STUDIES OF OPTICALLY INDUCED MAGNETIZATION DYNAMICS IN COLLOIDAL IRON OXIDE NANOCRYSTALS

A Dissertation

by

CHIH-HAO HSIA

Submitted to the Office of Graduate Studies of
Texas A&M University
in partial fulfillment of the requirements for the degree of

DOCTOR OF PHILOSOPHY

August 2010

Major Subject: Chemistry

STUDIES OF OPTICALLY INDUCED MAGNETIZATION DYNAMICS IN COLLOIDAL IRON OXIDE NANOCRYSTALS

A Dissertation

by

CHIH-HAO HSIA

Submitted to the Office of Graduate Studies of
Texas A&M University
in partial fulfillment of the requirements for the degree of

DOCTOR OF PHILOSOPHY

Approved by:

Chair of Committee,	Dong Hee Son
Committee Members,	Wayne Saslow
	Simon W. North
	Christian Hilty
Head of Department,	David H. Russell

August 2010

Major Subject: Chemistry

ABSTRACT

Studies of Optically Induced Magnetization Dynamics in Colloidal Iron Oxide Nanocrystals.

(August 2010)

Chih-Hao Hsia, B.S.; M.S., National Chiao Tung University, Taiwan

Chair of Advisory Committee: Dr. Dong Hee Son

Studying dynamics of magnetization relaxation in excited magnetic materials is important both for understanding the rates and pathways of magnetization relaxation and for the potential use in spin-based electronics and data storage devices in the future. Previous studies have demonstrated that the size of nanocrystals is an important factor for energy relaxation in quantum dots and metal nanoparticles. Since magnetization relaxation is one of energy relaxation pathways, the size of nanocrystals may be also an important factor for magnetization relaxation in nanoscale magnetic materials. The goal of this study is to have a better understanding of magnetization relaxation in nanoscale magnetic materials. In particular, we focused on the correlation between the nanocrystal size and the rates of spin-lattice relaxation (SLR), a magnetization relaxation pathway, in magnetic nanocrystals.

The size-dependent magnetization relaxation rate after optically induced demagnetization in colloidal Fe_3O_4 nanocrystals was measured by using time-resolved Faraday rotation (FR). Fe_3O_4 nanocrystals were chosen as the model system to study the

correlation between the size of nanocrystals and the rates of SLR due to the well-established synthetic procedure of making nanocrystals with various sizes and narrow size dispersion. Faster SLR rates were observed in smaller Fe_3O_4 nanocrystals. The results suggested the surface of nanocrystals have higher efficiency of SLR than the interior region by using a simple model to analyze the SLR rates of Fe_3O_4 nanocrystals with various sizes. Higher efficiency of SLR at the surface may be due to the stronger spin-orbit coupling at the surface relative to the interior region. In addition to magnetization dynamics studies, the effect of oxidation on static FR in iron oxide nanocrystals (between Fe_3O_4 and γ-Fe_2O_3) was studied. The results indicated FR signal is linearly correlated to the strength of optical transition between Fe^{2+} and Fe^{3+} in Fe_3O_4 for a given size of nanocrystals.

ACKNOWLEDGEMENTS

This dissertation would not be possible without the support of many people. First at all, I would like to thank my research advisor, Dr. Dong Hee Son, for his guidance and support over the last five years. He spent a tremendous amount of time guiding me. He provided me with an opportunity to do research from scratch. That great experience will become my unforgettable memory. Thanks also go to my committee members (past and present), Dr. North, Dr. Cremer, Dr. Saslow, Dr. Weimer and Dr. Hilty, for the help and advice they provided.

I would like to thank the members of the Son research group for their help, advice, and friendship. I would also like to individually thank Tai-Yen Chen, Stacey Wark, Hsiang-Yun Chen, and Dr. Shengguo Jia. Thanks also go to my friends and department staff for making my time at Texas A&M University a great experience.

I would also like to thank Dr. Hsin-Tien Chiu at National Chiao Tung University in Taiwan. He encouraged me to study in the U.S. and take the challenge. I also want to extend my gratitude to the Taiwan Merit Scholarship (TMS-094-1-A-021) for the four-year financial support. This extra financial support helped me to convince my wife to come to the U.S. with me.

Finally, I would like thank my family for their love, support, and encouragement throughout the years. In particular, I would like to thank my mother for raising me alone for more than twenty years. The love from my wife, Yi-Chieh Yeh, and my daughter, Emily Hsia, was very important support for me to during my Ph.D. study. Thank you!

TABLE OF CONTENTS

CHAPTER Page

LIST OF FIGURES

FIGURE Page

FIGURE Page

FIGURE Page

FIGURE Page

LIST OF TABLES

CHAPTER I

INTRODUCTION

Studying dynamics of spin relaxation in excited magnetic materials is important for understanding the rates and pathways of spin relaxation. An understanding of spin relaxation is essential for the potential use in spin-based electronics and data storage devices in the future.[1-5] The process of energy relaxation from spin to lattice degrees of freedom, i.e. spin-lattice relaxation, is one of the spin relaxation pathways.[6, 7] A better understanding of spin-lattice relaxation in magnetic nanocrystals is the goal of this study.

The energy relaxation in nanoscale materials is an important issue. The importance of energy relaxation in quantum dots and gold nanoparticles has been demonstrated in earlier studies.[8-11] For quantum dots, the dynamics of electrons and holes relaxation in excited semiconductor quantum dots are important for the potential use in light emitting diodes (LED) and solar cells.[10] A high yield quantum dot LED can be achieved by blocking non-radiactive relaxation pathways and only allowing energy relaxation in terms of light emission. On the other hand, light emitting pathways need to be eliminated to achieve more efficient solar energy conversion in solar cells. For gold nanoparticles, it is also important to understand the energy dissipation from electrons to lattice vibrations after photoexcitation.[11] The energy in lattice degrees of freedom can cause melting of gold nanocrystals because the melting point of gold in nanometer scale

---

This dissertation follows the style and format of the *Journal of the American Chemical Society*.

is much lower than in bulk.[12] The understanding of laser-induced photothermal melting mechanism will be helpful for photothermal reshaping of metal nanoparticles. It was reported that photothermal reshaping of gold nanoparticles has potential applications in optical recording data storage devices.[13] In contrast to the well-studied dynamics of energy relaxation in quantum dots and gold nanoparticles, studies of spin relaxation in magnetic nanocrystals are still rare.[14, 15] Studying the dynamics of spin relaxation in excited magnetic nanocrystals may lead to a better understanding of the correlation between the size of nanocrystals and the spin relaxation in nanoscale magnetic materials. This study may be important for making high-density spin-based electronics.

The size of nanocrystals is an important factor of energy relaxation in nanoscale materials. For example, the rates of electron relaxation via Auger processes in excited quantum dots are size-dependent.[9, 10, 16] Faster electron relaxation occurs in smaller quantum dots. The size of magnetic nanocrystals is also considered as an effective factor of spin relaxation because the rates of energy flow from lattice to spin degrees of freedom were affected by the thickness of Fe_3O_4 films after optical excitation.[17]

It was reported that the magnetic anisotropy constant (K_{aniso}) in partially oxidized Fe_3O_4 nanocrystals increased by decreasing the volume of nanocrystals.[18] Loosely speaking, the magnetic anisotropy constant (K_{aniso}) indicates the strength of the spin-orbit coupling and the spin-orbit coupling strength is a key factor determining the rate of spin-lattice relaxation. The rates of spin-lattice relaxation are roughly linear to the magnetic anisotropy constants (K_{aniso}) of ferromagnetic and ferrimagnetic thin films.[19] In Ref. 19, faster spin-lattice relaxation was observed in materials with higher magnetic

anisotropy constants (K_{aniso}). The results imply the rates of spin-lattice relaxation in magnetic nanocrystals may be influenced by the volume of nanocrystals because the spin-orbit coupling strength may be varied with nanocrystal size.

Fe_3O_4 nanocrystals were chosen as the model system to study the correlation between nanocrystal size and spin-lattice relaxation due to its well-established synthesis procedures.[18, 20-22] Fe_3O_4 nanocrystals with good size dispersion can be synthesized from 4 nm to larger than 100 nm in diameter.[23] It is essential to have nanocrystals with good size dispersion (dispersion < 10 %) for size dependent properties studies. Another advantage of choosing Fe_3O_4 nanocrystals is that many physical properties of Fe_3O_4 nanocrystals have been well-studied. Fe_3O_4 nanocrystals have been intensively studied because of their potential biomedical applications, such as drug delivery, contrast agent for magnetic resonance imaging (MRI) and heating mediator for cancer.[22]

Fe_3O_4 nanocrystals with diameter smaller than 30 nm have only a single magnetic domain but are superparamagnetic, showing no net magnetic moment without an external magnetic field. Magnetization direction in superparamagnetic nanocrystals randomly fluctuates because the thermal energy exceeds the magnetic anisotropy energy of the nanocrystal, shown in Figure 1.1.[24] The magnetic moment of a nanocrystal is the sum of the magnetic moments in the nanocrystal. The magnetic anisotropy energy provides an energy barrier that tends to fix magnetic moment direction of an individual nanocrystal. The height of energy barrier, magnetic anisotropy of nanocrystal, is linearly correlated to the volume of the nanocrystal according to the Stoner-Wohlfarth theory.[6] This superparamagnetic behavior results in well-suspended colloidal Fe_3O_4 nanocrystals.

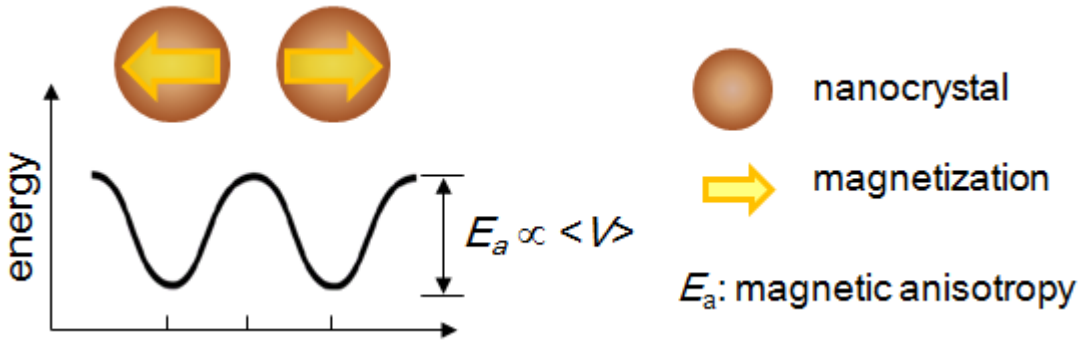

Figure 1.1. Magnetic anisotropy (E_a) is an energy barrier that tends to fix the magnetic moment direction of an individual nanocrystal. The height of energy barrier is linearly proportional to the volume of the nanocrystal ($\langle V \rangle$) according to the Stoner-Wohlfarth theory. When thermal energy exceeds the energy barrier, the magnetic moment direction of an individual nanocrystal is randomly flipped, resulting in superparamagnetic nanocrystals.

A suspension of Fe_3O_4 nanocrystals is useful for optical based measurements, such as absorption spectroscopy and Faraday rotation measurment.[25] For example, the surface of Fe_3O_4 is more readily oxidized into γ-Fe_2O_3 than the interior. The degree of oxidation in iron oxide nanocrsytsals can be easily determined by the absorption intensity in the near-infrared region, which is only due to intervalence charge transfer transition between Fe^{2+} and Fe^{3+} in Fe_3O_4.

The magnetic ordering in Fe_3O_4 nanocrystals is believed to be ferrimagnetic, like bulk Fe_3O_4. The magnetic moment of a nanocrystal is due to unpaired spin of electrons in Fe cations. In a free Fe^{3+} cation, the magnetic moment is due to 5 unpaired spins at 5 degenerate energy levels. In the Fe_3O_4 lattice, the energy levels split into two groups via ligand field splitting, due to the symmetry of the orbitals.[6] The ferromagnetic order is a result of the crystal structure, shown in Figure 1.2. The crystal structure of Fe_3O_4 is called spinel. The oxygen ions lie on a face-center cubic packed structure, and iron cations fill some of the tetrahedral and octahedral sites. In the formula of Fe_3O_4, one Fe sits on tetrahedral site (A site) and two Fe cations sit on octahedral sites (B site). The magnetic structure is composed of the two magnetic sublattices, A and B, separated by oxygen. The exchange interaction between two sublattices, mediated by oxygen anions, results in an antiparallel alignment of the magnetic moments of the A and B sublattices. The magnetic moments of the A and B sublattices are not equal and result in a net magnetic moment. The magnetic contributions from the two Fe^{3+} cations on different sublattice, A and B, cancel. Therefore, the net magnetic moment of Fe_3O_4 is due to the magnetic moment of Fe^{2+} on B sublattices.

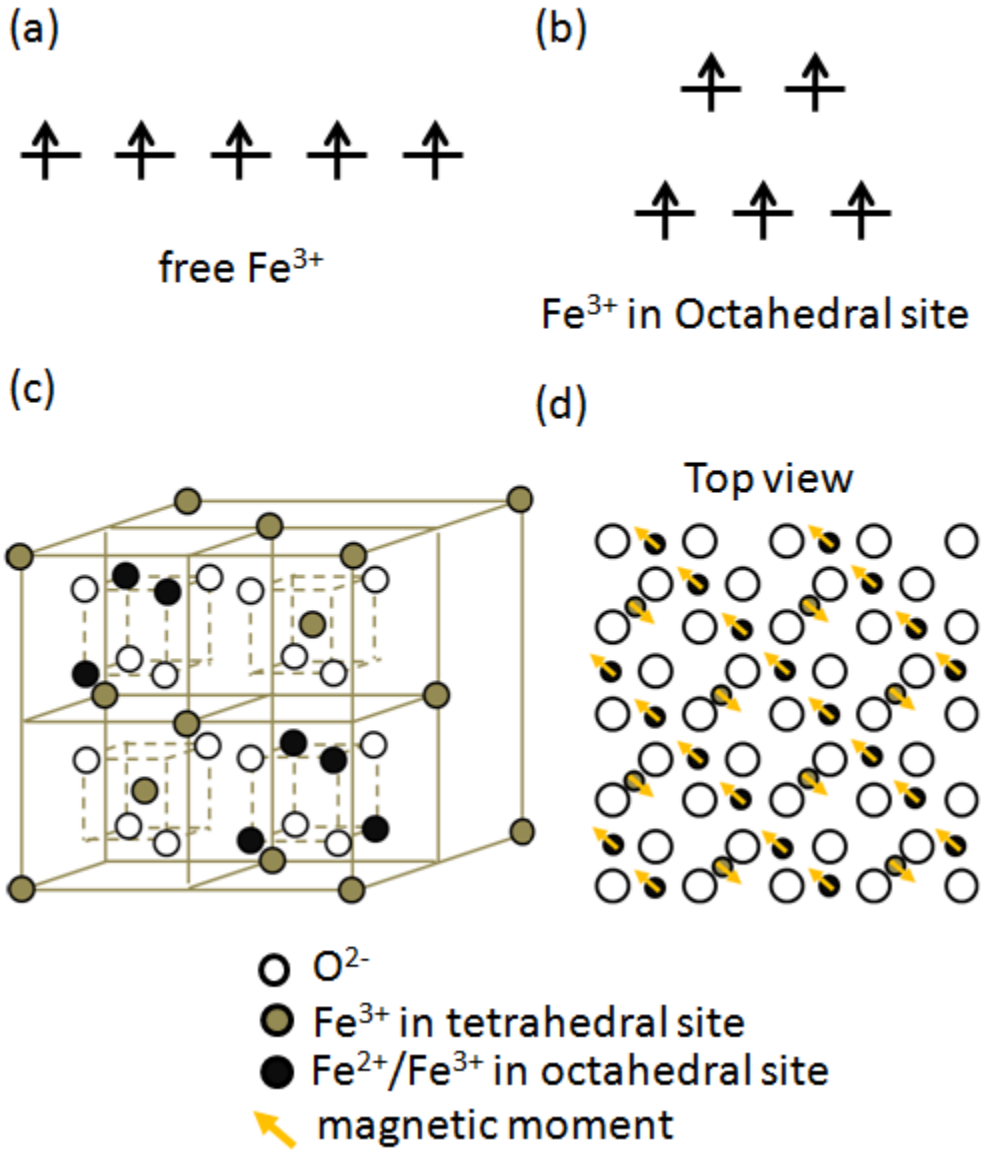

Figure 1.2. (a) The energy levels for unpaired electrons in free Fe^{3+} are degenerate. (b) The energy levels for unpaired electrons split when Fe^{3+} is in the Fe_3O_4 lattice. Fe^{3+} in octahedral site (B site) is shown as example. (c) Crystal structure of Fe_3O_4. (d) Top view of Fe_3O_4 crystal structure. The directions of magnetic moment of each Fe cations in Fe_3O_4 are shown as arrows.

The dynamics of magnetization relaxation after optical excitation in magnetic materials have been studied by time-resolved magneto-optic effects, such as Faraday rotation (FR) and magneto-optic Kerr effect (MOKE).[26-29] With the advancement of femtosecond laser techniques, one can selectively excite the electrons in the material and then monitor the energy relaxation in real time. A three heat reservoir model, namely electrons, spins, and lattice, was widely used to describe laser-induced demagnetization and the following magnetization relaxation in magnetic materials, shown in Figure 1.3.[29] The electrons absorb the photon energy, leading to a non-equilibrium temperature difference among three heat reservoirs. Energy flow from electrons to spins cause demagnetization, decrease of the magnitude of magnetic moments, with the time scales as fast as sub-picoseconds (ps). One explanation for the demagnetization is that the energy in the spin reservoir randomizes the direction of the spins, resulting in a decrease of magnetization. One pathway for spins to relax energy is spin-lattice relaxation, an energy flow from the spin to the lattice, and the time scales of the relaxation are in the order of 100 ps.

In this dissertation, time-resolved Faraday rotation measurements were performed in Fe_3O_4 nanocrystals with various sizes to understand the correlation between the nanocrystal size and the spin-lattice relaxation rate after optical excitation. The synthetic procedures to produce spherical Fe_3O_4 nanocrystals of different sizes will be discussed in Chapter II. Faraday rotation measures the rotation of linear polarization of light transmitted through magnetic materials. Due to the essentially optical nature of the technique, Faraday rotation signal can be contributed from the strength of optical

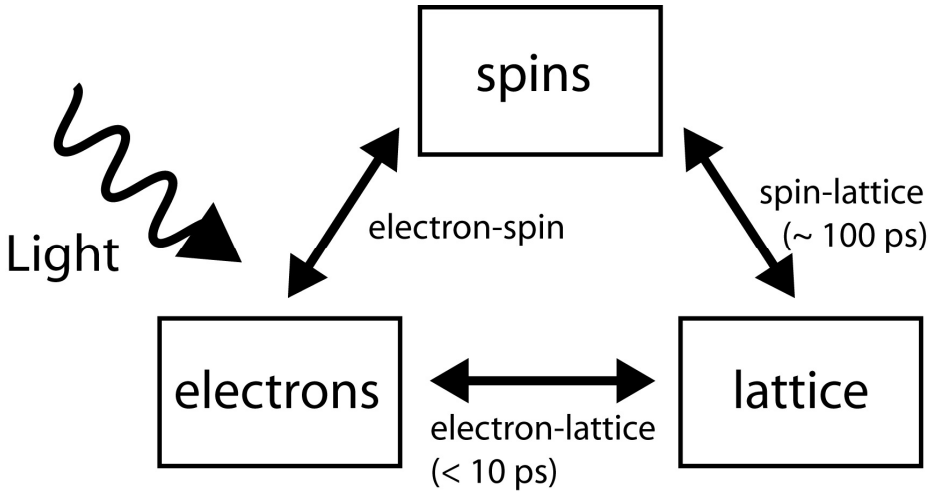

Figure 1.3. The three heat reservoir (electrons, spin, and lattice) model is used to explain the magnetization dynamics after optical excitation.

transition and the magnetization of material. Chapter III demonstrates that time-resolved Faraday rotation data reflects the change of magnetization as a function of time. The correlation between the size of nanocrystals and spin-lattice relaxation in photoexcited Fe_3O_4 nanocrystals will be discussed in Chapter IV. It was found that the rate of spin-lattice relaxation in smaller Fe_3O_4 nanocrystals is faster due to the higher efficiency of spin-lattice relaxation at the surface relative to the interior region. The higher efficiency of spin-lattice relaxation at the surface is due to the discontinuous lattice at the surface leading to a stronger spin-orbit interaction. The oxidation layer at the surface in oxidized Fe_3O_4 nanocrsytals is not a factor for spin-lattice relaxation, although different dynamics of magnetization relaxation in iron oxide nanocrystals with different degrees of oxidation were obtained. The effect of oxidation on the static Faraday rotation signal in iron oxide nanocrystals will be discussed in Chapter V. Finally, some concluding remarks and future directions for the dynamics of magnetization relaxation in magnetic nanomaterials will be discussed in Chapter VI.

CHAPTER II

SAMPLE PREPARATION AND CHARACTERIZATION

2.1 Introduction

Magnetite (Fe_3O_4) nanocrystals were chosen as the model system to study the correlation between the size of nanocrystals and the rate of magnetization relaxation due to their well-established synthetic procedures.[20, 21] In addition, many properties in Fe_3O_4 have been well-studied since Fe_3O_4 is one of the oldest magnetic materials. Thermal decomposition of iron precursor in high boiling point solvent with long hydrocarbon chained surfactants is a promising way to prepare Fe_3O_4 nanocrystals with ~ 10 % dispersion of the size. The diameter of monodisperse Fe_3O_4 nanocrystal can be prepared from 5 nm up to 100 nm by varying synthetic conditions.[23] The range of nanocrystal size for this study is from 5 to 15 nm in diameter. The synthetic process developed by Sun *et al*. was chosen because it is the most reproducible method to prepared Fe_3O_4 nanocrystals with the desired sizes.[20] Larger Fe_3O_4 nanocrystals with good size dispersion (~ 10%) can be prepared by using seeded growth method. In seeded growth, the same chemical reaction was repeated with previously prepared Fe_3O_4 nanocrystals as a seed. In addition, the size of nanocrystals in this method can be also controlled by reaction temperature, concentration, and surfactant to iron precursor ratio.[22] High reaction temperature, high concentration and lower surfactant to Fe ratio can lead to form larger Fe_3O_4 nanocrystals, but size dispersion would become worse.

The size of nanocrystals was suggested as a factor for magnetization relaxation based on size-dependent energy dissipation processes in semiconductor quantum dots in earlier studies. For example, exciton relaxation in CdSe nanocrystals after photoexcitation were size dependent.[8-10] In addition, it has been reported that the rates of energy flow from lattice to spin were influenced by the thickness of Fe_3O_4 films after optical excitation.[17] The studies of size-dependent energy relaxation provide the information for tuning the rates and pathways of energy relaxation in nanoscle materials by varying the size of nanocrystals.

The size range of our study was chosen from 5 nm to 15 nm because the static size-dependent magnetic properties are more prominent at this size range.[30] Some static magnetic properties (such as Curie temperature, saturated magnetization, and magnetic anisotropy energy) have been reported as size dependent properties.[24, 30, 31] Most of the size dependent magnetic properties in ferromagnetic and ferromagnetic materials is due to the total amount of magnetic moments, which is correlated to the volume of nanocrystals. Curie temperature is the temperature that spontaneous magnetic materials start losing their magnetic ordering. The magnetic ordering in spontaneous magnetic materials is due to the exchange interaction between magnetic moments. The total exchange interaction energy is linearly correlated to the total amount of magnetic moments. The size-dependent magnetic anisotropy is linearly correlated to the volume of magnetic nanocrystals, which was discussed in Chapter I. The size-dependent saturation magnetization can be explained by a core/shell model. The first model suggested the magnetic moments at the surface of the magnetic nanocrystals are more disorder than the

magnetic moments in the interior. The decrease of magnitude of saturation magnetization is due to smaller contribution from the surface layers of the nanocrystals. The study of size dependent magnetization dynamics in photoexcited Fe_3O_4 nanocrystals will be discussed in Chapter IV in detail.

Nanocrystals have high surface-to-volume ratio and the surface of Fe_3O_4 is more readily oxidized. Thus, the effect of oxidation should be also considered in the study. The partially oxidized Fe_3O_4 nanocrystals can be treated as Fe_3O_4/γ-Fe_2O_3 core/shell nanostructures, which may also affect magnetization relaxation. Before studying the magnetization dynamics, the effect of oxidation on static Faraday rotation in iron oxide nanocrystals (between Fe_3O_4 and γ-Fe_2O_3) should be studied first. The effect of oxidation on the signal of magneto-optic Kerr effect (MOKE) in Fe_3O_4 films was observed, but the effect is not quantitatively understood because it is difficult to obtain the exact degree of oxidation in bulk.[32] However, the degree of oxidation in iron oxide nanocrystals can be easily achieved by using UV-Vis-NIR spectroscopy.[25] The effect of oxidation on static Faraday rotation will be discussed in detail in Chapter V, and the preliminary result of magnetization dynamics in partially oxidized Fe_3O_4 nancorystals will also be discussed in Chapter V. To have a better understanding of the effect of oxidation on static Faraday rotation in magnetic nanocrystals, Co nanocrystals were prepared. Co nanocrsytals are metal magnetic materials, and the oxidation layer (CoO) is an antiferromagnetic material, which does not contribute to the magnetization of nanocrystals. The synthetic procedure of Co nanocrystals will be discussed in this chapter.

Nanocrystals have versatile structural parameters, such as size, sharp, core/shell nanostructure …etc. The structural parameters play important roles on exciton relaxation in quantum dots. For example, Auger relaxation, one of the exciton relaxation processes, in excited quantum dots can be suppressed by coating certain semiconductor shells. Cobalt substituted ferrite ($Co_xFe_{3-x}O_4$) nanocrystals was prepared to study the correlation between cobalt content and the rates of spin-lattice relaxation. Cobalt substituted ferrite ($Co_xFe_{3-x}O_4$) nanocrystals was chosen because the cobalt content in ferrites can increase the magnetocrystalline anisotropy constant (K_{mca}) of the material. The magnetocrystal anisotropy is associated with the strength of spin-orbit coupling, and spin-orbit coupling is one key parameter to determine the rates of spin-lattice relaxation. Therefore, cobalt content is suggested as a factor for varying the rates of spin-lattice relaxation. The preliminary result of dynamics of magnetization relaxation in cobalt substituted ferrite ($Co_xFe_{3-x}O_4$) nanocrystals will also be discussed in Chapter IV. The synthetic procedure of making $Co_xFe_{3-x}O_4$ nanocrystals is very similar to the synthetic procedure of making Fe_3O_4 nanocrystals. The cobalt content (x) in the nanocrystals is controlled by the initial molar ratio between Co and Fe precursors, and the details will be discussed in this chapter.

2.2 Synthetic details

Figure 2.1 shows the reaction schemes of making magnetic nanocrytals, such as Fe_3O_4, $Co_xFe_{3-x}O_4$, Co nanocrystals. In addition, the phase conversion reactions between Fe_3O_4 and γ-Fe_2O_3 were also included.

2.2.1 *Chemicals*

The following chemicals were purchased from Aldrich and used without further purification. Iron (III) acetylacetonate ($Fe(acac)_3$, 97%), cobalt (II) acetylacetonate ($Co(acac)_2$, 97%), oleic acid (technical grade, 90% and 99%), oleylamine (technical grade, 70%), 1,2-dodecanediol (90%), phenyl ether (99%), benzyl ether (99%), 1-octadecene (ODE, technical grade, 90%), 1,2-dichlorobenzene (99%), tetradecane (99%). The following chemicals were purchased from Strem and used without further purification. Cobalt carbonyl ($Co_2(CO)_8$, stabilized in 1-5 % of hexane) and trioctylphosphine oxide (TOPO, 99%).

2.2.2 *One pot synthesis of 5nm Fe_3O_4 nanocrystals*

5 nm of spherical Fe_3O_4 nanocrystals were synthesized following the previously reported procedure.[20] 2 mmol of iron(actylacetonate)$_3$ ($Fe(acac)_3$, 97%) was placed in a 100 ml 3-neck round flask with the mixture of 10 mmol of 1,2-dodecanediol (90%), 6 mmol of oleic acid (technical grade, 90%) and 6 mmol oleylamine (technical grade, 70%) in 20 ml of phenyl ether (99%). The experiment setup of the synthesis was shown in Figure 2.2. A magnetic stirring bar was placed in the flask, and the mixture was under

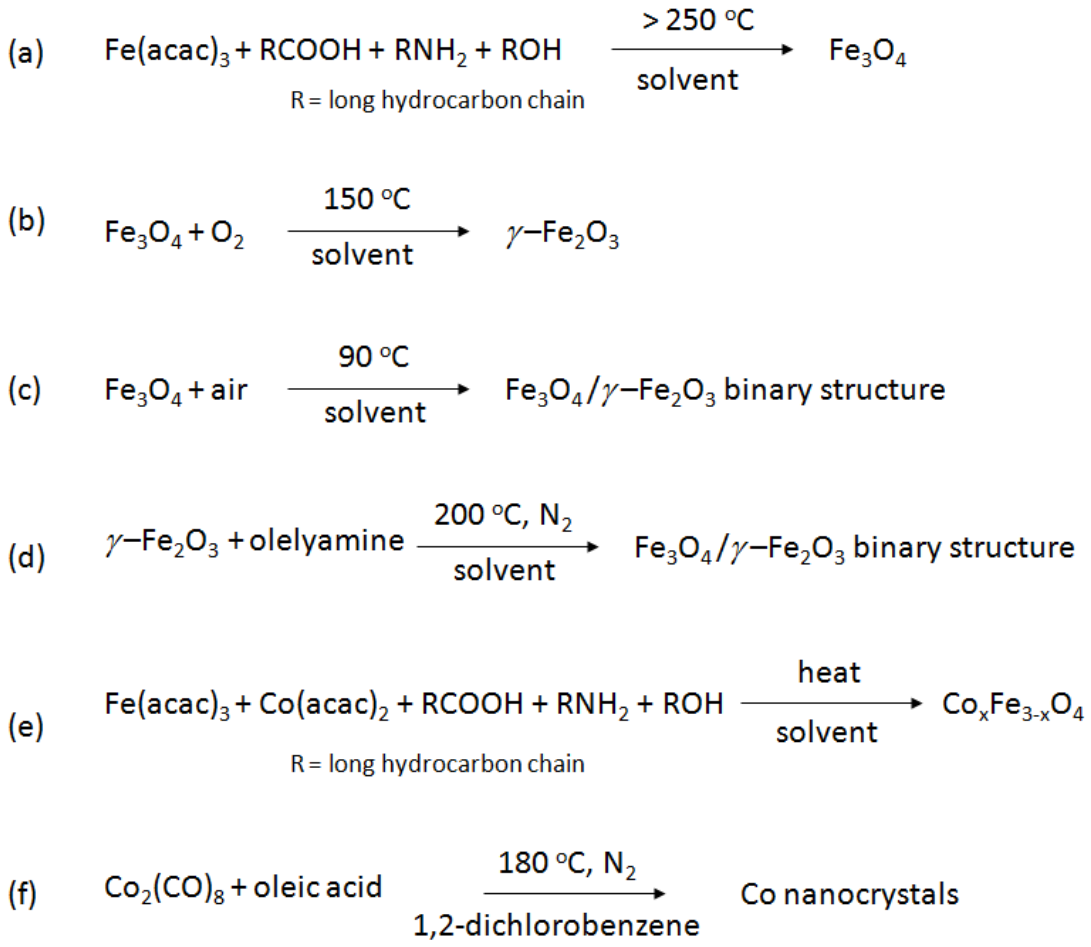

Figure 2.1 Reaction schemes of making magnetic nanocrystals. (a) Fe_3O_4 nanocrystals, (b) γ-Fe_2O_3 nanocrystals, (c) Fe_3O_4-γ-Fe_2O_3 binary nanostructure from oxidation reaction, (d) Fe_3O_4-γ-Fe_2O_3 binary nanostructure from reduction reaction, (e) $Co_xFe_{3-x}O_4$ nanocrystals, (f) Co nanocrystals.

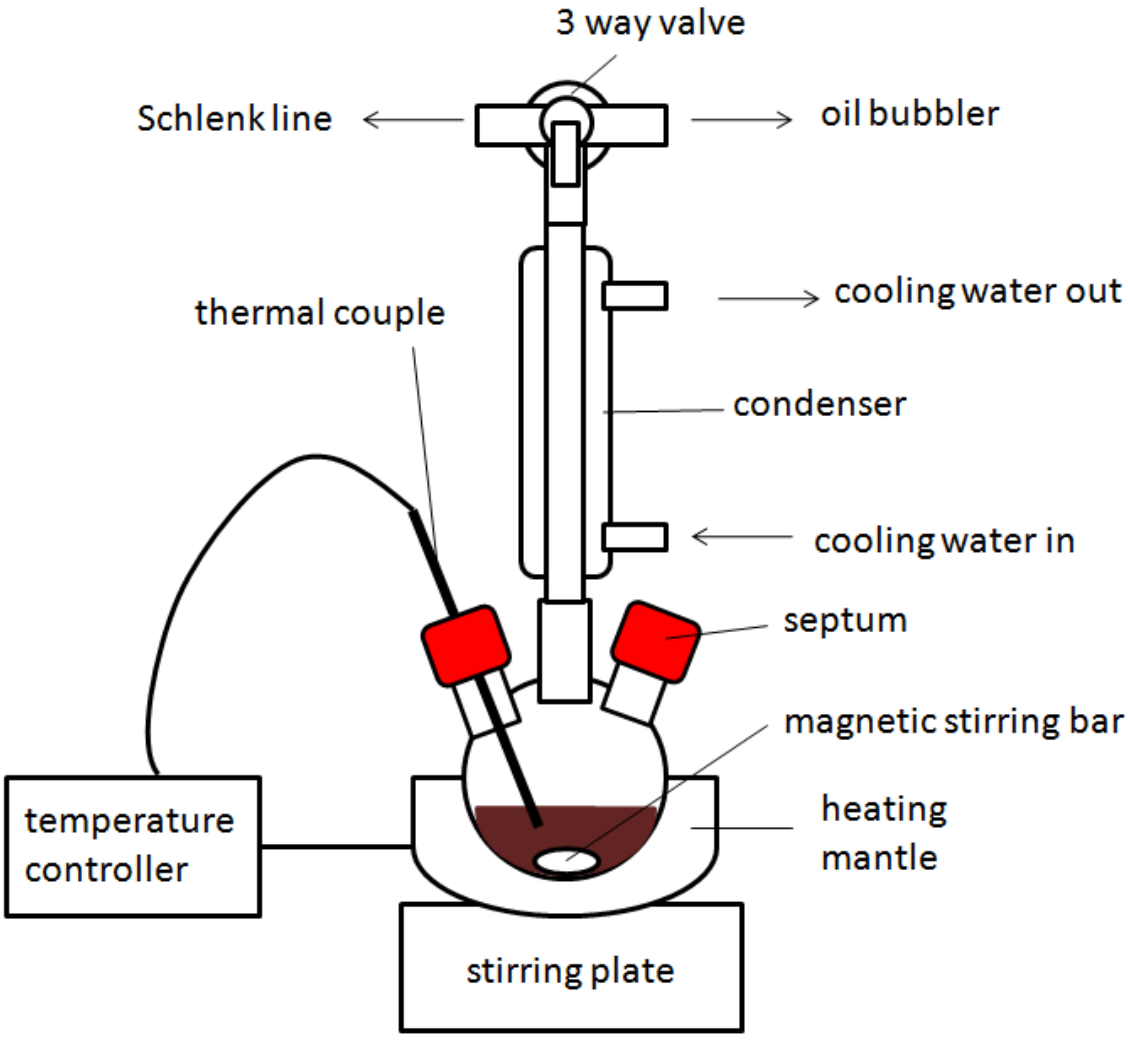

Figure 2.2 Experimental setup for synthesis of Fe_3O_4 nanocrystals.

stiring during whole reaction period. A Liebig condenser was set at the middle neck of the flask and two side necks were capped with septa. A heating mantle was place under the flask. The reaction flask was connected to a Schlenk line system (vacuum/gas manifold). The reaction was performed under nitrogen (N_2) environment. The N_2 filled environment was achieved by evacuating and refilling N_2 back to the environment for three times. The reaction temperature was controlled by a temperature controller associated with a thermocouple and a heating mantle. The mixture was first heated to 200 ^oC, and the temperature was held at 200 ^oC for 1 hr. The color of mixture was turned from red to black, implying $Fe(acac)_3$ was decomposed and the monomer for Fe_3O_4 nanocrystals was formed. 5 nm Fe_3O_4 nanocrystals was made after increasing the temperature to 250 ^oC and holding at this temperature for 30 min. 7 nm of Fe_3O_4 nanocrystals were prepared by the same procedure described above at 290 ^oC for 1 hr in benzyl ether, instead of phenyl ether. After cooled to room temperature, the result product was treated with ethanol under air, and product was precipitated from the solution. The product nanocrystals were cleaned by the repeated precipitation with ethanol and resuspension in hexane. Because the cleaning was performed under the ambient condition, the surface of Fe_3O_4 nanocrystals was slightly oxidized and turned into γ-Fe_2O_3.

2.2.3 *Seeded growth synthesis of Fe_3O_4 nanocrystals*

Fe_3O_4 nanocrystals with the sizes larger than 7 nm were prepared by the seeded growth method. In this method, the smaller nanocrystals were used as the seed under the

similar reaction condition described above. After cooled to room temperature, the result product was treated with ethanol under air, and product was precipitated from the solution. The product nanocrystals were cleaned by the repeated precipitation with ethanol and resuspension in hexane. Because the cleaning was performed under the ambient condition, the surface of Fe_3O_4 nanocrystals was slightly oxidized and turned into γ-Fe_2O_3, resulting in the reduction of the charge-transfer absorption intensity in near IR region. In addition to seeded growth, larger nanocrystals can also be prepared by increasing the reaction temperature.

2.2.4 *Reduction of oxidized Fe_3O_4 nanocrystals*

The partially oxidized Fe_3O_4 nanocrystals could be reduced back to 'pure' Fe_3O_4 phase by heating the nanocrystals in 1-octadecene under N_2 atmosphere at the reaction temperature higher than 200 ^oC in the presence of small amount of oleylamine (5% v/v). Even γ-Fe_2O_3 nanocrystals can be reduced back to 'pure' Fe_3O_4 phase. The reaction kinetics was monitored by UV-Vis spectroscopy, which will be discussed in sample characterization part. The reduction reaction can also occur under oxygen-free environment without adding extra oleylamine at the temperature higher than 210 ^oC. In addition, the reduction reaction can even occur under the ambient condition with excess amount of oleylamine because oleyalmine is a reducing agent for γ-Fe_2O_3.

2.2.5 *Synthesis of γ-Fe_3O_4 nanocrystals*

Spherical colloidal γ-Fe_2O_3 nanocrystals were prepared by oxidizing Fe_3O_4 nanocrystals under oxygen (O_2) at 150 ^oC for >1 hr. For instance, 5 nm of Fe_3O_4 nanocrystals in hexane were added into benzyl ether (~ 20 ml) with small amount of oleic acid (~ 1 ml) to prevent aggregation of nanocrytals. The mixture was heated at 90 ^oC under air for 30 min to remove hexane and then heated to 150 ^oC under O_2 until the oxidation is completed. The completion of oxidation was ascertained by checking the disappearance of the intervalence charge-transfer (IVCT) absorption in the near-IR region. The absorption in the near-IR region is only contributed from the IVCT transition between Fe^{2+} and Fe^{3+} in Fe_3O_4.

2.2.6 *Synthesis of iron oxide nanocrystals with different degrees of oxidation*

Iron oxide nanocrystals with a varying degree of oxidation between Fe_3O_4 and γ-Fe_2O_3 were prepared in two different ways: (i) oxidation of Fe_3O_4 and (ii) reduction of γ-Fe_2O_3 nanocrystals. The oxidation of Fe_3O_4 nanocrystals was performed in tetradecane by heating the sample solution at 90 ^oC in the open air with the presence of a small amount of oleic acid to keep the nanocrystals from precipitation. The reduction of γ-Fe_2O_3 nanocrystals was performed in the mixture of 1-octadecene and oleylamine (20:1 volume ratio) under N_2 atmosphere at >200 ^oC. The degree of oxidation was varied simply by changing the reaction time. The partially oxidized Fe_3O_4 and partially reduced γ-Fe_2O_3 nanocrystals were kept under N_2 atmosphere at -15 ^oC to prevent additional oxidation of the sample before the measurements are made. The degree of oxidation in

iron oxide nanocrystals was determined from the intensity of the charge-transfer absorption in near-IR region, which decreases linearly with the degree of oxidation from Fe_3O_4 to γ-Fe_2O_3 phase.

2.2.7 *Synthesis of $Co_xFe_{3-x}O_4$ nanocrystals*

Spherical $Co_xFe_{3-x}O_4$ nanocrystals passivated with oleic acid with varying cobalt content (x) in the range of $0 < x < 0.9$ were synthesized by following the previously reported procedure.[21] For instance, 7 nm $Co_xFe_{3-x}O_4$ nanocrystals were synthesized by thermally decomposing iron acetylacetonate ($Fe(acac)_3$) and cobalt acetylacetonate ($Co(acac)_2$) with a mixture of oleic acid, oleylamine and 1,2-dodecanediol at 290 ºC in benzyl ether. Tuning of cobalt content was achieved by varying the molar ratio of $Fe(acac)_3$ and $Co(acac)_2$. After cooled to room temperature, the result product was treated with ethanol under air, and product was precipitated from the solution. The product nanocrystals were cleaned by the repeated precipitation with ethanol and resuspension in hexane.

2.2.8 *Synthesis of Co nanocrystals*

Spherical Co nanocrystals passivated with oleic acid were synthesized by following the previously reported procedure. For instance, 8 nm Co nanocrystals were synthesized by thermally decomposing cobalt carbonyl ($Co_2(CO)_8$) with a mixture of oleic acid (99%) at 180 ºC in 1,2-dichlorobenzene. Tuning of the size of nanocrystals was achieved by varying the molar ratio of $Co_2(CO)_8$ and oleic acid. To present

oxidation, the sealed flask was transferred into nitrogen filled glovebox after cooled down to room temperature. The product nanocrystals were precipitated by adding methanol. The supernatant solution was discarded and the Co nanocrystals were re-suspended in nonpolar solvent, such as hexane, cyclohexane, and toluene.

2.2.9 *Sample preparation for characterization*

Iron oxide nanocrystals were suspended in non-polar solvent (such as hexane, toluene, and cyclohexane) for UV-Vis-NIR absorption measurement. The size and crystal structure of the nanocrystals were examined by transmission electron microscopy (TEM) and X-ray diffraction (XRD). The TEM sample was prepared by adding a drop of dilute iron oxide nanocrystals solution on carbon film coated copper grid. For XRD measurements, the predicated samples were used. The surfactants capped on nanocrystals were studied by Fourier transform infrared (FT-IR) spectroscopy. The concentration of colloidal iron oxide and cobalt substituted ferrite nanocrystals were calculated from total metal ion concentration measured from elemental analysis employing induced coupled plasma-atomic emission spectroscopy (ICP-AES) and the size of the particle measured from TEM images. The samples for ICP-AES measurement were prepared by digesting the dried nanocrystal samples in 1 ml of aqueous HCl (12 M) solution and diluting it to several ppm level with aqueous HNO_3 (1M) solution.

In addition, static mass magnetization and blocking temperature measurement of $Co_xFe_{3-x}O_4$ nanocrystals were performed. The static mass magnetization of $Co_xFe_{3-x}O_4$ nanocrystal samples was measured by using a superconducting quantum interference

device (SQUID) magnetometer (MPMS-XL, Quantum Design). Saturation magnetization of $Co_xFe_{3-x}O_4$ nanocrystal samples was obtained from the field-dependent magnetization measurement at the temperature of 5K. Similar to the results from previous study, the saturation magnetization exhibited only a very weak dependence on cobalt content (< 4%).[33] In order to estimate the magnetic anisotropy constant (K_{aniso}) of the nanocrystals, blocking temperature (T_B) was also obtained from the zero-field-cooled (ZFC) magnetization measurement within the temperature range of 10-300 K. In the ZFC curve, the temperature at which the magnetization reaches the maximum value was taken as T_B. The magnetic anisotropy constant (K_{aniso}), partially reflecting the strength of spin-orbit coupling was obtained from $K_{aniso} = 25k_BT_B/V$, where k_B is Boltzmann constant and V is the volume of the nanocrystal.[34] For all the SQUID measurements, the nanocrystal samples were dispersed in liquid eicosane to avoid the aggregation and subsequently solidified to prevent the agitation of the nanocrystals in the matrix during the measurements.

2.3 Characterization of iron oxide nanocrystals

2.3.1 *Size of nanocrystals*

Figure 2.3 shows the TEM images of Fe_3O_4 nanocrystals in different sizes (diameter of nanocrystals: 5, 7, 10, and 15 nm) by one pot synthesis and seeded growth. From the TEM images, all of the nanocrystals have nearly spherical shape, and the particle size dispersion is less than 10 % in diameter. The result indicates the size of nanocrystals can be controlled by seeded growth. In addition to seeded growth, larger nanocrystals can be prepared by increasing the reaction temperature. A plot of result particle size versus reaction temperature was shown in Figure 2.4. Larger nanocrystals can also be prepared by decreasing the solvent amount, namely increase the concentration. The reduction of solvent leads to the saturation of nuclei at early stage, and more reactant can contribute to the growth of nanocrystals, giving larger particles. A plot of result particle versus solvent amount was shown in Figure 2.5. Reducing the surfactant to Fe ratio is another approach to synthesize larger Fe_3O_4 nanocrystals. The reduction of surfactants leads the particles with less surfactant coverage, and the growth of particle can continue on the uncovered area, giving larger particles. A plot of result particle versus surfactant to iron ratio was shown in Figure 2.6. The later approaches were not chosen for this study, because the dispersion of particle size became much worse than original procedure.

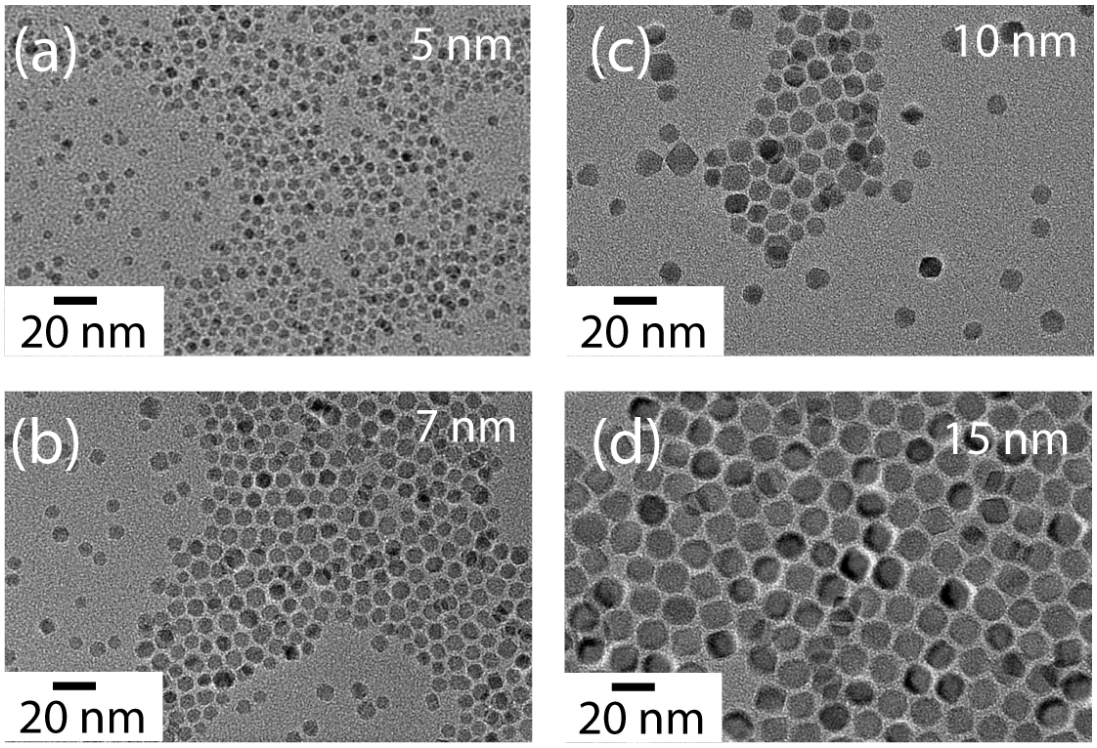

Figure 2.3 TEM images of Fe_3O_4 nanocrystals with different sizes (a-d).

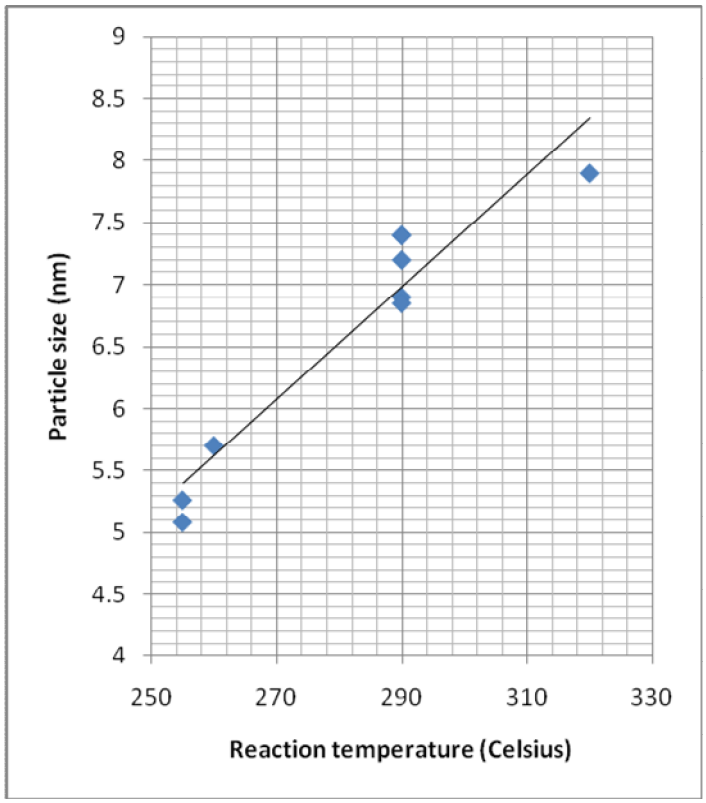

Figure 2.4 This plot illustrates that larger nanocrystals can be prepared by increasing the reaction temperature. For 320 ^{o}C reaction, the solvent is 1-octadecene. The black straight line is guide of eye.

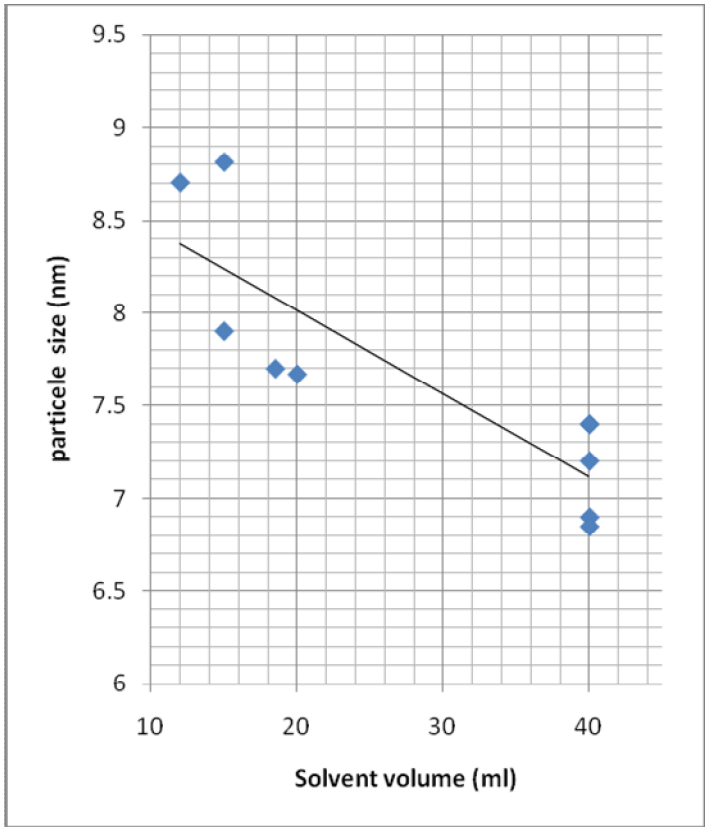

Figure 2.5 This plot illustrates that larger nanocrystals can be prepared by reducing the amount of solvent in the reaction. The reaction conditions were modified from 7 nm Fe_3O_4 synthesis, and all quantities were doubled. The reaction temperatures were set at 290 ^{o}C. The black straight line is guide of eye.

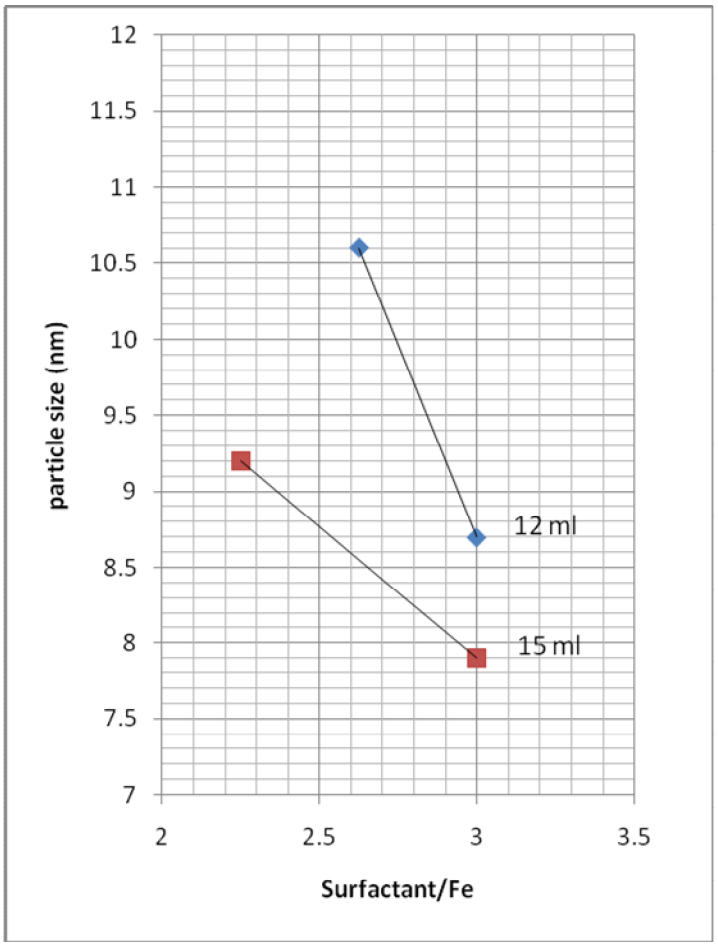

Figure 2.6 This plot illustrates that larger nanocrystals can be prepared by reducing the surfactant to iron ratio. The reaction conditions were modified from the synthesis with reduction of solvent amount, and the solvent amount were 12 and 15 ml in double scale synthesis. The reaction temperatures were set at 290 ^{o}C. The black straight line is guide of eye.

2.3.2 *Crystal structure of nanocrystals*

The crystal structure of Fe_3O_4 nanocrystals was confirmed by XRD patterns, shown in Figure 2.7. All the major peaks in XRD patterns of all the nanocrystals fit the XRD pattern of Fe_3O_4 database. The peaks at 2θ of 35.5, 43.2, 53.6, 56.9, and 62.6 degree were assigned as the X-ray diffraction from (311), (400), (422), (511), and (440) planes, respectively. The crystal structure of Fe_3O_4 is spinel, and general composition of spinel is AB_2O_4. A represents cations occupied in tetrahedral site and B represents cations occupied in octahedral sites of O^{2-} ion face center cubic (fcc) lattice. In typical spinel structure (Fe_3O_4), 1/8 of tetrahedral sites are occupied and 1/2 octahedral sites are occupied. As mentioned before, nanocrystals are easily oxidized due to their high surface-to-volume ratio. Thus, the surface of Fe_3O_4 nanocrystals can be oxidized into γ-Fe_2O_3 during the cleaning processes in the ambient condition. It is difficult to distinguish Fe_3O_4 and γ-Fe_2O_3 by using XRD because the crystal structures of Fe_3O_4 and γ-Fe_2O_3 are very similar. The only difference between Fe_3O_4 and γ-Fe_2O_3 in crystal structure is the number of vacancy sites, so the lattice parameters of Fe_3O_4 (0.8396 nm) and γ-Fe_2O_3 (0.8346 nm) are closed, based on JCPDS files 19-629 and 39-1346. This is supported by comparison of XRD patterns of Fe_3O_4 and γ-Fe_2O_3 nanocrystals, shown in Figure 2.8.

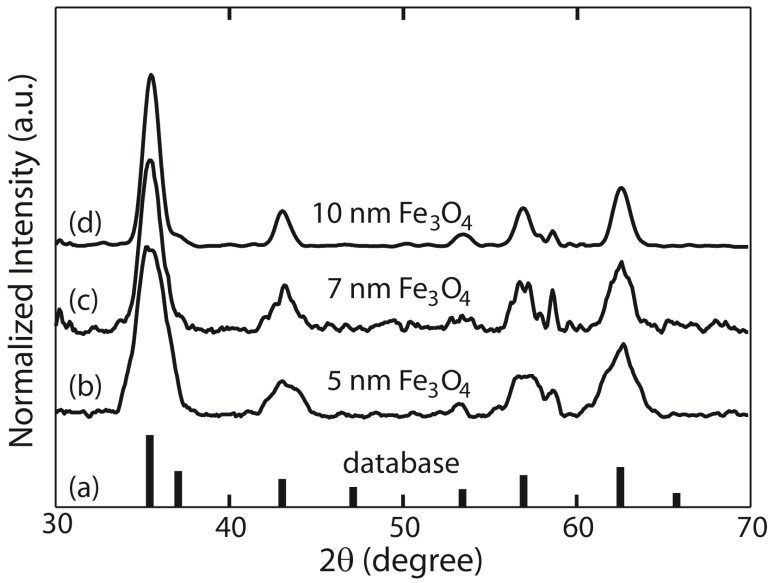

Figure 2.7 XRD patterns of Fe_3O_4 nanocrystals with different sizes. X-ray source: Cu.

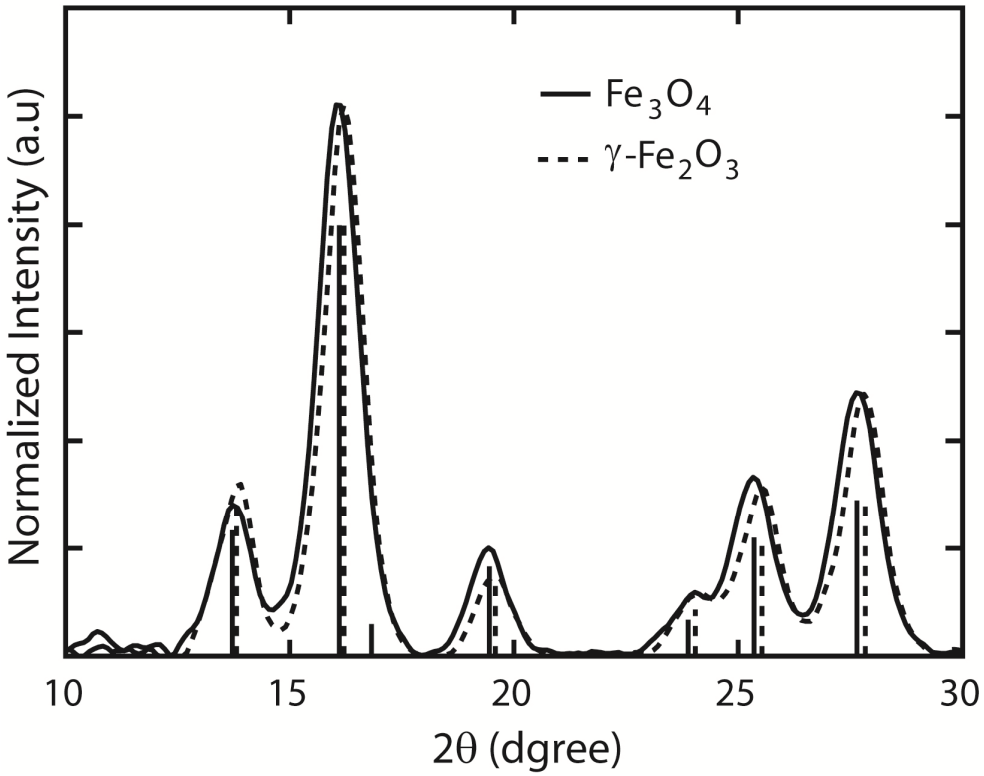

Figure 2.8 XRD patterns of Fe_3O_4 and γ-Fe_2O_3 nanocrystals. X-ray source: Mo.

2.3.3 *Absorption spectra of iron oxide nanocrystals.*

UV-Vis spectroscopy is an easy method to distinguish Fe_3O_4 and γ-Fe_2O_3 nanocrystals by comparing the absorption intensity in the near-infrared region, which is assigned to the inter-valence charge transfer (IVCT) transition between Fe^{2+} and Fe^{3+} in Fe_3O_4. The IVCT absorption in Fe_3O_4 phase disappears as the oxidation converts Fe^{2+} into Fe^{3+}, shown in Figure 2.9. The spectra were normalized at 385 nm, which is an isobestic point between Fe_3O_4 and γ-Fe_2O_3. The isobestic point was found based on results of UV-Vis-NIR spectra and ICP-OES. Absorption of γ-Fe_2O_3 in the near-infrared region is absent because the electronic transitions between Fe^{3+} cations are forbidden transitions. The IVCT absorption was considered to be a good linear measure of the oxidation in γ-Fe_2O_3-Fe_3O_4 binary system and has been previously utilized to monitor the oxidation kinetics of Fe_3O_4 nanocrystals.[22] The absorption spectra of oxidized Fe_3O_4 nanocrsystals was well represented as the linear combination of the spectra of γ-Fe_2O_3 and Fe_3O_4 nanocrystals. (See Figure 2.9c and 2.9d) A common linear scale of IVCT absorption intensity was used to determine the degree of oxidation for iron oxide for a given particle size. Zero intensity of IVCT absorption was taken to represent 100% γ-Fe_2O_3 phase. To obtain the reference absorption spectrum of 'pure' Fe_3O_4 phase, the spectrum was obtained under oxygen-free atmosphere using the reduced Fe_3O_4 nanocrystals dispersed in N_2-bubbled solvent to avoid oxidation. The reduction kinetics was monitored by UV-Vis spectroscopy, shown in Figure 2.10. The absorption intensity at 635 nm was used to indicate the degree of oxidation, because the major contribution

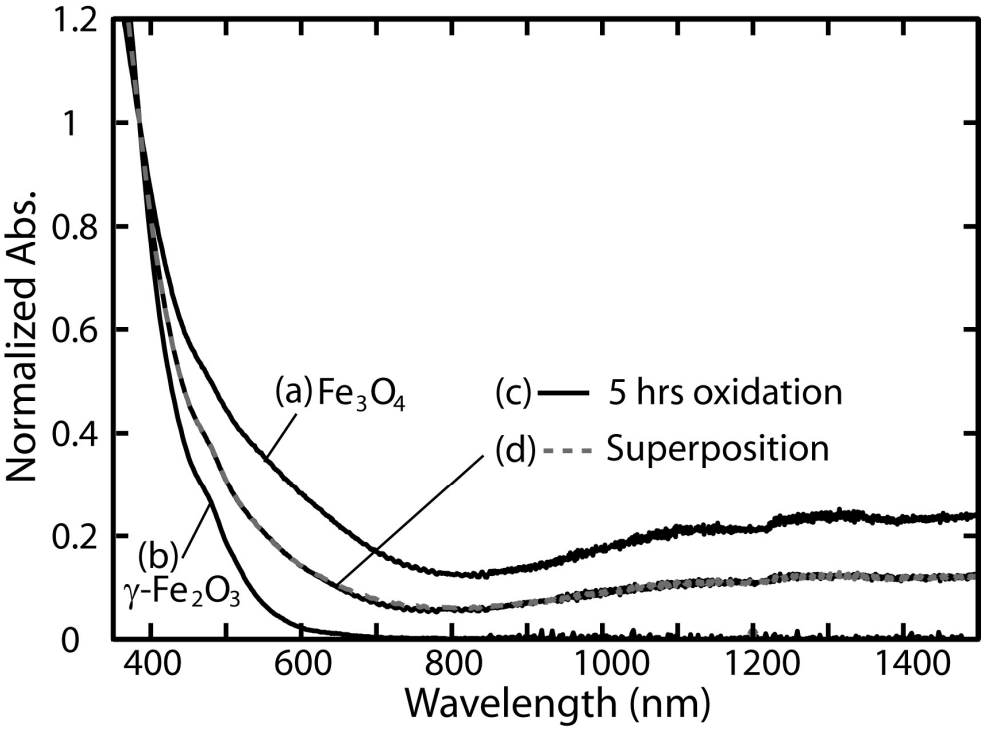

Figure 2.9 UV-Vis-NIR spectra of 7 nm iron oxide nanocrystals with different degree of oxidation. (a) Fe_3O_4, (b) γ-Fe_2O_3, (c) oxidized Fe_3O_4 90 ^oC for 5hrs, (d) superposition of Fe_3O_4 and γ-Fe_2O_3 with corresponding degree of oxidation with (c).

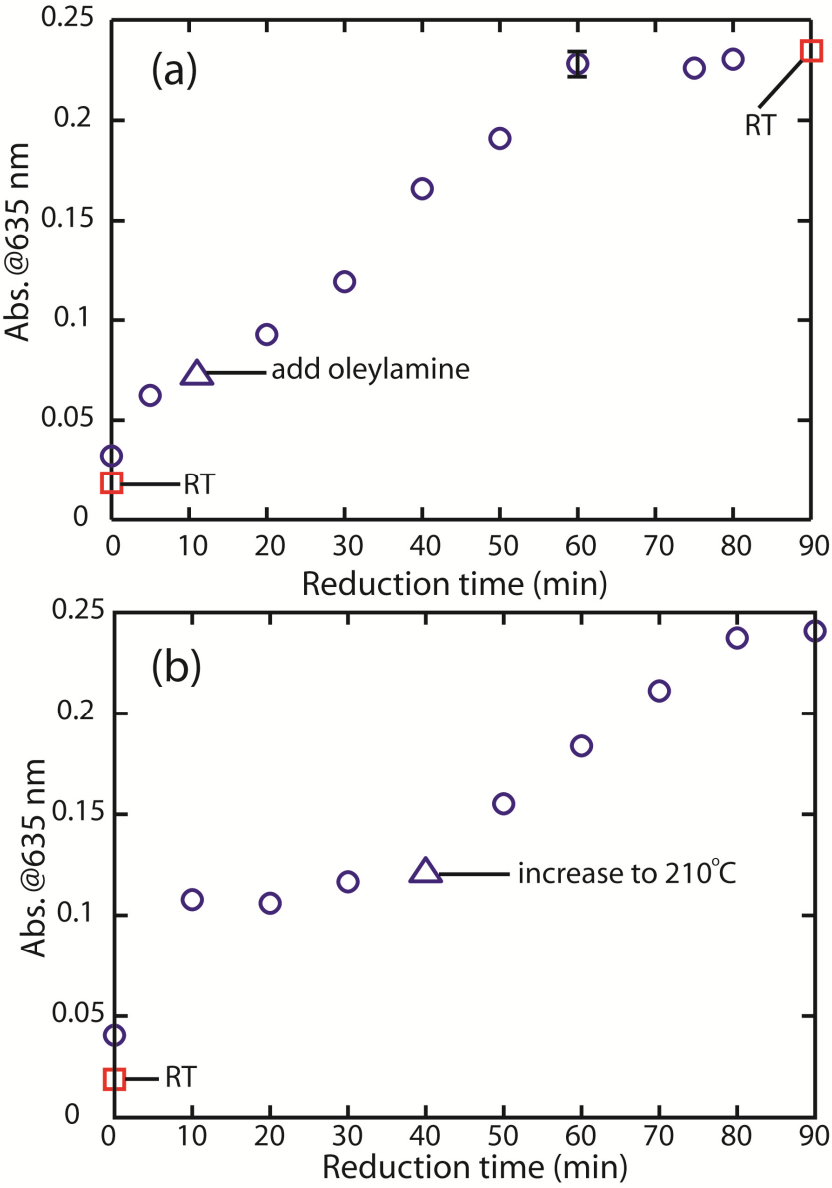

Figure 2.10 Reduction kinetics of 5 nm iron oxide nanocrystals was represented by absorption intensities at 635 nm as a function of time. (a) extra olelyamine was added in the reaction (b) no extra oleylamina was added in the reaction. The start of reduction reaction was set the time while temperature reach 200 ^{o}C.

of the absorption at 635 nm in Fe_3O_4 nanocrystals is from the IVCT transition between Fe^{2+} and Fe^{3+}, shown in Figure 2.9. Figure 2.10a shows the reduction kinetics with adding extra olelyamine, and Figure 2.10b shows the reduction kinetic without adding extra olelyamine in the reaction. The results indicate oleylamine help the reduction of γ-Fe_2O_3, because the reduction reaction seems to be stopped after 10 min in the reaction without adding extra olelyamine. In addition, the reaction temperature is another important factor for reduction of γ-Fe_2O_3, because the reduction reaction restarted while increasing the temperature to 210 ^oC. γ-Fe_2O_3 nanocrystals can be reduced by olelayamine even in the ambient condition. (data is not shown) The results suggests oleylamine is a reducing agent for γ-Fe_2O_3 nanocrystals. Therefore, olelyamine, reaction temperature, and reducing atmosphere are all important factors for the reduction of γ-Fe_2O_3. Among these factors, the reaction temperature is essential because no reduction reaction was observed at the reaction temperature lower than 200 ^oC.

Figure 2.11a shows the oxidation kinetics of Fe_3O_4 nanocrystals in non-polar solvent. Oxidation of Fe_3O_4 nanocrystals was studied in water, and our oxidation kinetics data is consistent with theirs. The oxidation of Fe_3O_4 has been well-studied in films, and the mechanism of oxidation was suggested as diffusion of Fe^{2+} from interior to surface. Our data can fit this diffusion model, Sidhu model, shown in Figure 2.11. The Sidhu diffusion is written as follows:

$$\frac{M_t}{M_\infty} = 6\pi^{-1/2}\left(\frac{Dt}{a^2}\right)^{1/2} - 3\frac{Dt}{a^2}$$

where M_t is the amount of Fe^{2+} that has diffused out after time t and M_∞ is the total

amount Fe^{2+}. D is diffusion coefficient and a is the radius of spherical nanocrystal. Dividing each side by t, we get

$$\frac{M_t}{M_\infty}\times\frac{1}{t}=6\pi^{-1/2}\left(\frac{D}{a^2}\right)^{1/2}\times\frac{1}{t^{1/2}}-3\frac{D}{a^2}$$

Therefore, a straight line should be obtained when we plot $(M_t/M_\infty)/t$ versus $1/t^{1/2}$. Figure 2.11b shows a straight plot and the data fit Sidhu's model very well. The result indicates the oxidation mechanism is outward diffusion of Fe^{2+}. So, partial oxidized Fe_3O_4 should have a Fe_3O_4/γ-Fe_2O_3 core/shell nanoctructure, and there is no sharp interface between two species.

For Fe_3O_4 nanocrystals of different sizes, the reference absorption spectra of 'pure' Fe_3O_4 phase normalized to the total Fe ion concentration in the sample solution was very similar with only a small variation of the IVCT absorption intensity as shown in Figure 2.12. Slightly weaker IVCT absorption in smaller nanocrystals may arise from a number of sources. The discontinuity at the surface, which reduces the number of Fe^{2+}-Fe^{3+} pairs that gives rise to the IVCT absorption, may contribute to the weak size-dependent IVCT absorption intensity. The presence of carboxylate group of oleic acid binding the surface may also prefer Fe^{3+} over Fe^{2+} also reducing the IVCT absorption intensity.

UV-Vis-NIR spectra of Fe_3O_4 nanocrystals can be easily measured because the nanocrystals can suspend in non-polar solvents and the Fe concentration can be obtained. Superparamagnetic nanocrystals cannot attract each other throught magnetic dipole moments. While bulk Fe_3O_4 is ferrimagnetic, nanocrystals in these size ranges are

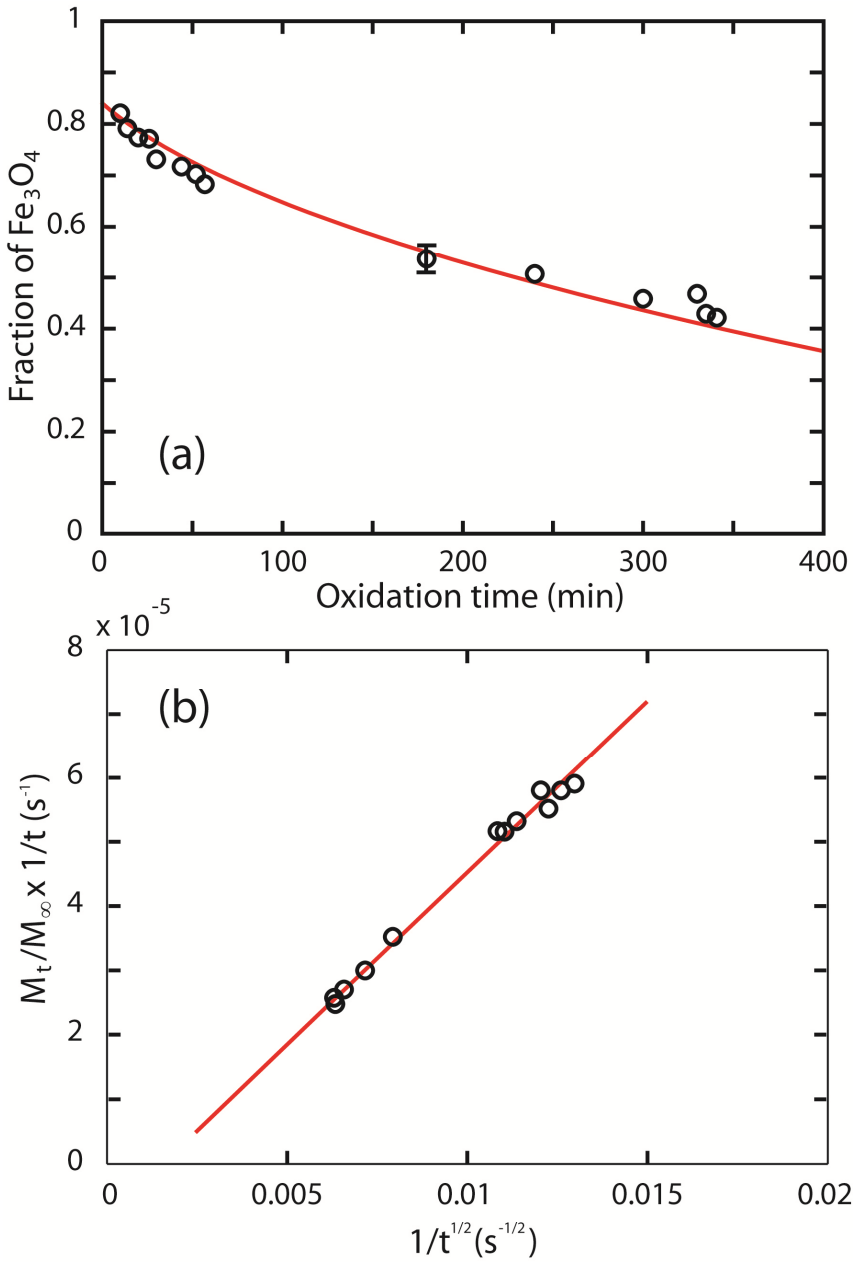

Figure 2.11 (a) Degree of oxidation as a function of time. Reaction temperature is 90 ^{o}C. Open circus represents real data, and red curve is fitting curve from Sidhu's diffusion model. (b) a plot $(M_t/M_\infty)/t$ versus $1/t^{1/2}$ based on Sidhu's diffusion model. Open circus represents real data, and red straight line is fitting data from Sidhu's diffusion model.

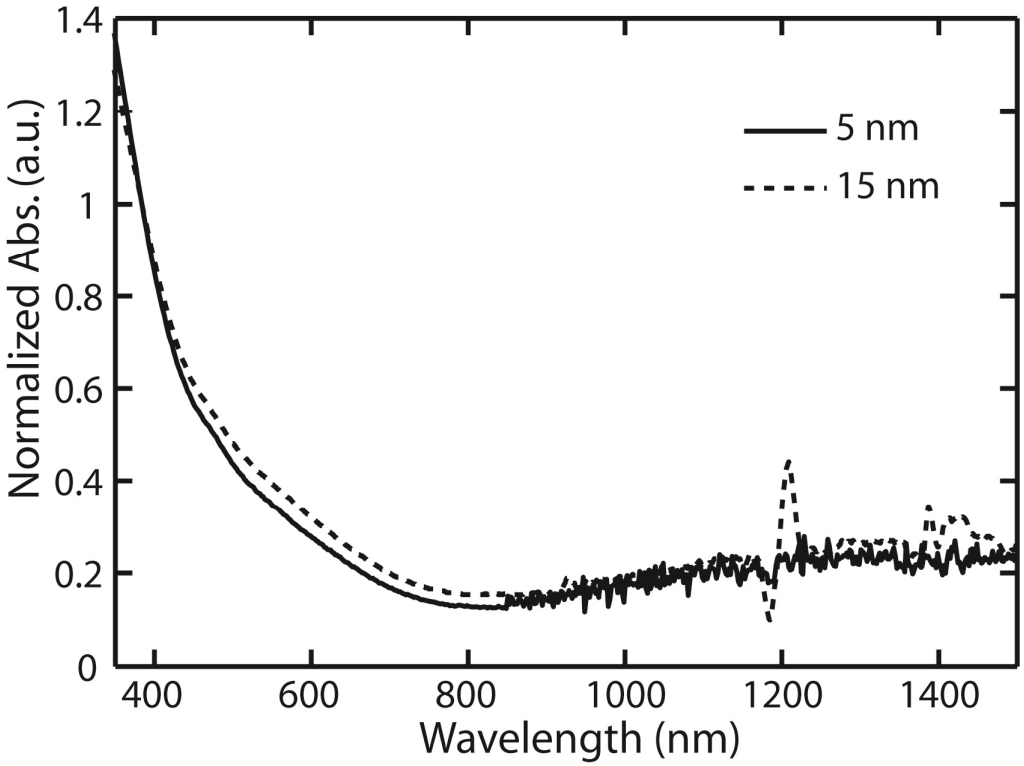

Figure 2.12 UV-Vis-NIR spectra of 5 nm and 15 nm 'pure' Fe_3O_4 nancorystals.

superparamagnetic at room temperature, meaning thermal energy overcomes the energy barrier of magnetic anisotropy of nanocrystals and flips the magnetization in the nanocrystals.

2.3.4 *FT-IR spectra of iron oxide nanocrystals.*

The surface of Fe_3O_4 nanocrystals was considered passivated with oleic acid. Figure 2.13a shows the FT-IR spectrum of Fe_3O_4 nanocrystals. The absorption in the range of 2850 to 3000 cm^{-1}, assigned as C-H stretching, indicates nanocrystals coated with long hydrocarbon chain surfactants. The disappearance of absorption around 1700 cm^{-1}, associated with vibration of COOH group, indicates no free oleic acid around nanocrystals. The absorption peaks appearing around 1500 cm^{-1} are associated with vibration of COO^- in Figure 2.13a and 2.13b. The results suggest the surface was coated with oleic acid. However, the absorption of function group of oleylamine ($-NH_2$), around 1600 cm^{-1}, is much weaker than COO^- group, so the existence of oleylamine cannot be ruled out by using FT-IR spectroscopy, shown in Figure 2.13c. The assignment of FT-IR peaks is summarized in Table 2.1.

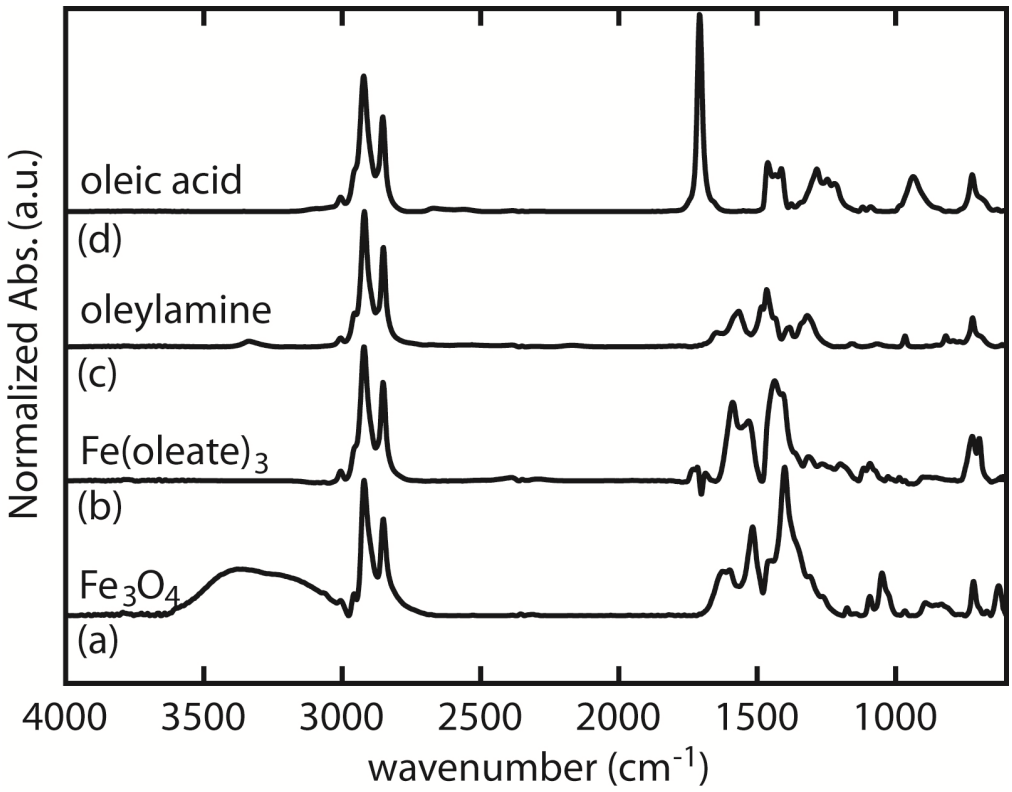

Figure 2.13 FTIR spectra of 5 nm Fe_3O_4 nancorystals (a), $Fe(oleate)_3$ (b), free olelyamine (c), and free oleic acid (d).

Table 2.1 Assignment of FT-IR peaks in Figure 2.13.

wavenumber (cm^{-1})	*Assignment*
2956	$-CH_3$ (asymmetric)
2923	$-CH_2-$ (asymmetric)
2853	$-CH_2-$ (symmetric)
1707	–COOH
1590	$-COO^-$ (asymmetric)
1527	$-COO^-$ (asymmetric)
1430	$-COO^-$ (symmetric)

The FT-IR assignment is consistent with the assignment in the reference.[35]

2.4 Characterization of $Co_xFe_{3-x}O_4$ nanocrystals

Figure 2.14 shows the TEM images of $Co_xFe_{3-x}O_4$ nanocrystals (x = 0.09 - 0.9). The size of nanoparticles is 7 nm, and the size dispersion is less than 10 %. The results indicate the same size of $Co_xFe_{3-x}O_4$ nanocrystals can be prepared by using similar reaction conditions. Figure 2.15 shows the XRD patterns of $Co_xFe_{3-x}O_4$ nanocrystals (x = 0.09 - 0.9). The XRD patterns of all the samples are very similar, indicating $Co_xFe_{3-x}O_4$ nanocrystals have the same crystal structures. Figure 2.16 shows the blocking temperature (T_B) of $Co_xFe_{3-x}O_4$ nanocrystals (x = 0.09 - 0.9). The results indicates the magnetic anisotropy energy, $E_a = 25K_BT_B$, increases with increasing the cobalt content in the nanocrystals.

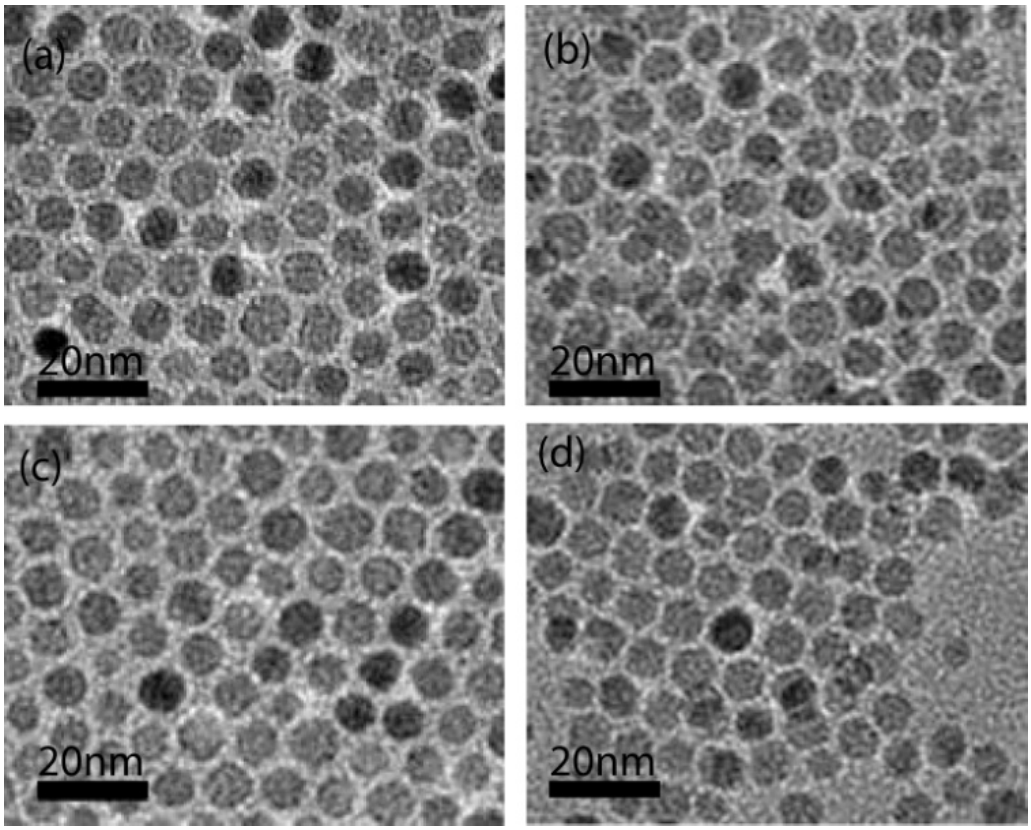

Figure 2.14 TEM images of $Co_xFe_{3-x}O_4$ nanocrystals. (a) x= 0.09, (b) x=0.18, (c) x= 0.3, (d) x=0.9.

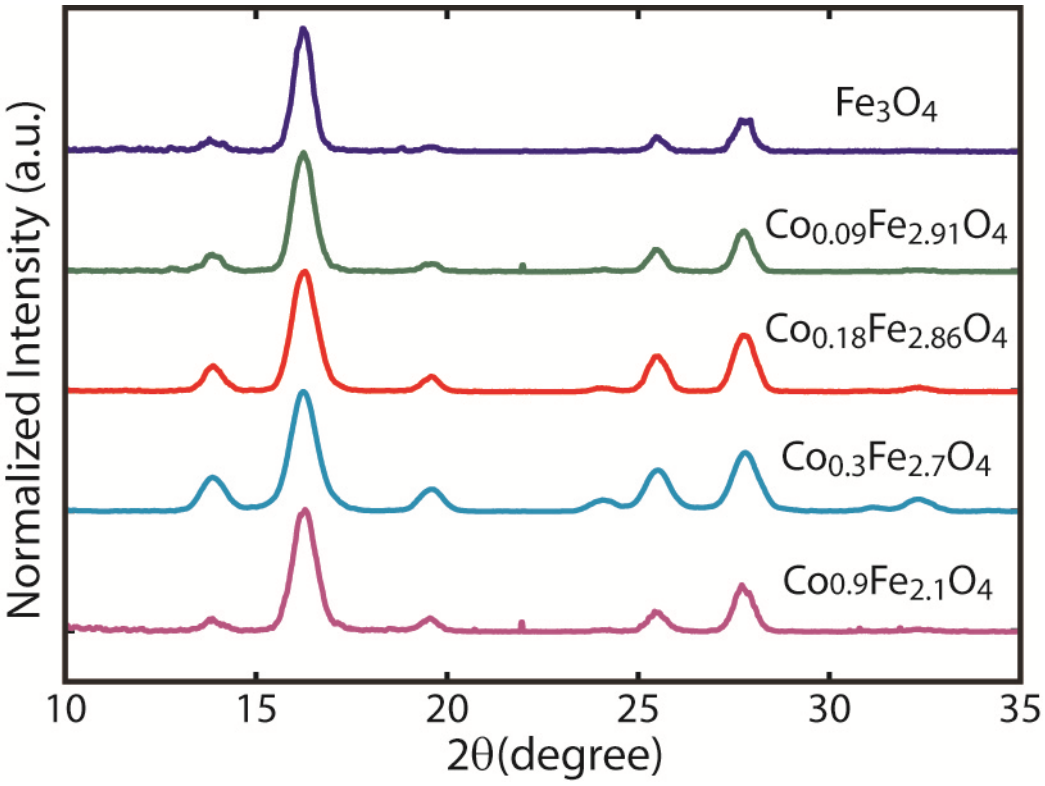

Figure 2.15 XRD patterns of $Co_xFe_{3-x}O_4$ nanocrystals. (a) x= 0.09, (b) x=0.18, (c) x= 0.3, (d) x=0.9.

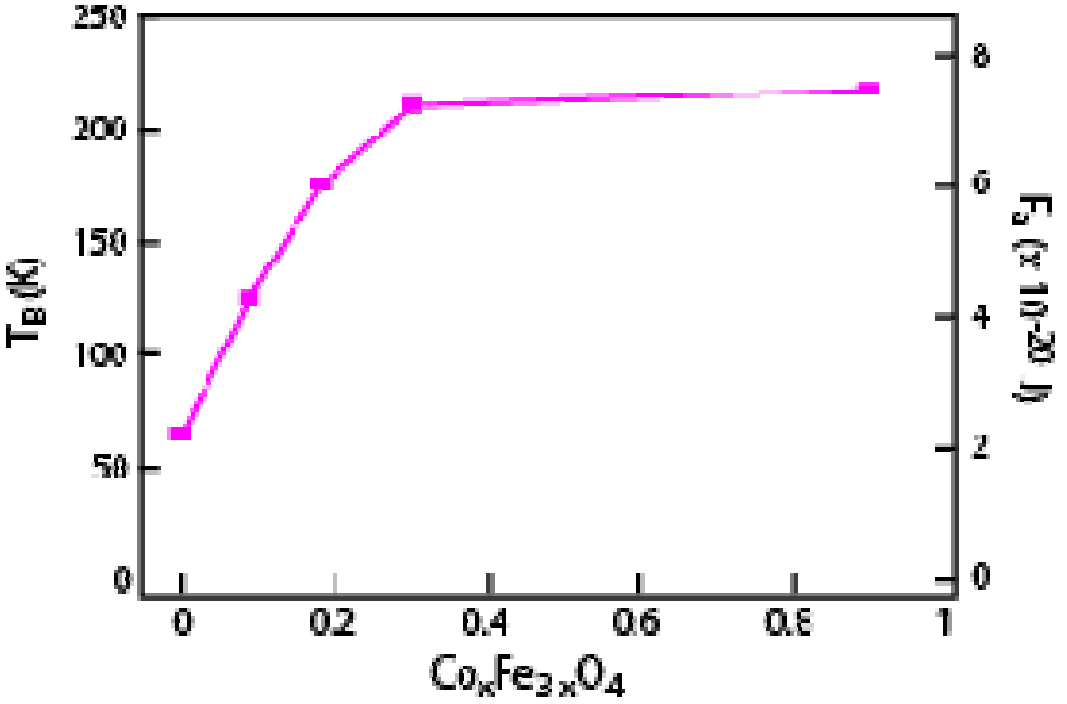

Figure 2.16 Blocking temperatures of $Co_xFe_{3-x}O_4$ nanocrystals (x = 0.09 - 0.9).

CHAPTER III

EXPERIMENTAL METHOD: TIME-RESOLVED FARADAY ROTATION*

3.1 Introduction

Time-resolved Faraday rotation is a useful tool to monitor ultrafast dynamics of magnetism in magnetic materials taking the merits of optical nature of this technique.[15, 36, 37] Faraday rotation measures the rotation of linear polarization of light transmitted through the magnetic materials, and whose magnitude is proportional to the magnetization for a given material. Due to the essentially optical nature of technique, the magnetization information is indirectly obtained from the optical response. Beside the magnetization of materials, Faraday rotation is also affected by the strength of optical transition since it is originated from the splitting of energy levels caused by magnetic field, so-called Zeeman effect. For example, the static Faraday rotation signal in iron oxide nanocrystals is linearly correlated with the strength of optical transition between Fe^{2+} and Fe^{3+} caions. (see Chapter V) In this chapter, I demonstrated that time-resolved Faraday rotation is a useful tool to measure the ultrafast dynamics of the magnetization in photoexcited Fe_3O_4 nanocrsytals, and the signal from time-resolved Faraday roation of this measurement reflects the change of magnetization.

---

* Reprinted in part with permission from *Nano Lett., 8* Hsia, C.-H.; Chen, T.-Y.; Son, D. H.; "Size-dependent Ultrafast Magnetization Dynamic in Iron Oxide Nanocrystals," 571, Copyright 2008 by the American Chemical Society.

Ultrafast dynamics of the magnetization in magnetic materials attracted a great deal of attention in recent years.[4, 38] In particular, modification of the magnetization on sub-picosecond (ps) time scales using femtosecond optical pulses in ferro- and antiferro-magnetic materials has been the subject of heated debates and active investigations.[26, 39-43] Because the ultrashort optical excitation could manipulate the magnetization on the time scales much faster than the typical spin-lattice relaxation time (>100 ps), a significant effort has been made to understand the microscopic mechanism. During the past decade, various mechanisms including both thermal and non-thermal pathways were proposed to explain the optically induced ultrafast demagnetization, magnetization, and spin switching.[28, 44, 45] From a practical point of view, the ability to control the ultrafast magnetization is very important in applications such as spintronics and magnetic data storage devices.[2, 3] Due to the continuing demand for higher-speed and larger-capacity devices, ultrafast magnetization dynamics in nanometer scale magnetic structures also gained much attention.[46] Earlier efforts to investigate the ultrafast dynamics of the magnetization in magnetic nanostructures mainly focused on thin film structures with one-dimensional spatial confinement or mesoscopic structures. On the other hand, magnetic structures with three-dimensional spatial confinement received much less attention,[37, 47] while the finite-size effect in nanometer length scale could be more systematically investigated. In this respect, colloidal magnetic nanocrystals are very useful for investigating the ultrafast dynamics of the magnetization in three-dimensionally confined magnetic structures. The merits of colloidal nanocrystals in the study of finite-size effect on various ultrafast dynamic processes were previously well

demonstrated in semiconductors nanocrystals,[48, 49] where the methods of size and shape control are highly developed. In this chapter, we report the femtosecond time-resolved studies on the optically induced ultrafast magnetization dynamics in size-controlled superparamagnetic Fe_3O_4 nanocrystals as a model system for the three-dimensionally confined magnetic nanostructures. Linearly polarized femtosecond optical pulses at 780 nm excited the weak absorption originating from the inter-valence charge transfer (IVCT) transition between Fe^{3+} and Fe^{2+} ions. The excitation resulted in an instantaneous decrease of Faraday rotation, indicating ultrafast photoinduced demagnetization. The Faraday rotation recovered on multiple time scales ranging from a few to hundreds of picoseconds. Here, we investigated how the dynamics of the ultrafast demagnetization and its recovery are affected by the density of the optical excitation and the size of the nanocrystals.

3.2 Experimental method

3.2.1 *Static Faraday rotation*

Faraday rotation (FR) is the change in polarization angle of the linearly polarized light passing through the magnetic materials and essentially reflects the magnetic circular birefringence of the materials.[50] For a given magnetic material, the magnitude of FR reflects the magnitude of magnetization. Faraday rotation is proportional to $\vec{M}(t)\cdot\vec{k}$, where $\vec{M}(t)$ and $\vec{k}$ are the magnetization vector of the nanocrystal and wavevector of the probe light, respectively.[51] In order to have maximum Faraday rotation signal the magnetization vector of the nanocrystal and wavevector should be parallel or anti-

parallel. The external field parallel to wavevector can be created by a pair of permanent magnets, shown in Figure 3.1. The magnetic field line is a straight line in the middle area between two magnets, but the region having straight magnetic field line is very small. Incorrect measurement could be done if the sample position is slight off from the center point. In order to overcome this situation, two iron plates were placed on two ends of magnets, shown in Figure 3.2. It is very clear that the introduction of iron plates on two ends of magnets will create more straight magnetic lines between two magnets. However, when magnets were place in this geometry, they would repel each other. In order to fix the position of magnets, a magnet holder was designed, shown in Figure 3.3. The magnets were placed into the holder and they were forced to close to each other by turning screw bolts. There were brass plates placed between crew bolts and magnets to protect the potential damage caused by the screw bolts. There were two small holes on both size of magnet holder, and the position of holes for probing light was set in the middle of two magnets. Sample cuvette was place in the middle of two iron plates. The material of the holder is aluminum, so the magnetic field lines would not influenced by the holder.

The experimental set up for the measurement of Faraday rotation of colloidal solution of nanocrystals is shown in Figure 3.4. The linearly polarized *cw* laser beam from a diode laser passing through a linear polarizer, whose axis is set at 45° with respect to the vertical direction, was used to measure FR. A Wollaston prism was placed before the detector to split the beam into two orthogonal polarization components with

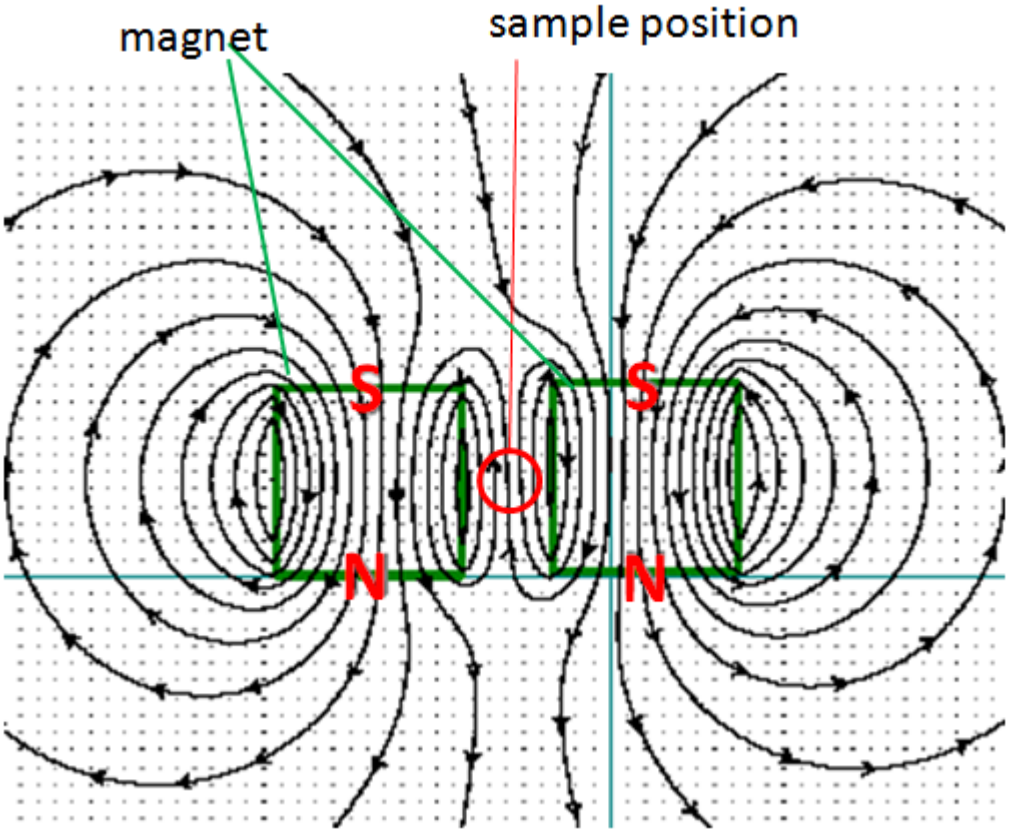

Figure 3.1 Simulation result of magnetic field lines created by two permanent magnets by freeware Vizmag. The green squares represent magnets. The magnetic field lines in the middle of two magnets are straight lines.

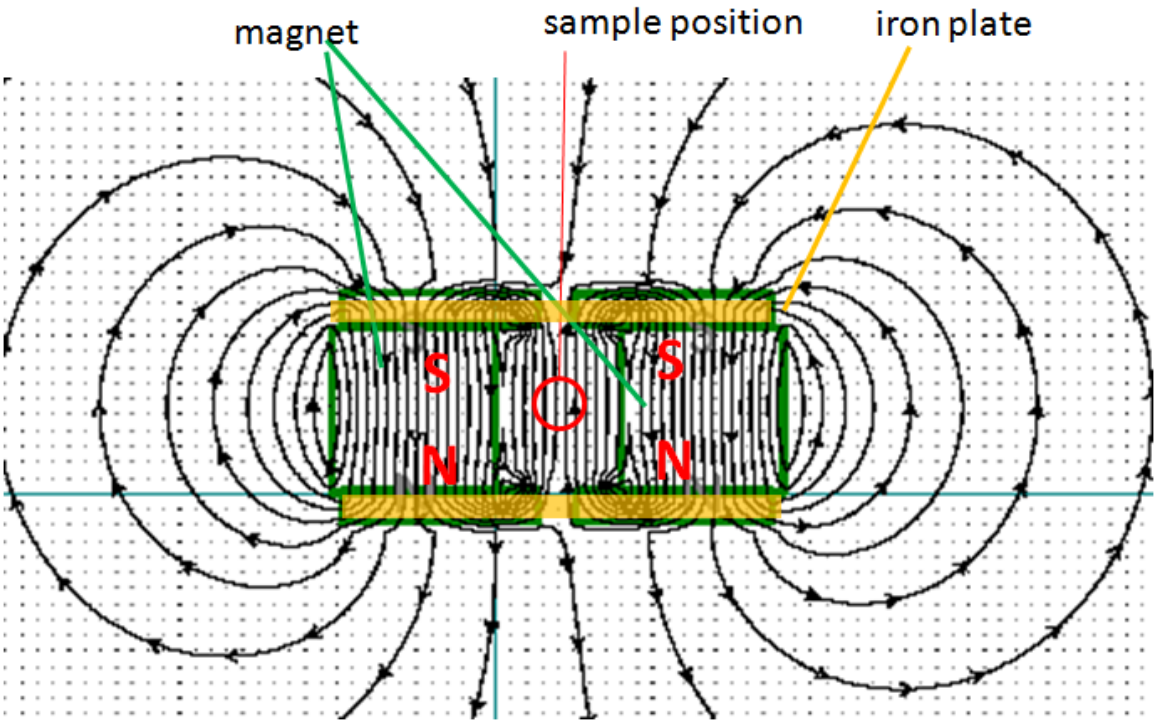

Figure 3.2 Simulation result of magnetic field lines created by two permanent magnets and two iron plate by freeware Vizmag. The green squares represent magnets, and yellow shades represent iron plates. The iron plates have a small hole in the center to let light passing through for Faraday rotation measurement. The magnetic field lines in the middle of two magnets are straight lines.

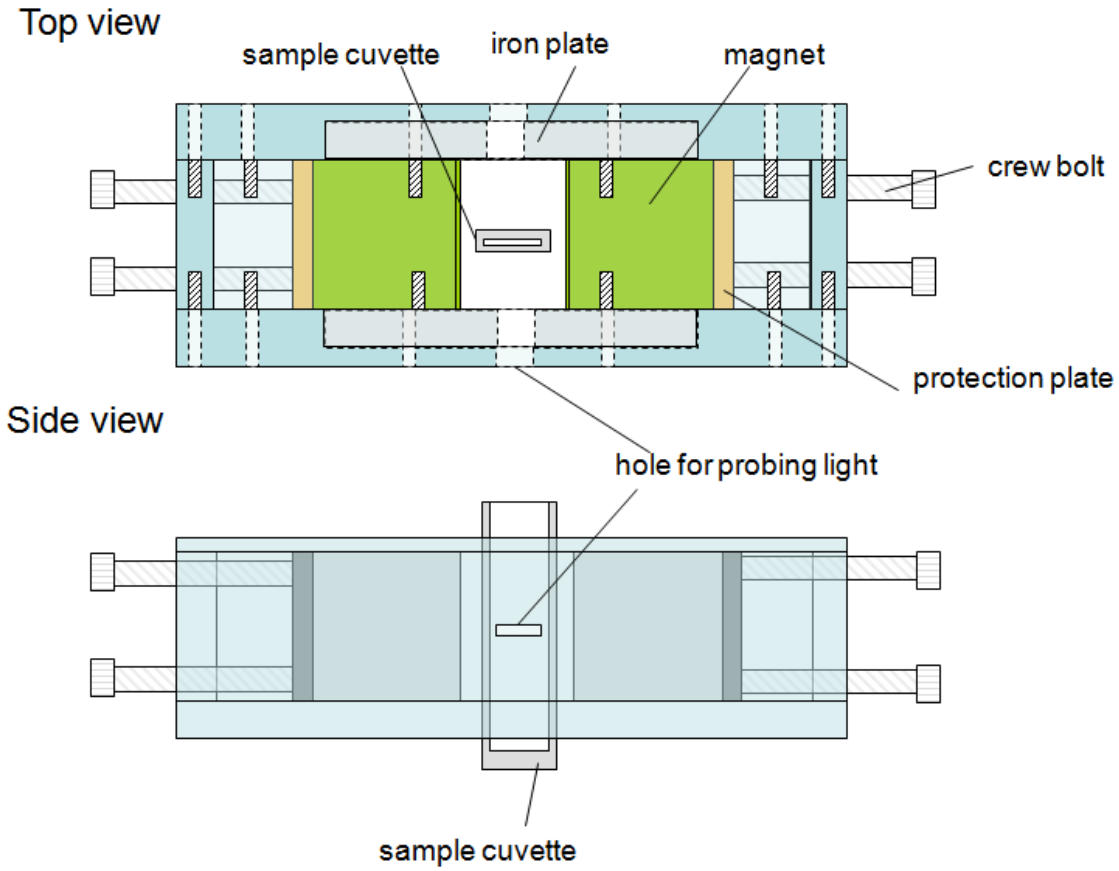

Figure 3.3 Schematic diagram of real design for Faraday rotation measurement. The crew bolts are used to push magnets.

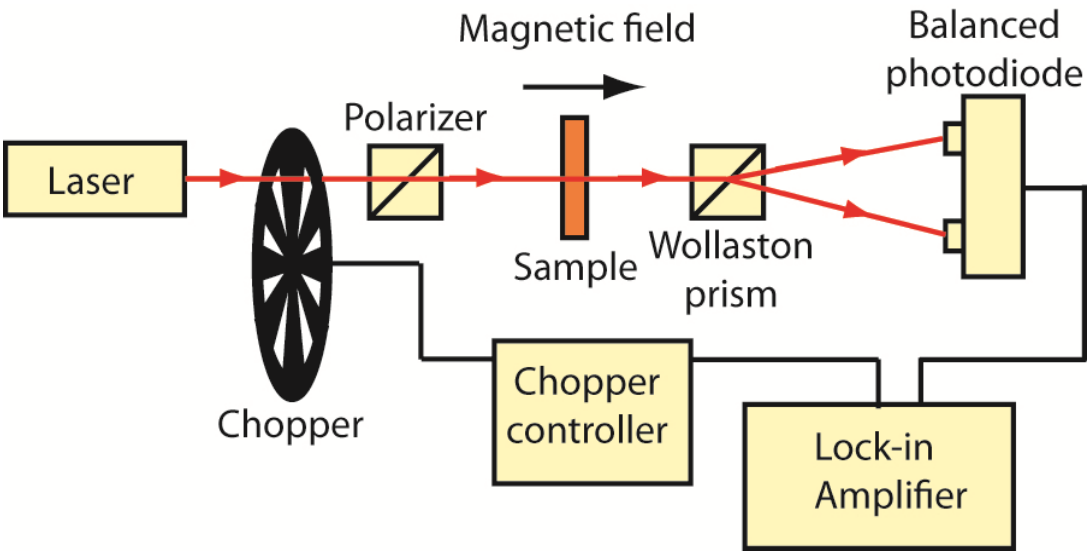

Figure 3.4 Experimental setup for static Faraday rotation measurement.

equal intensities. A pair of balanced photodiodes measures the difference between the intensities of the two beams. The iron oxide nanocrystal solution in 1 mm-thick quartz cuvette was placed between the polarizer and Wollaston prism under 0.32 T of external magnetic field applied parallel to the direction of the laser beam. Wollaston prism is a beamsplitter, and it would split the beam into two orthogonal polarization components (vertical and horizontal). When the polarization of light before Wollaston prism was set 45^{o} from vertical direction, the intensities of two orthogonal polarization components would be the sample. Without sample, the output from balanced photodiode should be zero. After placing sample inside, FR angle (θ) was obtained from the difference in intensities of the two orthogonal polarization components (I_v and I_h) normalized to the total intensity of the laser beam, $\theta \propto |I_v\text{-}I_h|/(I_v+I_h)$ for a small rotation angle, shown in Figure 3.5. The actual rotation angle can be obtained by a simple mathematical calculation $|I_v\text{-}I_h|/(I_v+I_h) = |\cos(45+\theta)\text{-}\sin(45+\theta)|/ (\cos(45+\theta)+\sin(45+\theta))$. The correlation between FR angle (θ) and $2|I_v\text{-}I_h|/(I_v+I_h)$ was shown in Figure 3.6.

Faraday rotation data of Fe_3O_4 and γ-Fe_2O_3 as a function of sample concentration was shown in Figure 3.7. Faraday rotation was obtained from blank sample (solvent in cuvette), and it may be contributed from the cuvette and solvent. In order to remove the background signal from quartz cuvette and solvent, FR of the nanocrystals was measured by taking the slope of θ vs. concentration of the nanocrystal solution. FR signal of iron oxide nanocrystals increased linearly to the sample concentration indicating that interparticle interaction are negligible within the concentration range of our study.

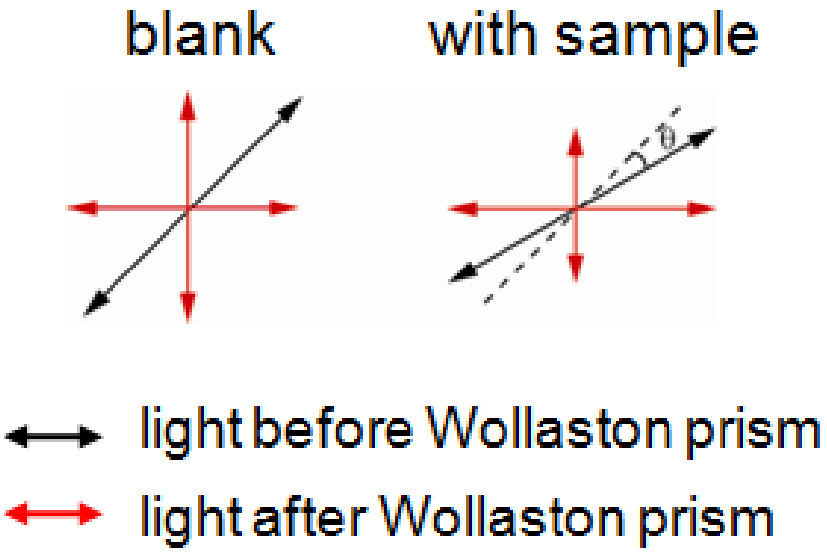

Figure 3.5 Schematic diagram illustrated the intensities of vertical and horizontal component after passing through Wollaston prism.

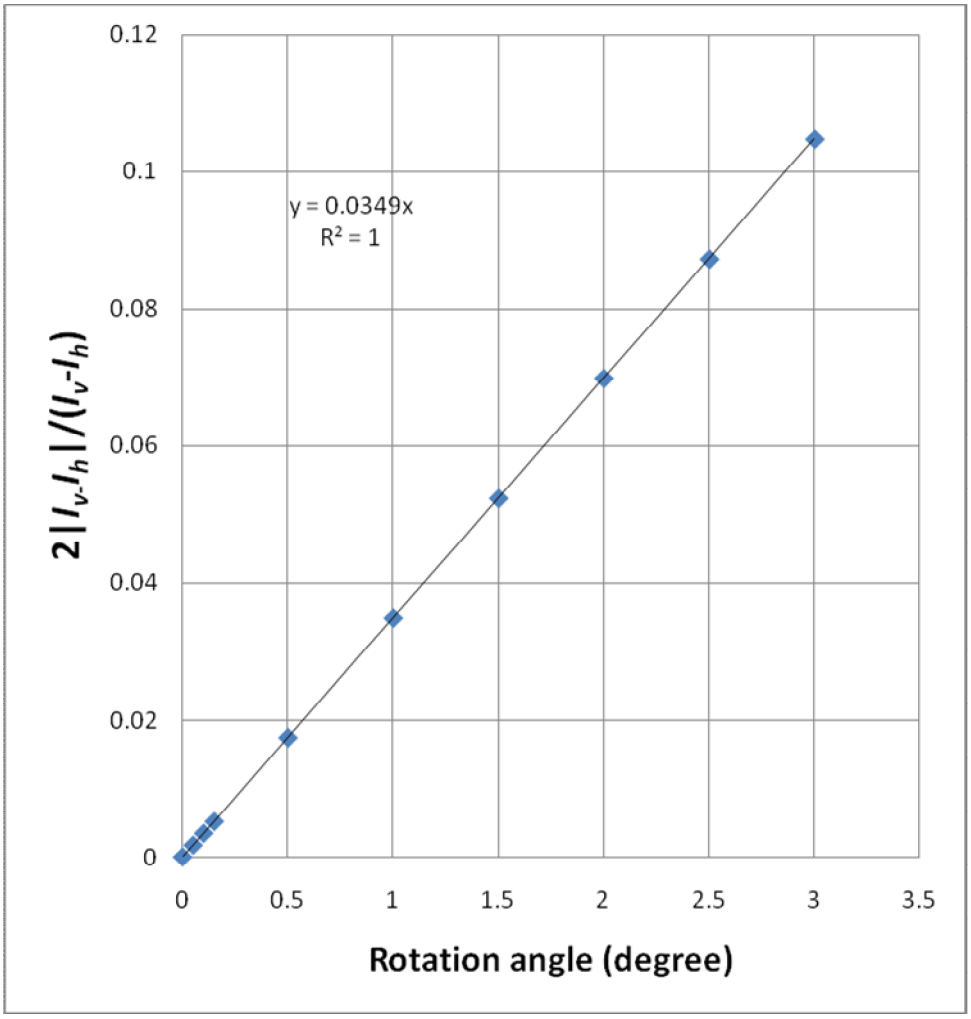

Figure 3.6 A plot of FR angle (θ) versus $2|I_v\text{-}I_h|/(I_v+I_h)$. The actual Faraday rotation angle can be calculated by using this correlation.

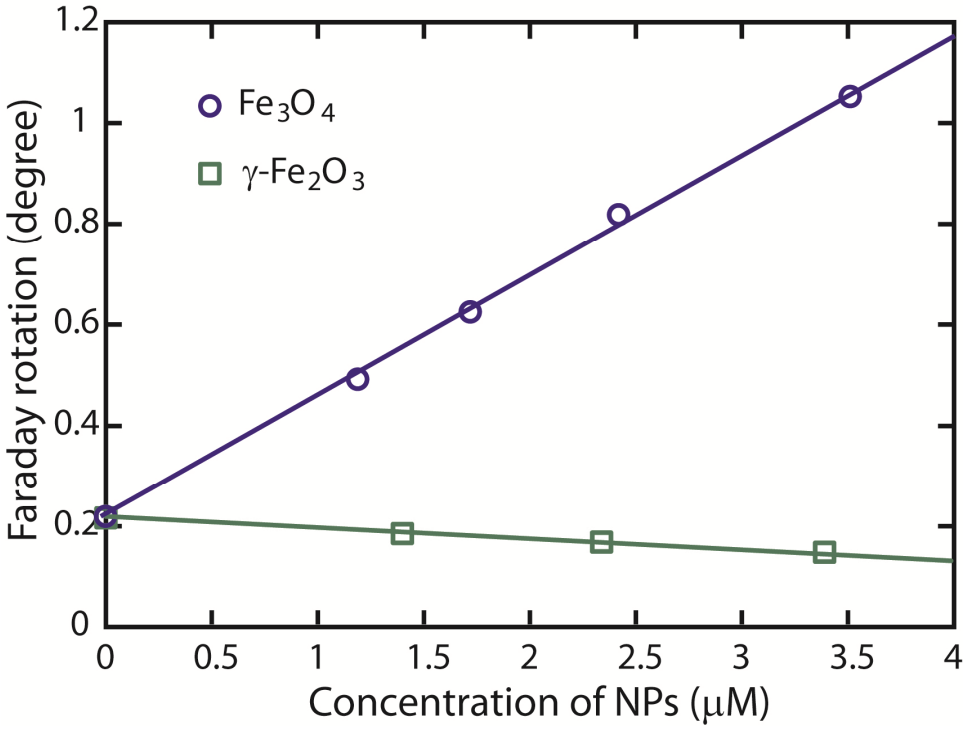

Figure 3.7 Faraday rotation data of Fe_3O_4 and γ-Fe_2O_3 as function of sample concentration.

3.2.2 *Time-resolved Faraday rotation for magnetization dynamics measurement*

Time-dependent magnetization of the photoexcited Fe_3O_4 nanocrystals was monitored by time-resolved Faraday rotation measurements. Faraday rotation is proportional to $\vec{M}(t)\cdot\vec{k}$, where $\vec{M}(t)$ and $\vec{k}$ are the magnetization vector of the nanocrystal and wavevector of the probe light, respectively.[51] Due to the high temporal resolution, time-resolved Faraday rotation and the related technique of magneto-optic Kerr effect have been widely utilized in the study of the ultrafast magnetic responses.[26, 45, 52-54] A schematic diagram of the experimental setup is shown in Figure 3.8. Linearly polarized pump pulses (780 nm, 60 fs, 3 kHz) excited the free-streaming jet (400 μm thick) of nanocrystals at room temperature and under the external magnetic field of 0.32 T. The sample solution was circulated as a jet form to prevent potential sample damage and accumulated thermal effects due to the repeated exposure of the same sample area to the pump pulses, shown in Figure 3.9. The linearly polarized probe pulses at 620 or 900 nm, derived from white light continuum, were used to monitor the time-dependent Faraday rotation of the photoexcited samples. The excitation fluence was varied in the range of 15-61 mJ/cm^2 resulting in the corresponding average excitation density in the range of 3-12 %. The approximate average excitation density was estimated from the concentration of the nanocrystals and the absorbed excitation pulse energy. The concentration of nanocrystals was kept low to maintain the average inter-particle distance much larger than the size of the nanocrystal (e.g., factor of ~ 10).

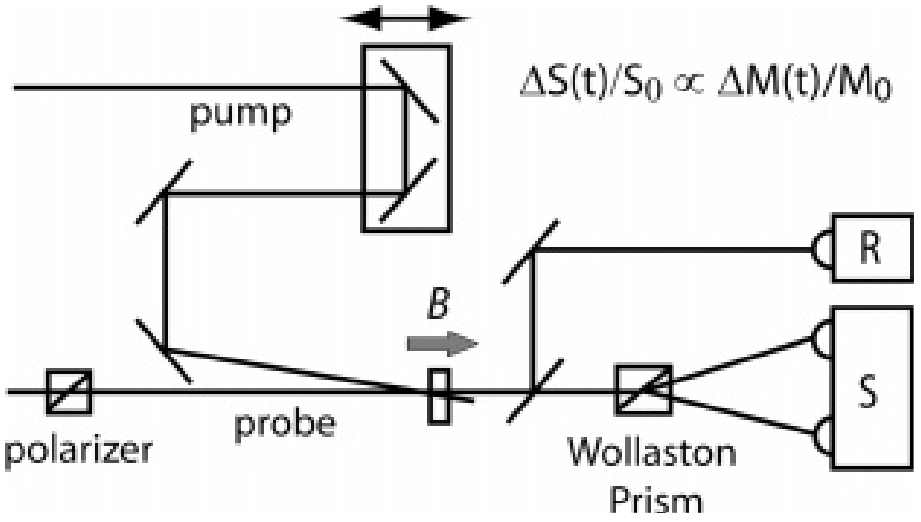

Figure 3.8 Schematic diagram of the time-resolved Faraday rotation measurement. The external magnetic field (*B*) was provided by a pair of permanent magnets, whose polarity was set either parallel or perpendicular to the direction of the probe light.

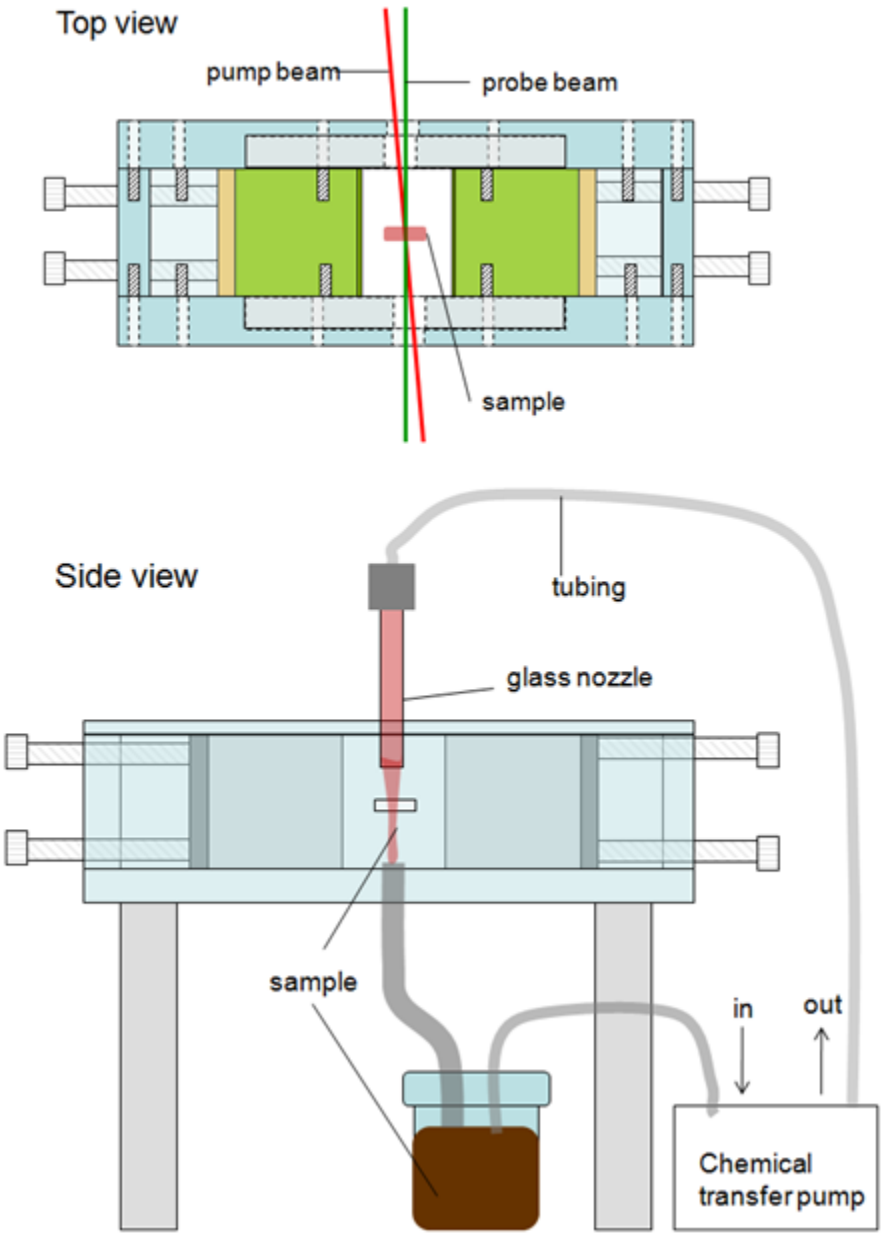

Figure 3.9 Schematic diagram of sample circulation system.

Magnetic dipolar interaction between the nanocrystals is insignificant at these concentrations and should not affect the dynamics of the magnetization.[55] Combination of a Wollastonprism and a balanced photodiode pair was used to measure the Faraday rotation, which is proportional to the output signal from the balanced photodiode normalized to the transmitted probe intensity, S/R, for a small rotation angle. Fractional changes of magnetization induced by the optical excitation was obtained by measuring $\Delta S/S_0$, where $\Delta S = [S_{(\text{pump on})} - S_{(\text{pump off})}]/R$ and $S_0 = S_{(\text{pump off})}/R$, respectively. The measured signal $\Delta S/S_0$ in this study reflects in principle the complex Faraday rotation with contributions of circular birefringence and dichroism, both of which are linear to the magnetization.[50]

3.2.2 *Pump-probe transient absorption measurement*

Pump-probe transient absorption measurement was made on an amplified Ti:sapphire laser, which produced pulses of 60 fs centered at 780 nm at 3 kHz repetition rate. Figure 3.10 shows the schematic diagram of experimental setup. For the probe beam, a white light continuum generated by focusing 780 nm beam on a 2 mm thick sapphire crystal was used. The probe beam passed through a prism dispersion compensator, which was also used to preselect the wavelength of the probe light before the sample. Pre-selection of the probe wavelength greatly diminished the artifact near zero time delay arising from the cross-phase modulation under intense excitation. Typical pump-probe cross correlation and step size were 70 and 10 fs, respectively. Pump and probe beam diameters were 150 and 30 μm, respectively.

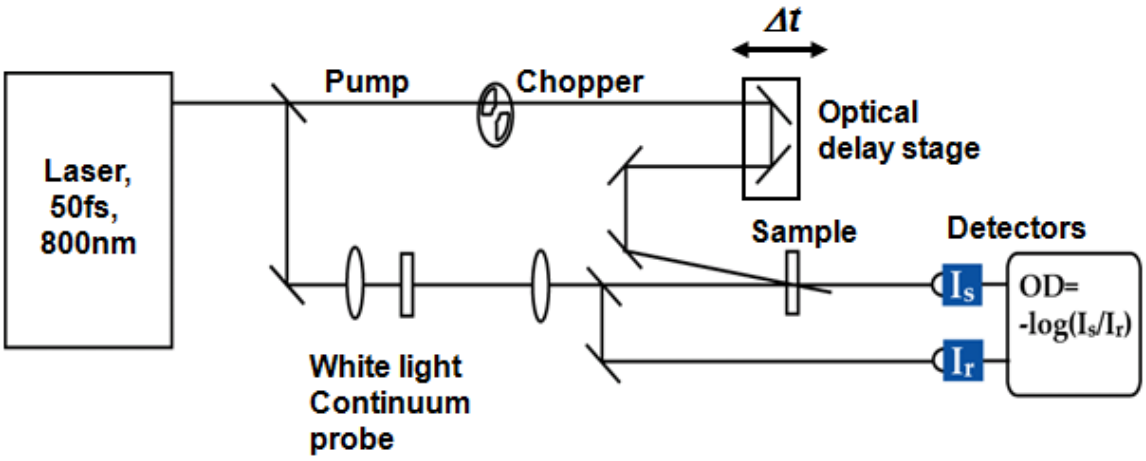

Figure 3.10 Schematic diagram of the transient absorption measurement. I_s represents the intensity of light after passing through the sample, and I_r represent the reference intensity, namely the intensity of light without passing through the sample. The sample was circulated prevent potential damage or heat circulation under continuous exposure to intense laser beam.

3.3 Analysis of time-resolved Faraday rotation data

Figure 3.11 shows the representative pump-probe Faraday rotation data of 7.5 nm Fe_3O_4 nanocrystals under Voigt and Faraday geometries. The probe light propagates in the direction perpendicular and parallel to the external magnetic field for Voigt and Faraday geometry, respectively. Under the Voigt geometry, Faraday rotation exhibits essentially no dynamic response except a spike near zero time delay originating from optical Kerr effect. Under the Faraday geometry, an immediate decrease of Faraday rotation was observed with the subsequent recovery of the signal on two distinct time scales. The opposite polarity of the external magnetic field yielded signals with the opposite sign (ΔS_1 and ΔS_2), because the Faraday effect is odd with respect to the magnetic field.[50] To remove any potential nonmagnetic feature in the dynamics, the difference between ΔS_1 and ΔS_2 were taken to obtain the time-dependent magnetization throughout the measurements.

No signature of a precession of the magnetization vector was observed up to 3 ns of delay time for both Faraday and Voigt geometries. The lack of precessional signature may be due to negligible photoinduced reorientation of the magnetization or critical damping of the precession.[47, 56] If the reorientation of the magnetization can be ignored, the fractional Faraday rotation ($\Delta S/S_0$) can be interpreted as the fractional changes in the amplitude of the magnetization ($\Delta M/M_0$) in the nanocrystals.

In Figure 3.12, pump-probe transient absorption (ΔOD) and magnetization data ($\Delta M/M_0$) are shown together to compare the electronic and magnetic responses to the ultrafast optical excitation. For an easy comparison of the dynamics, the sign of the

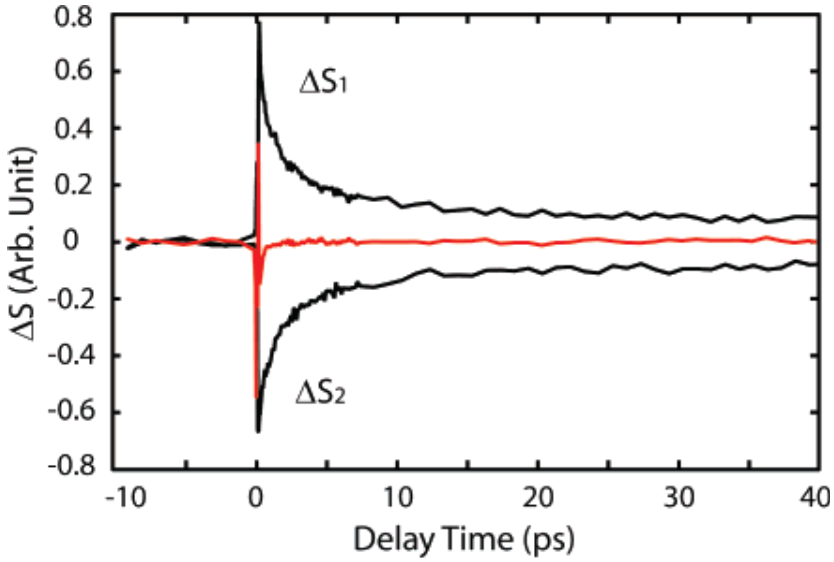

Figure 3.11 Time-resolved Faraday rotation of Fe_3O_4 nanocrystals (7.5 nm). ΔS_1 and ΔS_2 were obtained under Faraday geometry with the two opposite polarities of the external magnetic field. For these two curves, the signal obtained without the external magnetic field was subtracted. The red curve is obtained under Voigt geometry.

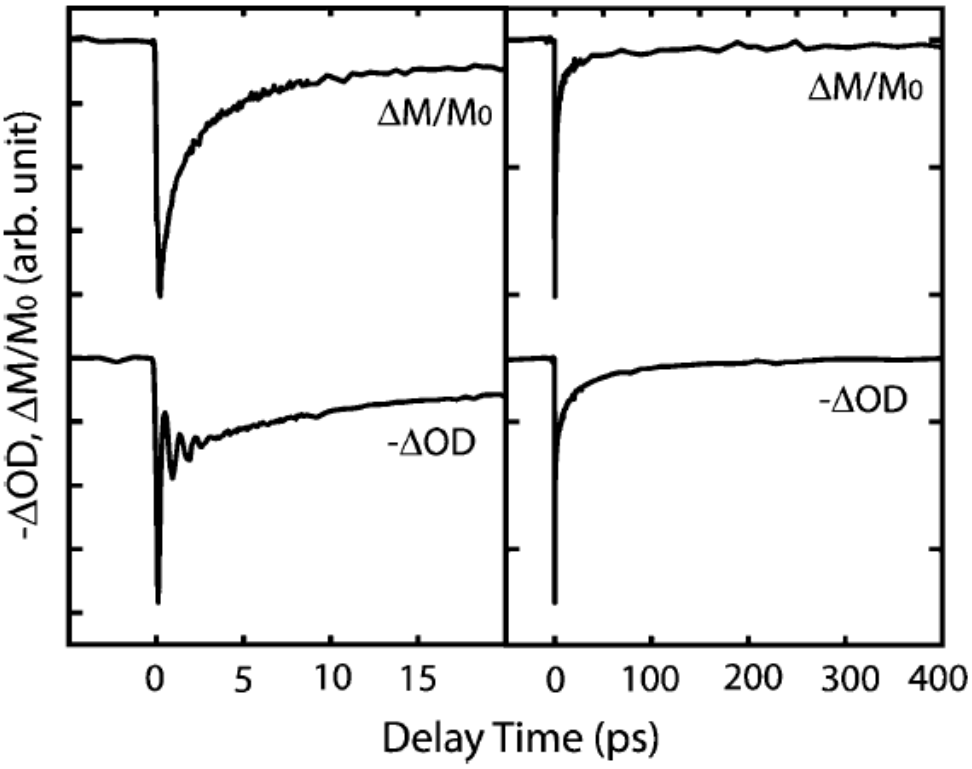

Figure 3.12 Comparison of the transient absorption (-ΔOD) and magnetization ($\Delta M/M_0$). The left and right panels display the same data set in different time windows.

transient absorption data is reversed in the figure. The transient absorption data exhibit pump-induced absorption in the broad range of visible and near-infrared probe wavelengths, which decays on multiple time scales with exponential time constants of τ= ~ 20 and ~ 200 ps. The time scales of the dynamics were weakly dependent on the probe wavelengths within the range 550-900 nm, while the amplitude varied with the wavelength, shown in Figure 3.13. The oscillations at early delay times are due to the coherent acoustic phonon.[57] On the other hand, dynamics of magnetization exhibits noticeable differences from the transient absorption at delay times earlier than 20 ps, while they exhibit comparable dynamics on much slower time scales. The initial recovery of the magnetization ($\Delta M/M_0$) following the ultrafast demagnetization occurs on ~ 20 picoseconds time scale and carries a larger fraction of recovery amplitude. This component of the dynamics is absent in the transient absorption data. The oscillatory features are not observable unlike in transient absorption data indicating that the coherent lattice motion does not have a measurable effect on $\Delta M/M_0$ in this study. The slower recovery component of the magnetization occurs with exponential time constants of τ = ~ 200 ps, which are similar to the transient absorption data. The measured $\Delta M/M_0$ is independent of the probe wavelength exhibiting essentially identical dynamics at 620 and 900 nm, shown in Figure 3.14.

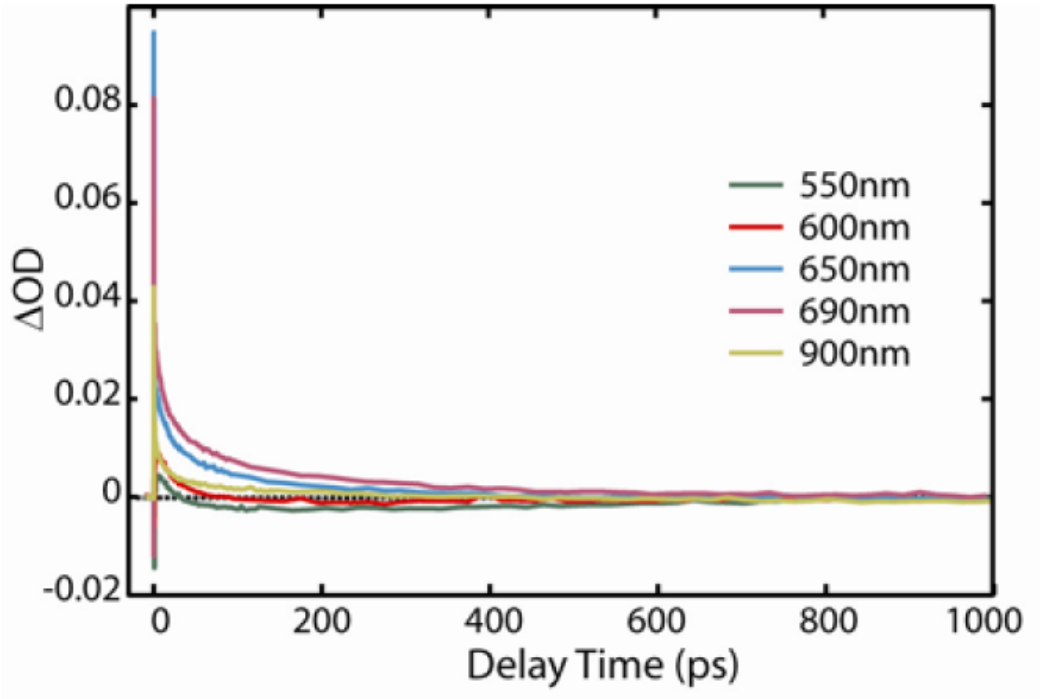

Figure 3.13 Transient absorption (ΔOD) probed at different wavelength (550-900nm).

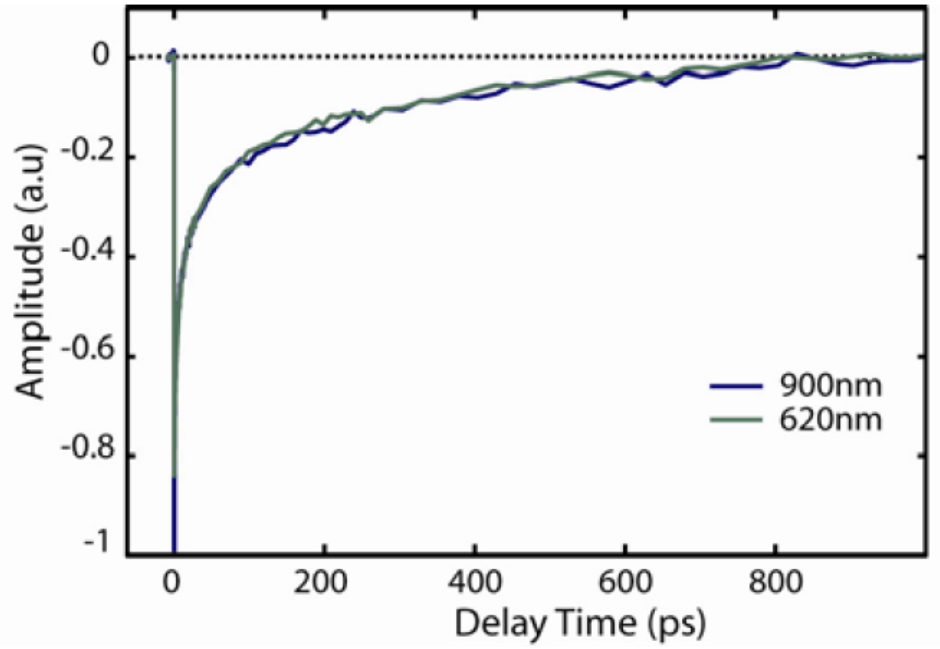

Figure 3.14 Transient magnetization ($\Delta M/M_0$) probed at two different wavelengths (620-900 nm).

The immediate decrease of $\Delta M/M_0$ following the optical excitation in ~ 100 fs is assigned to the ultrafast demagnetization by the destruction of the ferrimagnetic ordering upon the optical excitation. Optically induced demagnetization on subpicosecond time scale was previously observed on the surface of many ferro- and ferrimagnetic materials,[19, 26] although the exact mechanism has been debated for many years. Demagnetization by the equilibration of the laser heated lattice and spin system via usual spin-lattice interaction is unlikely because the time scale for such process typically exceeds 100 ps. Various mechanisms of optically induced ultrafast demagnetization were proposed such as spin-flip electron scattering, femtosecond spin-lattice relaxation, spin-orbit coupling during coherent excitation, magnon excitation by fast relaxing electrons or carriers, etc.[28, 43, 58, 59] Despite the recent progresses, understanding the microscopic mechanisms of ultrafast demagnetization continues to be a challenge because the pathways allowing the flow of both the energy and spin angular momentum on the relevant time scales need to be identified.[60]

To obtain a deeper and more quantitative understanding of the dynamics of the demagnetization and its recovery, $\Delta M/M_0$ was measured at various excitation fluences. Figure 3.15a shows the time-dependent $\Delta M/M_0$ of 4.5 nm Fe_3O_4 nanocrystals as a function of the excitation fluence. The peak value of $\Delta M/M_0$ negatively increases with the excitation density and saturates near -1, that is, almost complete demagnetization, at the excitation fluence of 46 mJ/cm^2 corresponding to ~ 10% excitation density as shown in Figure 3.15b. This suggests that each absorbed photon initially destroyed the magnetic ordering in ~ 10 times larger number of metal ions for 4.5 nm Fe_3O_4 nanocrystals. A

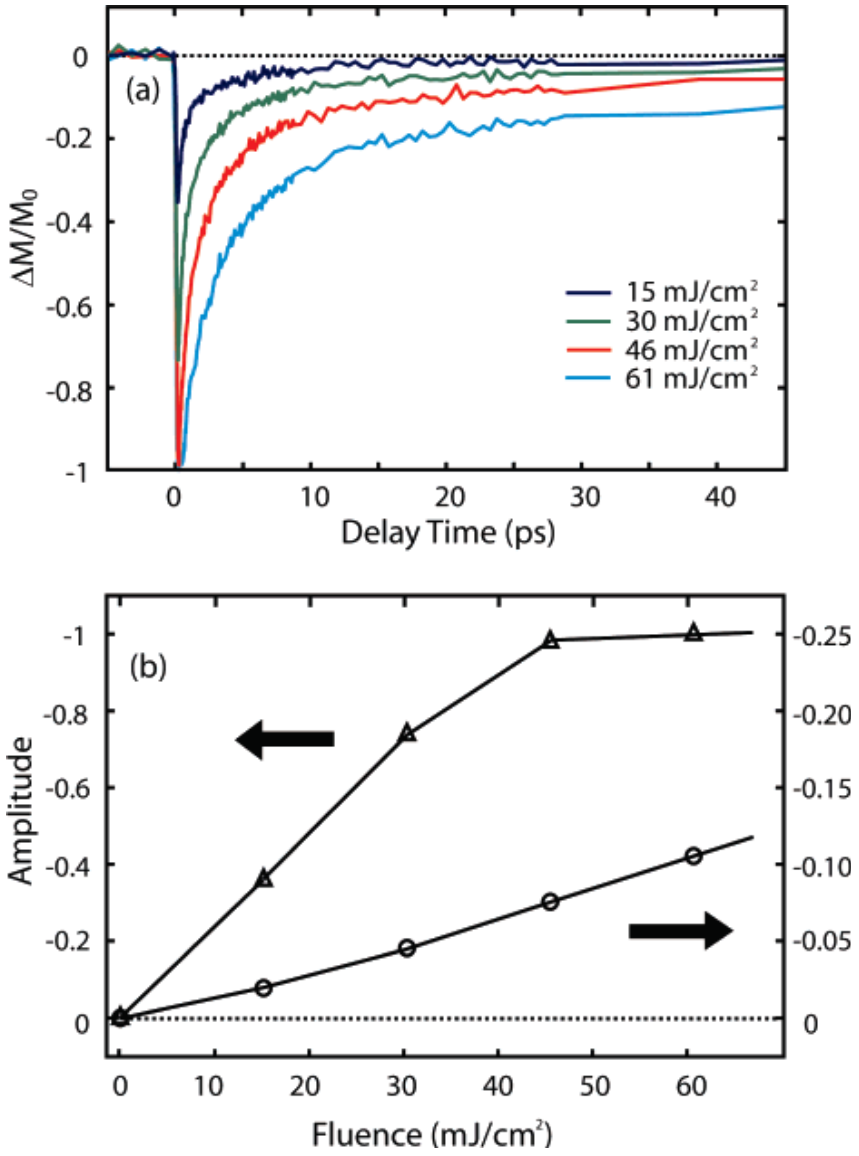

Figure 3.15 (a) Excitation fluence dependence of $\Delta M/M_0$ of 4.5 nm Fe_3O_4 nanocrystals. (b) Excitation fluence dependence of the amplitudes in $\Delta M/M_0$. Triangle: peak amplitude of $\Delta M/M_0$. Circle: amplitude of the exponential fit for τ = 200 ps recovery component. Solid lines superimposed on the marks are guides to an eye.

similar degree of the destruction of the magnetic ordering by the optical excitation was observed earlier in ferromagnetic chalcogenide surfaces.[19]

While their relative amplitudes vary as a function of the excitation fluence, the biphasic feature of the recovery, that is, fast (τ < 20 ps) and slow (τ =200 ps) phases, is maintained in the entire range of the excitation fluence of this study. For τ =200 ps component, the amplitude increases slightly superlinearly to the excitation fluence; see Figure 3.15b. Slight superlinearity is due to an additional contribution of the multiphoton absorption, which was also observed in the transient absorption data, shown in Figure 3.16. The fact that the slow magnetization recovery and transient absorption occur on comparable time scales and that they exhibit similar excitation fluence dependence suggest that slow magnetization recovery reflects the relaxation of the excited-state to the ground state. On the other hand, the fast recovery component of magnetization, carrying the larger fraction of the amplitude, does not have a corresponding feature in the transient absorption data.

To obtain a further insight into the magnetization dynamics and their dependence on the size of the nanocrystals, $\Delta M/M_0$ was measured for Fe_3O_4 nanocrystals of three different sizes. Figure 3.17a compares $\Delta M/M_0$ of 4.5, 7.5, and 10 nm Fe_3O_4 nanocrystals. The excitation density and the optical density at the probe wavelength were kept nearly the same for all three samples for this comparison. $\Delta M/M_0$ exhibits a strong dependence on the size of the nanocrystal, especially for its amplitude, while the biphasic recovery is observed for all the sizes.

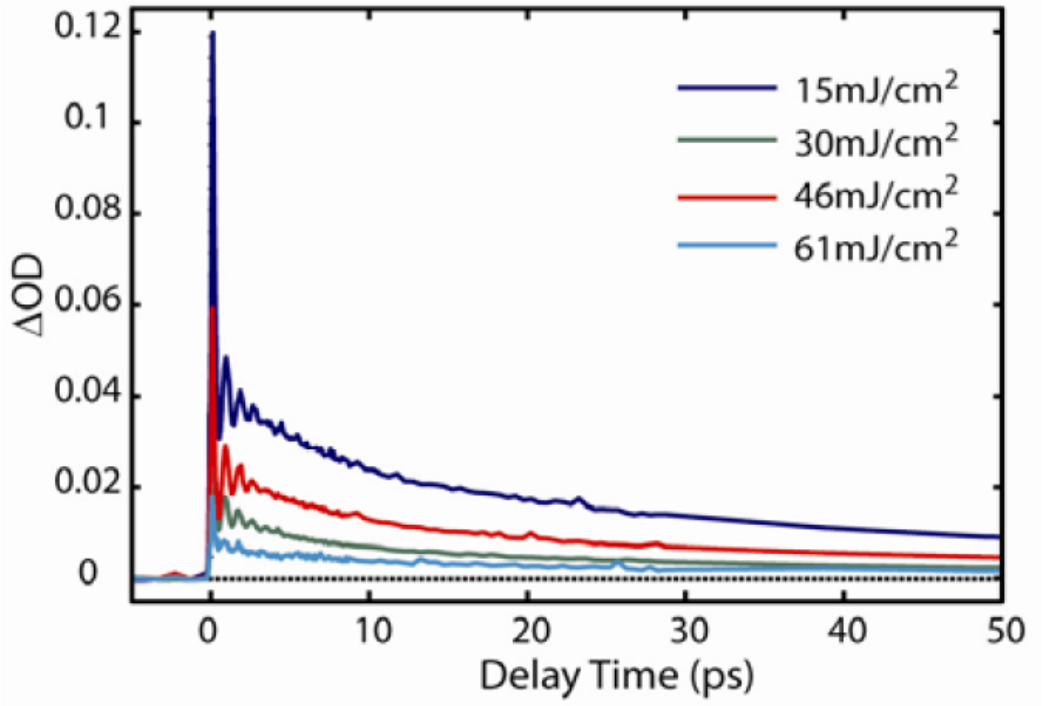

Figure 3.16. Excitation fluence dependence of ΔOD of 4.5 nm Fe_3O_4 nanocrystals.

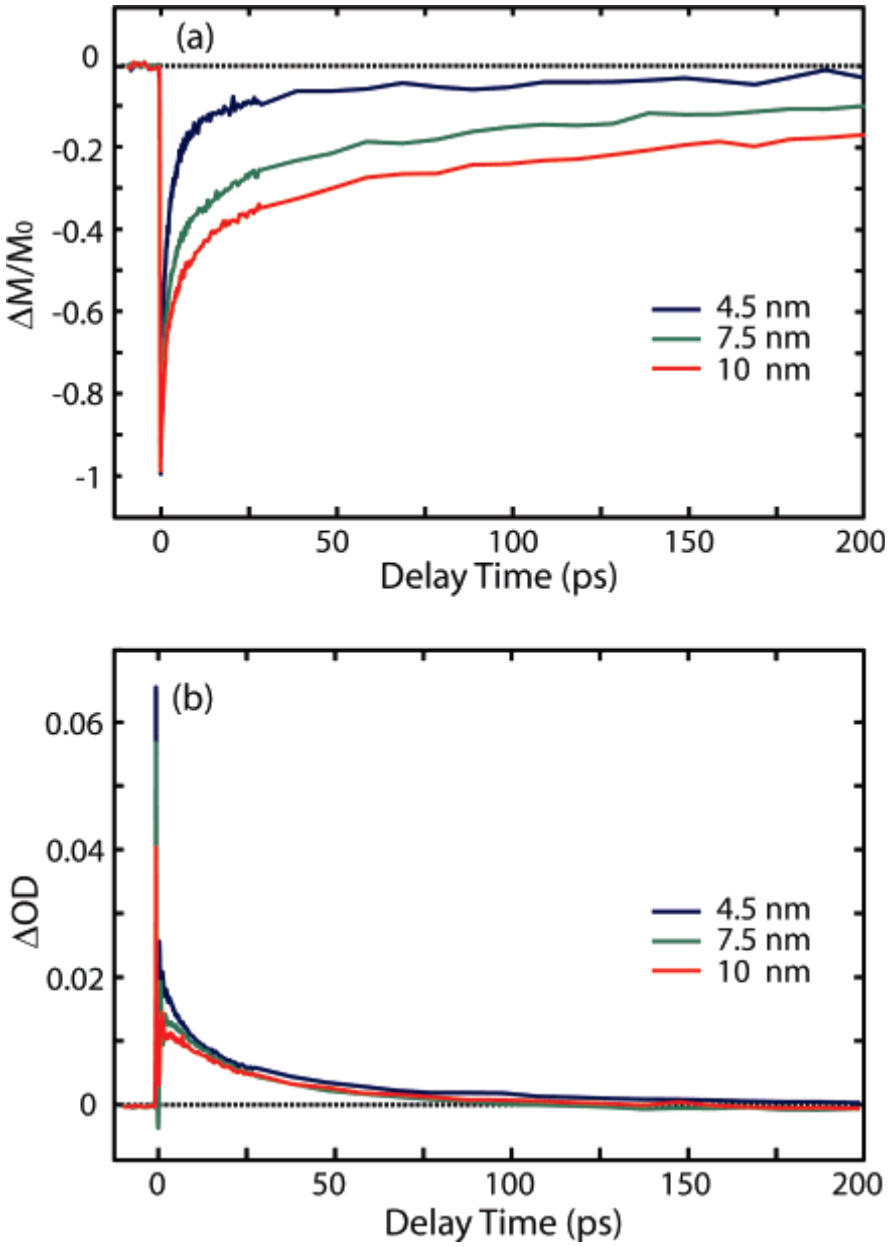

Figure 3.17 Size-dependent $\Delta M/M_0$ (a) and ΔOD (b) of Fe_3O_4 nanocrystals at the excitation fluence of 46 mJ/cm^2. The amplitude of slower recovery component of $\Delta M/M_0$ increases with the size of the nanocrystal while ΔOD exhibits no strong size-dependence.

This is in contrast to the transient absorption data shown in Figure 3.17b, which do not exhibit significant size-dependent dynamics except at very early delay times. For the fast recovery component of $\Delta M/M_0$, its relative contribution to the overall recovery dynamics becomes smaller as the size of the nanocrystal increases. On the other hand, the amplitude of the slow recovery component increases significantly with the size. The time scales of the magnetization recovery exhibit a slight increase as the size of the nanocrystal increases. The detail of size dependent spin-lattice rate will be discussed in Chapter IV.

The increase of the amplitude for the slow recovery component of $\Delta M/M_0$ with the size of the nanocrystals indicates that photoexcitation has a stronger influence on the destruction and recovery of the magnetic ordering for the larger nanocrystals. Size-dependent lattice temperature due to different cooling rate, which is in quasi-equilibrium with the spin degrees of freedom, cannot explain the above size dependence. The temperature increase in the lattice is estimated to be less than 100 K under the present experimental condition during the first several picoseconds from the temperature-dependent coherent acoustic phonon frequency and temperature-dependent elastic moduli of typical ferrite materials.[61, 62] Langevin function describing the temperature and field dependence of the magnetization of superparamagnetic particles predicts.[63] $\Delta M/M_0$ should not be affected by more than a few percent for 7.5 and 10 nm nanocrystals.

3.4 Summary

In this chapter, the experimental setups of static Faraday rotation and time-resolved Faraday rotation were presented. Static Faraday rotation angle of Fe_3O_4 nanocrystals is much larger than γ-Fe_2O_3 nanocrystals for a given size and concentration. The magnetization relaxation after optically induced demagnetization in superparamagnetic Fe_3O_4 nanocrystals was studied by using time-resolved Faraday rotation. The results indicate the change of Faraday rotation represent the change of magnetization. The dynamics of the slowly recovering component of $\Delta M/M_0$ were well correlated with the dynamics of electronic relaxation, indicating electrons and spins reservoirs have reached their equilibrium. The size dependent amplitude $\Delta M/M_0$ is not due to size dependent lattice heating based on size dependent lattice temperature measurement, which may be contributed from the surface oxidation (see Chapter V).

CHAPTER IV

TIME-RESOLVED STUDY OF SURFACE SPIN EFFECT ON SPIN-LATTICE RELAXATION IN Fe_3O_4 NANOCRYSTALS*

4.1 Introduction

Investigation of the flow of energy and momentum in spin degrees of freedom in magnetic materials is now an important field of research since the electron spin is actively exploited as a new information carrier in addition to the electron charge.[2, 3] In ferromagnetic materials, the dynamics of spin excitation and relaxation has been actively investigated.[46] The relaxation of the spins requires the exchange of energy and angular momentum between the spin and lattice degrees of freedom, which is mediated by spin-orbit coupling. The effective strength of spin-orbit interaction in ferromagnetic solids is determined not only by the intrinsic atomic spin-orbit coupling strength but also by the ligand field that depends on the details of the local lattice structure and symmetry.[6, 7] In nanoscale magnetic materials, there are many surface spins under different ligand fields from those of the interior spins due to the structural discontinuity on the surface. Therefore, one would expect that the rate of energy and momentum transfer in spin degrees of freedom in nanoscale magnetic materials be significantly influenced by the surface spins.

---

* Reprinted in part with permission from *J. Am. Chem. Soc.*, *131* Hsia, C.-H.; Chen, T.-Y.; Son, D. H.; "Time-Resolved Study of Surface Spin Effect on Spin−Lattice Relaxation in Fe_3O_4 Nanocrystals" 9146, Copyright 2009 by the American Chemical Society.

In this chapter, we report the real-time measurement of the rate of spin-lattice relaxation in photoexcited colloidal Fe_3O_4 nanocrystals to obtain insight into the role of the surface spins in the equilibration dynamics of the photoexcited spins. While the effect of surface spins on superparamagnetic relaxation dynamics involving the directional fluctuation of the magnetization was investigated in earlier studies,[63-65] we address the dynamics of energy flow between the spin and lattice resulting in the time-dependent magnitude of the magnetization. From the analysis of the spin-lattice relaxation rates of the nanocrystals of various sizes using a simple model, we estimated the relative efficiency of the spin-lattice relaxation on the surface with respect to the interior in Fe_3O_4 nanocrystals.

To investigate the dynamics of spin relaxation in magnetic nanocrystals directly in the time domain, we employed a time-resolved Faraday rotation technique. Due to its high temporal resolution (<100 fs), time-resolved Faraday rotation is particularly useful for observing fast dynamics in spin degrees of freedom, although it probes only the relative change in magnetization via magnetooptic effect.[29] A colloidal solution of organically passivated Fe_3O_4 nanocrystals was chosen as the model system for this study. Systematic variation of the size and surface coordination readily achievable in Fe_3O_4 nanocrystals makes it particularly suitable for investigating the role of surface spins on the energy flow in the spin degrees freedom.[20] In our recent report,[36] size-dependent magnetization dynamics in photoexcited Fe_3O_4 nanocrystals were discussed with an emphasis on the magnitudes of the demagnetization and its recovery. In this study, we focus on the *rate* of equilibration of the magnetization following the

photoinduced demagnetization, which will be correlated with the average strength of spin-orbit interaction of the nanocrystals.

4.2 Experimental section

The synthesis and characterization of nanocrystals were covered in Chapter II. In this study, spherical Fe_3O_4 nanocrystals of five different sizes (5 ~ 15 nm in diameter) were used, and nanocrystals were suspended in cyclohexane for all the magnetization dynamics measurements. Time-resolved Faraday rotation was chosen to measure the magnetization dynamics, as described in Chapter III. The clean process and measurement were performed in the ambient condition, thus nanocrystals natural oxidation layers. The absorption spectra of Fe_3O_4 nanocrystals before and after exposure of laser were shown in Figure 4.1. Only very small change on absorption spectra was observed. The results suggest the identity of sample did not change during the period of time-resolved Faraday rotation measurement.

4.3 Results and discussion

Figure 4.1 shows the time-dependent Faraday rotation data obtained from the colloidal Fe_3O_4 nanocrystals 5-15 nm in diameter. The samples were photoexcited with 780 nm, 60 fs pulses at a fluence of 20-40 mJ/cm^2 while being continuously refreshed to avoid sample damage by the repeated excitation. In this measurement, the same excitation density was maintained for all the samples. Fractional change in Faraday rotation, $\Delta\theta(t)/\theta$, represents the time-dependent magnetization of the photoexcited

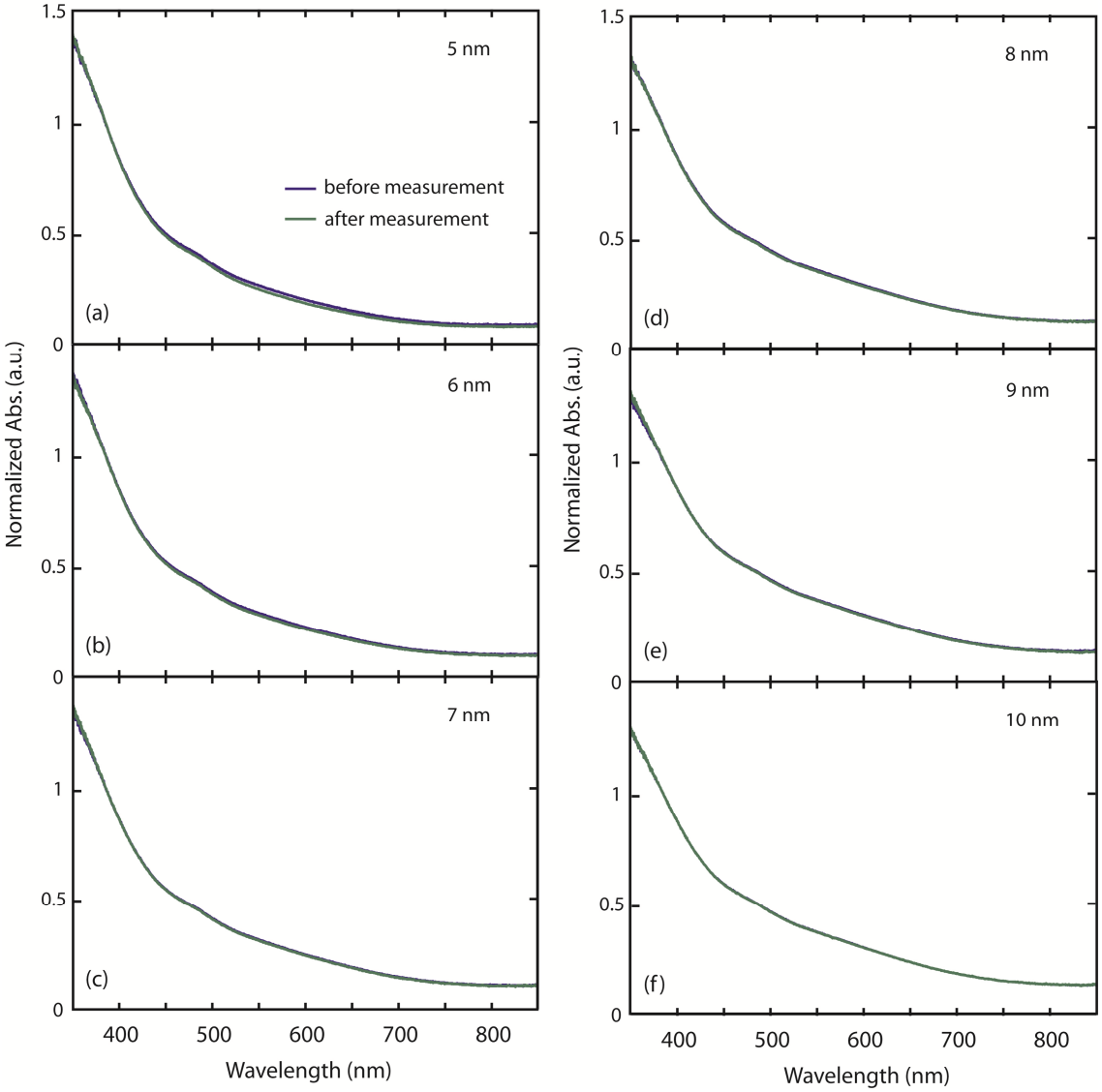

Figure 4.1 Absorption spectra of Fe_3O_4 nanocrystals with various sizes before and after time-resolved Faraday rotation measurement.

nanocrystals. Figure 4.2 shows time-dependent Faraday rotation data measured at two different wavelengths. The results indicate the time-dependent Faraday rotation data did not depend on the probing wavelength. General dynamic features of the data in Figure 4.3 are (i) sub-ps demagnetization following the excitation, (ii) recovery on ~10 ps scale, (iii) recovery on $\sim 10^2$ ps scale. Time scales of the recovery of $\Delta\theta(t)/\theta$ extracted from bi-exponential fitting of the data are summarized in Table 4.1.

The feature (i) has been previously observed in many metallic ferromagnets.[26, 28, 43] Such ultrafast demagnetization has been a topic of active research recently, which resulted in the discovery of a number of ultrafast spin-orbit coupling pathways. We will not discuss this process since it is beyond the scope of our discussion. Here, we focus on the dynamic feature (iii), occurring on the time scale τ_b = 250-350 ps. Justifications for relating τ_b to the time scale of spin equilibration via usual spin-lattice relaxation pathway are the following. First, τ_b has the correct order of magnitude for the spin-lattice relaxation time of $\sim 10^2$ ps expected for the ferromagnetic materials of transition metals.[6] In addition, τ_b in $Co_xFe_{3-x}O_4$ nanocrystals decreased with increasing content of Co that has a stronger spin-orbit interaction than Fe in a separate experiment. The data was shown in Figure 4.4. This strongly indicates that τ_b reflects the spin-lattice relaxation determined ultimately by the strength of the spin-orbit interaction. The origin of the faster dynamics (ii), an order of magnitude faster than the slower dynamics, is not entirely clear, although it may still reflect part of spin relaxation.

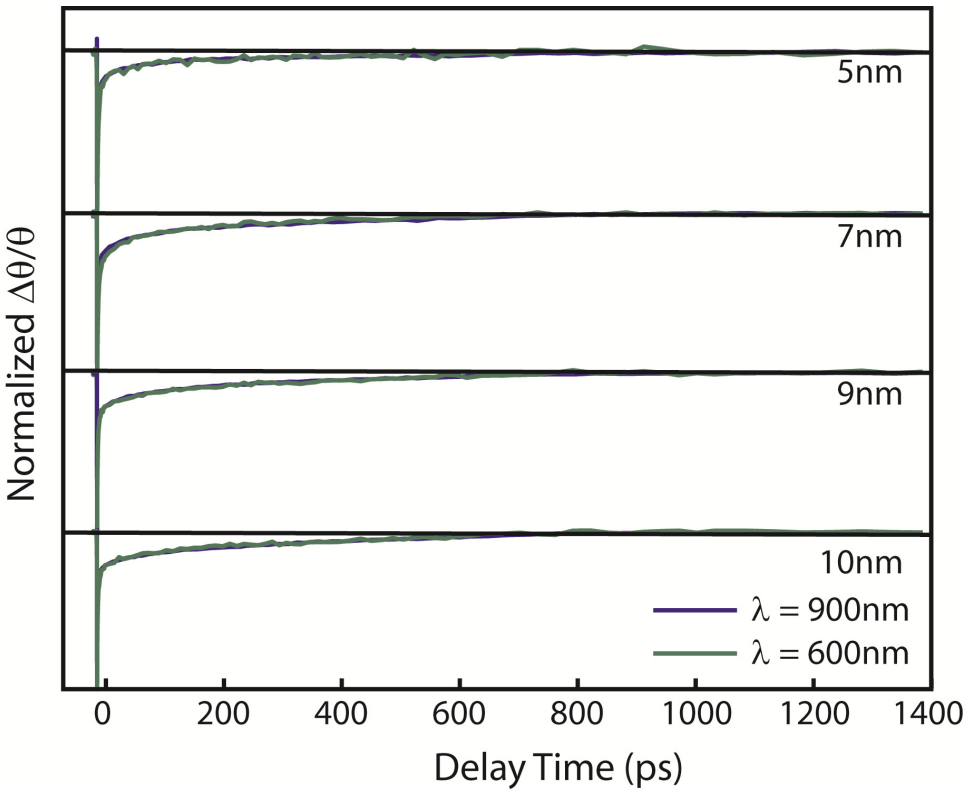

Figure 4.2 Time-dependent $\Delta\theta(t)/\theta$ of photoexcited Fe_3O_4 nanocrystals probed at two different wavelengths (600 and 900 nm).

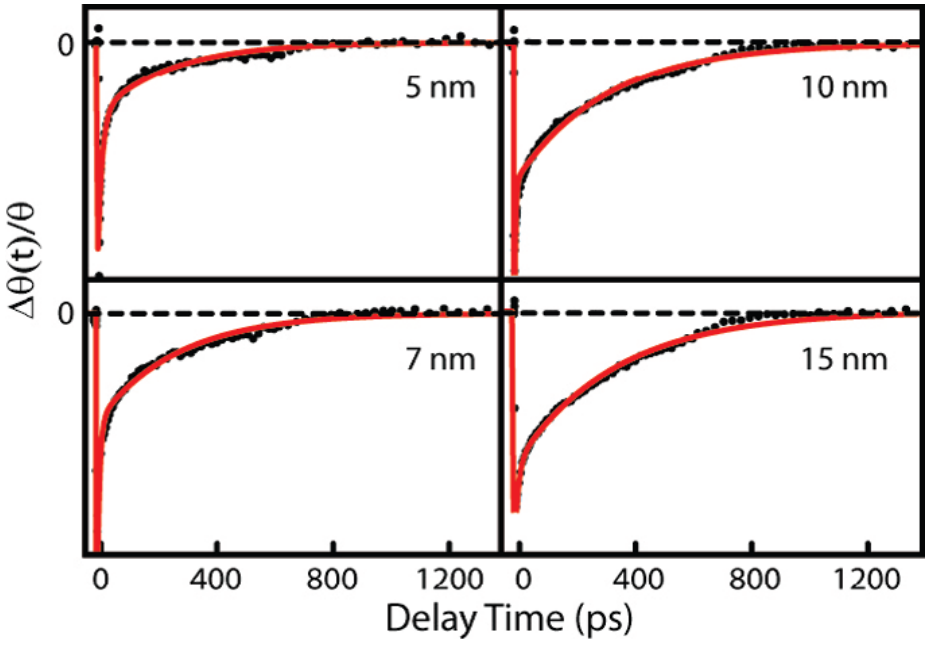

Figure 4.3 Time-dependent $\Delta\theta(t)/\theta$ of photoexcited Fe_3O_4 nanocrystals. Solid curves are the biexponential fit of the data.

Table 4.1 Time constants obtained from biexponential fit of $\Delta\theta(t)/\theta$.

Size *(nm)*	*5*	*7*	*9*	*10*	*15*
τ_a (ps)	22	29	32	24	12
τ_b (ps)	255±10	275±10	295±10	325±10	345±10

The feature (i) has been previously observed in many metallic ferromagnets.[26, 28, 43] Such ultrafast demagnetization has been a topic of active research recently, which resulted in the discovery of a number of ultrafast spin-orbit coupling pathways. We will not discuss this process since it is beyond the scope of our discussion. Here, we focus on the dynamic feature (iii), occurring on the time scale τ_b = 250-350 ps. Justifications for relating τ_b to the time scale of spin equilibration via usual spin-lattice relaxation pathway are the following. First, τ_b has the correct order of magnitude for the spin-lattice relaxation time of $\sim 10^2$ ps expected for the ferromagnetic materials of transition metals.[6] In addition, τ_b in $Co_xFe_{3-x}O_4$ nanocrystals decreased with increasing content of Co that has a stronger spin-orbit interaction than Fe in a separate experiment. The data was shown in Figure 4.4. This strongly indicates that τ_b reflects the spin-lattice relaxation determined ultimately by the strength of the spin-orbit interaction. The origin of the faster dynamics (ii), an order of magnitude faster than the slower dynamics, is not entirely clear, although it may still reflect part of spin relaxation.

τ_b obtained from the fitting of data was not sensitive to the wavelength of the probe light, unlike in transient absorption, as expected for $\Delta\theta(t)/\theta$ representing the magnetization dynamics.[29] At sufficiently low excitation intensities, τ_b was also independent of the excitation intensity, shown in Figure 4.5. On the other hand, τ_b increased from 250 to 350 ps as the size of the nanocrystal increased from 5 to 15 nm. We attribute the size dependence of τ_b mainly to the weaker average spin-orbit interaction in the larger nanocrystals as will be discussed below.

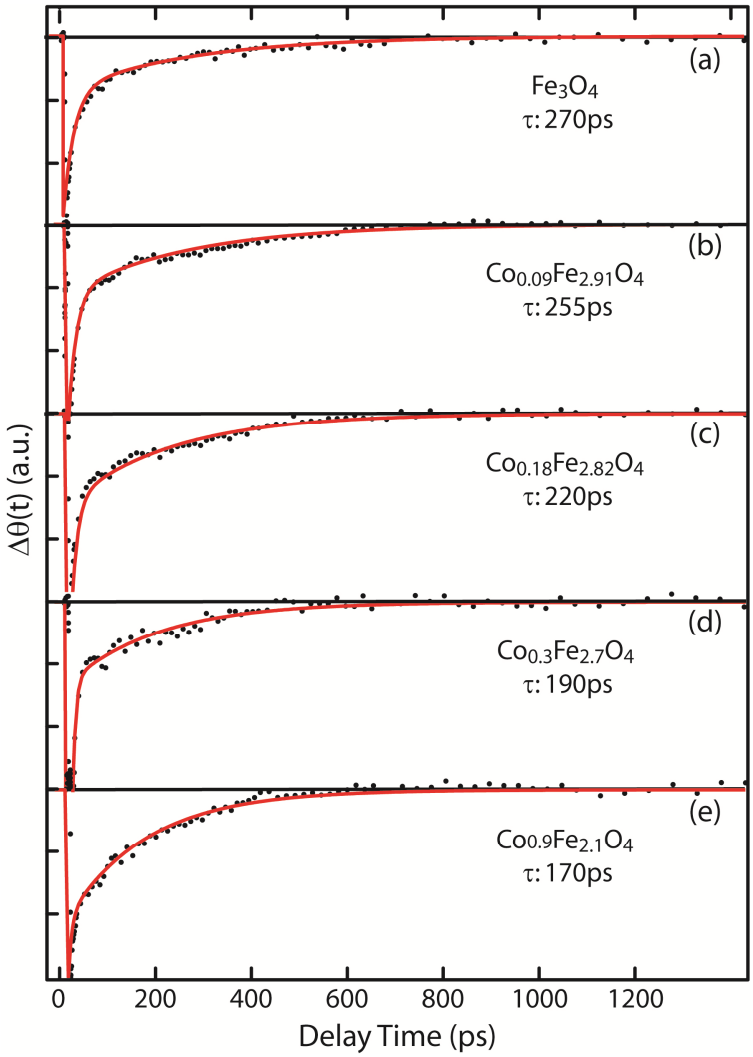

Figure 4.4. Cobalt content-dependent Δθ(t) data of 7 nm $Co_xFe_{3-x}O_4$ nanocrystals, x = 0, 0.09, 0.18, 0.3, and 0.9 for (a) to (e) respectively.

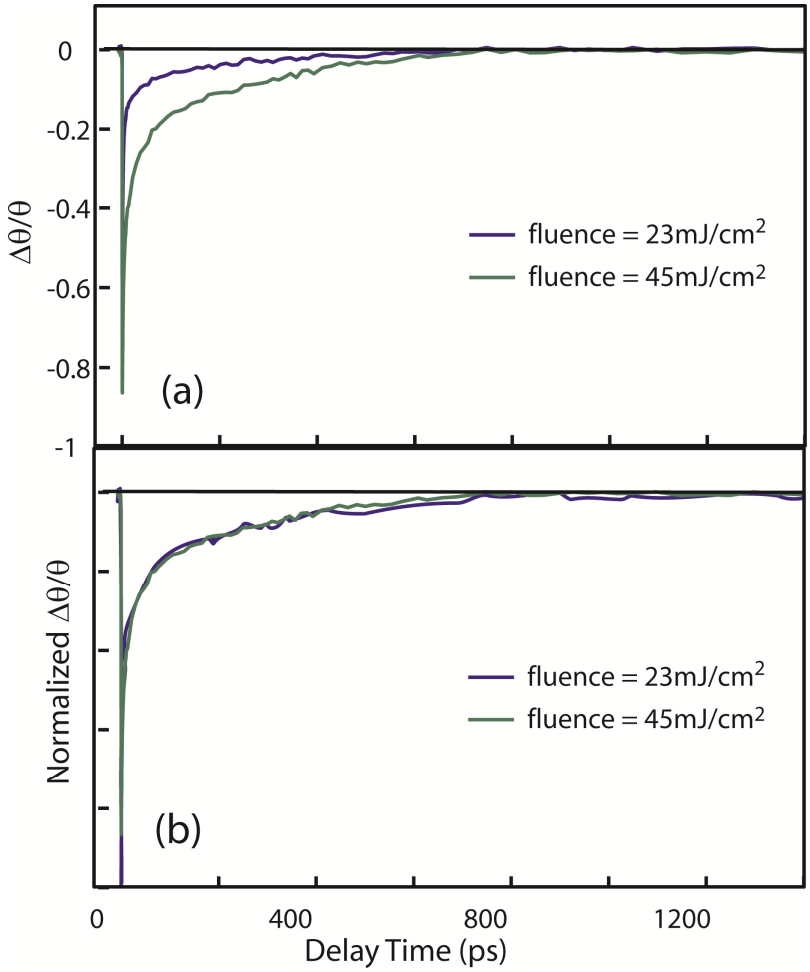

Figure 4.5. Pump fluence dependent Δθ/θ data of 7 nm Fe_3O_4 nanocrystals. (a) raw data, (b) normalized data. The data was normalized at time delay 200 ps. This normalized data demonstrate the spin-lattice relaxation in Fe_3O_4 nanocrystals is not depended on the excitation power when the power is still low.

According to Fermi's golden rule, spin-lattice relaxation rate ($1/\tau_b$) is proportional to the square of the coupling Hamiltonian term ($|\langle V \rangle|^2$) between the spin-orbit perturbed ligand field states, where the Hamiltonian V is the fluctuating electric potential of the ligand.[66] Here, we assume $|\langle V \rangle|^2$ of nanocrystals has contributions from the interior ($|\langle V_i \rangle|^2$) and the surface ($|\langle V_s \rangle|^2$) proportionally to the fraction of the interior (*fi*) and surface (*fs*) spins. A similar model incorporating the surface contribution in the energy relaxation has been used to explain exciton relaxation dynamics in quantum dots.[67]

$$1/\tau_b \propto \left|\langle V \rangle\right|^2 = f_i \cdot \left|\langle V_i \rangle\right|^2 + f_s \cdot \left|\langle V_s \rangle\right|^2 \qquad (1)$$

Using this model, we estimated the relative efficiency of the surface in spin-lattice relaxation with respect to the interior. The values of f_i and f_s depend on the thickness (t) of the surface region, which is somewhat arbitrary. In our analysis, we chose the values of t between 3 and 5 Å that contain the outermost atomic layer. By comparing the variation of $1/\tau_b$ with the variation of $|\langle V \rangle|^2$ on the nanocrystal size, we obtained $|\langle V_s \rangle|^2/|\langle V_i \rangle|^2 \approx 3$ for t =4 Å. Comparison of the relative values of $1/\tau_b$ and $|\langle V \rangle|^2$ as a function of the nanocrystal diameter is shown in Figure 4.6.

This result indicates that the surface of the Fe_3O_4 nanocrystal is 3 times more efficient than the interior for spin-lattice relaxation. Considering that spin-orbit interaction is a major factor determining the spin-lattice relaxation rate, the observed size-dependence of τ_b can be interpreted as the stronger spin-orbit interaction on the

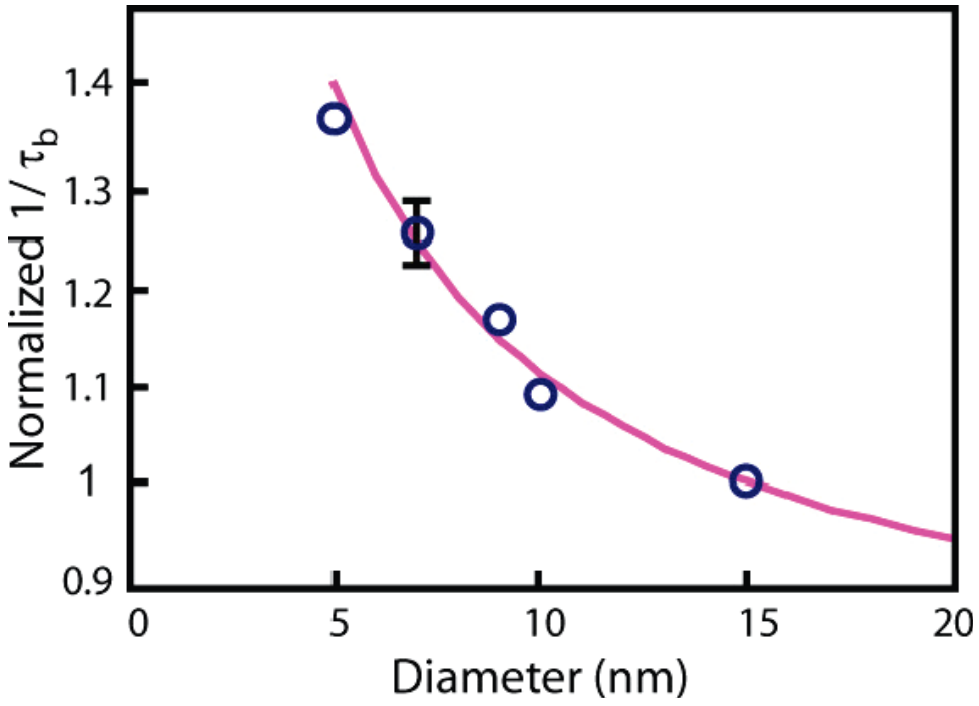

Figure 4.6 Relative values of $1/\tau_b$ (circle) and $|\langle V \rangle|^2$ (line) as a function of the diameter of nanocrystal. All the values are normalized to those of 15 nm sample. The error bar represents a typical margin of error.

surface. While the unequal vibrational baths of the surface and interior may contribute to the size dependence of τ_b, we believe it plays a less significant role in our study.

Stronger spin-orbit coupling at the surface can be justified as follows. In magnetic crystals, the effective spin-orbit energy (E_{so}), representing the strength of spin-orbit coupling, is on the order of $\xi^2/\Delta E$, where ξ is the atomic spin-orbit coupling parameter and ΔE is the ligand field splitting energy.[46] In Fe_3O_4 nanocrystals, Fe ions have a smaller number of oxygen ligand on the surface than in the interior. The lacking oxygen ligand is replaced with weakly bound carboxylic group of oleic acid used as the surfactant. Therefore, the ligand field acting on the surface spins is smaller than that of the interior spins. Consequently, E_{so} of the surface spins can be larger than that of the interior spins, resulting in a decreasing average E_{so} with increasing nanocrystal size.

A stronger spin-orbit interaction of the surface spin is also corroborated by the earlier study on surface coercivity of the magnetic nanocrystals by Vestal et al.[24] They observed that surface coercivity of $MnFe_2O_4$ nanocrystals increased as the ligand field of the coordinating molecules decreased. This indicates that the effective spin-orbit interaction of the surface spin increases with the weaker ligand field, consistent with our results. It would be desirable to correlate the size-dependence of $1/\tau_b$ to the experimentally determined variation of E_{so} to further support our conclusion more quantitatively. However, we did not pursue such an analysis in this study. In the bulk phase, information on the variation of E_{so} is indirectly obtained from magnetocrystalline anisotropy energy E_{mca}, which is more readily measurable. For this reason, earlier studies often correlated the spin relaxation rate with magnetic anisotropy.[19, 34] We did not make

a similar analysis in our study, since the size-dependent E_{mca} of the nanocrystals does not correctly reflect the size-dependent E_{so}, due to the heavily weighted contribution of the surface anisotropy to the experimentally measured total E_{mca}.[68]

4.4 Summary

In summary, we have investigated the relaxation rate of the spins in colloidal Fe_3O_4 nanocrystals following the optically induced demagnetization. From the analysis of spin relaxation times of nanocrystals of different size using a simple model, we estimated the efficiency of spin-lattice relaxation at the surface relative to the interior region. This result will also be a starting point for the investigations on the effect of surface modifications on the spin-lattice relaxation in nanocrystals.

CHAPTER V

EFFECT OF OXIDATION ON FARADAY ROTATION SIGNAL IN OXIDIZED Fe_3O_4 NANOCRYSTALS

5.1 Introduction

Magneto-optic effects, such as Faraday rotation (FR) and magneto-optic Kerr effect (MOKE), whose magnitudes are proportional to the magnetization for a given material, have been used as a useful tool to investigate the magnetic properties of the materials.[26, 41, 53] Both FR and MOKE measure the rotation of the linear polarization of the light transmitted through (FR) or reflected from (MOKE) the magnetic materials.[50] Due to the essentially optical nature of the technique, the measurements of magnetization via FR and MOKE could be made with a much higher spatial and time resolution than other magnetometric methods. For this reason, many studies on the static and dynamic magnetism of various ferromagnetic materials utilized MOKE or FR despite their limited capability to measure the absolute magnitude of magnetization.[19, 26, 69, 70] For instance, optically induced dynamic magnetism in ferromagnetic materials and carrier spin-dynamics in semiconductor quantum dots have been investigated employing time-resolved FR or MOKE.[15, 36, 71]

On the other hand, indirect measurement of the magnetization with FR and MOKE via coupled optical and magnetic degrees of freedom also can presents a challenge in some cases. Since the magneto-optic signal originates from the Zeeman effect on the electronic states by the magnetic field, MO signal can be modified by the

changes of both electronic and magnetic properties of the material.[50] For instance, partial oxidation of magnetic metals and metal oxides exposed to the ambient condition can modify the optical and magnetic properties the materials and FR signal can be affected by both in principle. Therefore, the interpretation of FR as a measure of magnetization can become more complicated when the change of magnetization is accompanied by the change of the optical transitions relevant to MO response.

For many metallic ferromagnets, such as Co and Ni, the decrease of magnetooptic signal upon oxidation to CoO and NiO is considered to reflect the decreasing magnetization of the material,[72, 73] since antiferromagnetic oxide component has little contribution to the magnetization and magnetooptic signal. On the other hand, spinel ferrites, such as Fe_3O_4, present a very different situation. For instance, oxidation of Fe_3O_4 to γ-F_2O_3 results in little change in magnetization, while Fe^{2+}-Fe^{3+} intervalence charge-transfer absorption, responsible for magneto-optic signal of Fe_3O_4, decreases with increasing oxidation. Therefore, the variation of magneto-optic signal in ferrites does not necessarily represent the variation of magnetization unless the degree of oxidation is well controlled. This is particularly an important issue in the nanocrystals, where the partial oxidation or reduction can occur readily than in bulk phase. In fact, earlier studies on γ-F_2O_3 thin films and nanocrystals reported widely scattered FR and MOKE data possibly due to the contamination by Fe_3O_4 during the sample preparation that has stronger magnetooptic response.[74-76]

In this chapter, systematic measurements of FR as a function of the degree of oxidation in iron oxide nanocrystals between Fe_3O_4 and γ-F_2O_3 phases were performed

to obtain a quantitative understanding of the effect of oxidation on the magnitude of FR signal. In order to obtain a detailed understanding of the correlation between FR and structure of partial oxidation, we compared FR of three different groups of partially oxidized iron oxide nanocrystals, i.e. γ-F_2O_3-Fe_3O_4 binary structure prepared by oxidizing Fe_3O_4, reducing γ-F_2O_3, and simple mixing Fe_3O_4 and γ-F_2O_3. All three nanocrystal samples exhibited a highly linear correlation between the amplitude of FR and the degree of oxidation and the correlation was independent of the interfacial structure between Fe_3O_4 and γ-F_2O_3.

5.2 Experimental section

The synthesis and characterization of nanocrystals were covered in Chapter II. In this study, spherical Fe_3O_4 nanocrystals with different sizes (5 ~ 15 nm in diameter) were used, and nanocrystals were suspended in hexanes for all the static Faraday rotation measurements. The reaction conditions of oxidation and reduction of iron oxide nanocrystals were described in Chapter II. The experimental setup for static Faraday rotation measurement was described in Chapter III.

5.3 Results and discussion

In order to investigate the effect of oxidation on FR signal, we prepared spherical iron oxide nanocrystals of varying degree of oxidation between Fe_3O_4 and γ-Fe_2O_3 phases in the diameter range of 5-15 nm. For a given diameter, the degree of oxidation in nanocrystal samples was varied in two different ways that result in two different

structures. One was prepared by oxidizing Fe_3O_4 nanocrystals resulting in nominally Fe_3O_4/γ-Fe_2O_3 core/shell structure (*Sample A*). The other was prepared by reducing γ-Fe_2O_3 nanocrystals resulting in nominally γ-Fe_2O_3/Fe_3O_4 core/shell structure (*Sample B).* While the core/shell structure cannot be visually resolved in TEM image of the iron oxide nanocrystals due to the very similar lattice structures of Fe_3O_4 and γ-Fe_2O_3, it can be inferred from the kinetics of oxidation and observations of shell formation in the oxidation of nanocrystals of other materials.[77]

The degree of oxidation in the nanocrystals was determined from the intensity of the broad absorption covering visible and near-IR region attributed to intervalence charge transfer (IVCT) transition between Fe^{2+} and Fe^{3+} ions.[25] The IVCT absorption present in Fe_3O_4 phase disappears as the oxidation converts Fe^{2+} into Fe^{3+}. The IVCT absorption was considered to be a good linear measure of the oxidation in γ-Fe_2O_3-Fe_3O_4 binary system and has been previously utilized to monitor the oxidation kinetics of Fe_3O_4 nanocrystals to γ-Fe_2O_3 nanocrystals.[25] The absorption spectra of both *Sample A* and *Sample B* were well represented as the linear combination of the spectra of γ-Fe_2O_3 and Fe_3O_4 nanocrystals. (See Chapter II) A common linear scale of IVCT absorption intensity was used to determine the degree of oxidation for both Sample A and Sample B of the same particle size. Zero intensity of IVCT absorption was taken to represent 100% γ-Fe_2O_3 phase. To obtain the reference absorption spectrum of 'pure' Fe_3O_4 phase, the spectrum was obtained under oxygen-free atmosphere using the freshly reduced Fe_3O_4 nanocrystals dispersed in N_2-bubbled solvent to avoid oxidation.

In addition to the two set of partially oxidized Fe_3O_4 nanocrystals with different core/shell structures, a composite mixture of γ-Fe_2O_3 and Fe_3O_4 nanocrystals (*Sample C*) was also prepared to examine the potential influence of the γ-Fe_2O_3/Fe_3O_4 interface on FR. *Sample C* corresponding to the degree of oxidation in partially oxidized nanocrystals was prepared simply by adjusting the ratio of γ-Fe_2O_3 and Fe_3O_4 nanocrystals that results in the same absorption spectrum of the partially oxidized samples.

Figure 5.1a shows FR of all three nanocrystal samples of the same diameter (7 nm) measured at 904 nm as a function of the degree of oxidation. All three samples exhibit very similar dependence of FR on the degree of oxidation, where the amplitude of FR is linearly correlated to the degree of oxidation. The value of FR at a given degree of oxidation is a simple linear combination of FR of the constituents weighted by their relative amount only. In our measurements, Fe_3O_4 nanocrystals exhibited an order of magnitude stronger magneto-optic response than γ-Fe_2O_3 nanocrystals. Since the saturation magnetization of γ-Fe_2O_3 and Fe_3O_4 nanocrystals are very similar, oxidation of Fe_3O_4 to γ-Fe_2O_3 phase does not affect the overall magnetization of the partially oxidized Fe_3O_4 nanocrystals. Therefore, the magnitude of FR of the nanocrystals of a given size represents primarily the degree of oxidation.

The fact that FR correlates linearly to the degree of oxidation and is insensitive to the structure of Fe_3O_4/γ-Fe_2O_3 interface indicates that magneto-optic response of Fe_3O_4/γ-Fe_2O_3 system is local in nature and the core/shell structure is relatively homogeneous magnetically. This is a distinctly different situation from the oxidation of

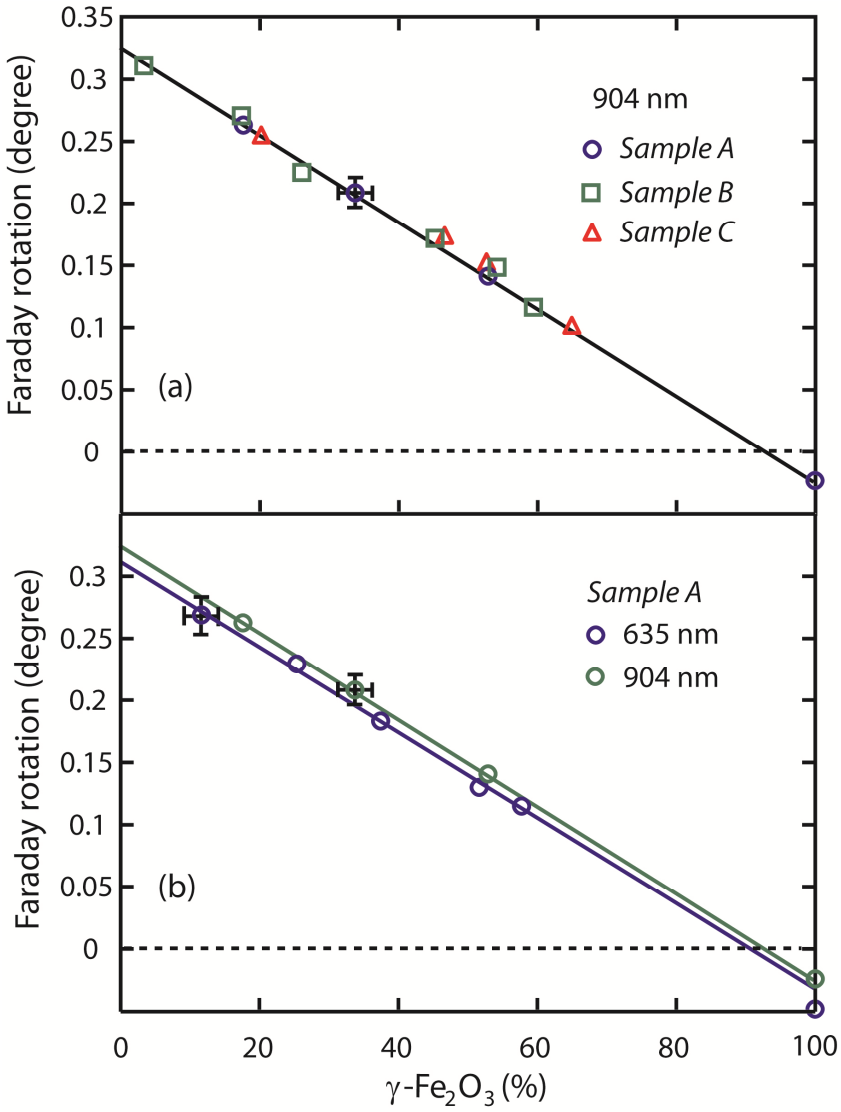

Figure 5.1 FR of 7 nm iron oxide nanocrystals as a function of degree of oxidation. (a) Comparison of FR of all three nanocrystal samples (*Sample A-C*). (b) Comparison of FR probed at two different wavelengths (635 and 904 nm).

many metallic nanocrystals, where the oxidized component is often antiferromagnetic resulting in magnetically heterogeneous interface. For instance, oxidation of Co nanocrystals results in Co/CoO core/shell structure with ferromagnetic core and antiferromagnetic shell,[72] where both the magnetization and magneto-optic signal arise mostly from the core. The Co/CoO core/shell structures with various degrees of oxidation were prepared by varying the ratio of N_2 bubbled and O_2 bubbled solvent the solvent, shown in Figure 5.2. The degree of oxidation can be regulated because the total amount of O_2 in the solvent is controlled. Figure 5.3 shows the FR signal and magnetization measured from SQUID together. In this case, FR signal of the partially oxidized Co nanocrystal should follow that of unoxidized core more closely, which varies as a function of volume following Langevin function.[72] In the case of iron oxide nanocrystals, similar ferrimagnetic order and volume magnetization of Fe_3O_4 and γ-Fe_2O_3 make the core/shell heterostructure less magnetically distinguishable. Therefore, the variation of FR with oxidation mainly reflects the local changes in optical properties independent of the detailed structure of Fe_3O_4/γ-Fe_2O_3 interface unless the particle size changes.

This observation was independent of the wavelength of the probe light as long as they belong to the same inter-valence charge-transfer transition as shown in Figure 5.1b. Essentially the same behavior was observed for 5 nm nanocrystals although the magnitude of FR was smaller than in 7 nm nanocrystals as predicted from Langevin function describing the magnetization of superparamagnetic nanocrystals, shown in Figure 5.4.

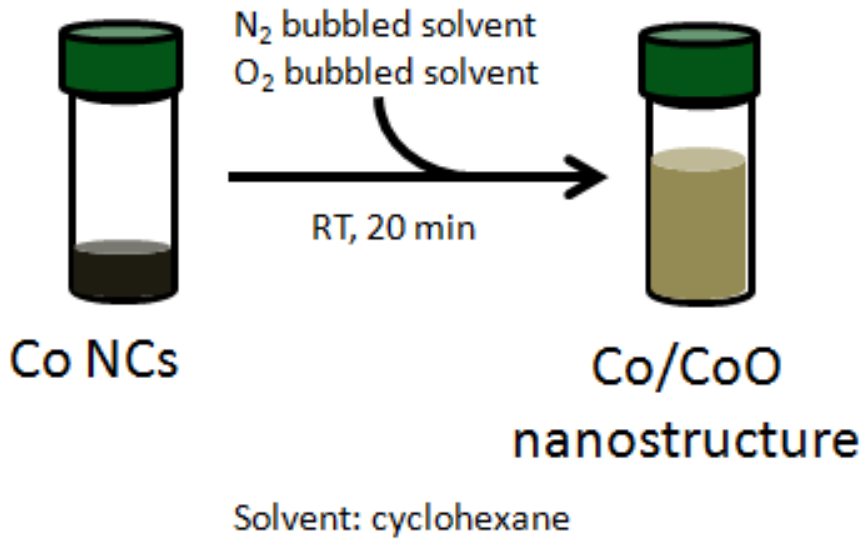

Figure 5.2 The scheme demonstrates the method to prepared Co/CoO with various degrees of oxidation.

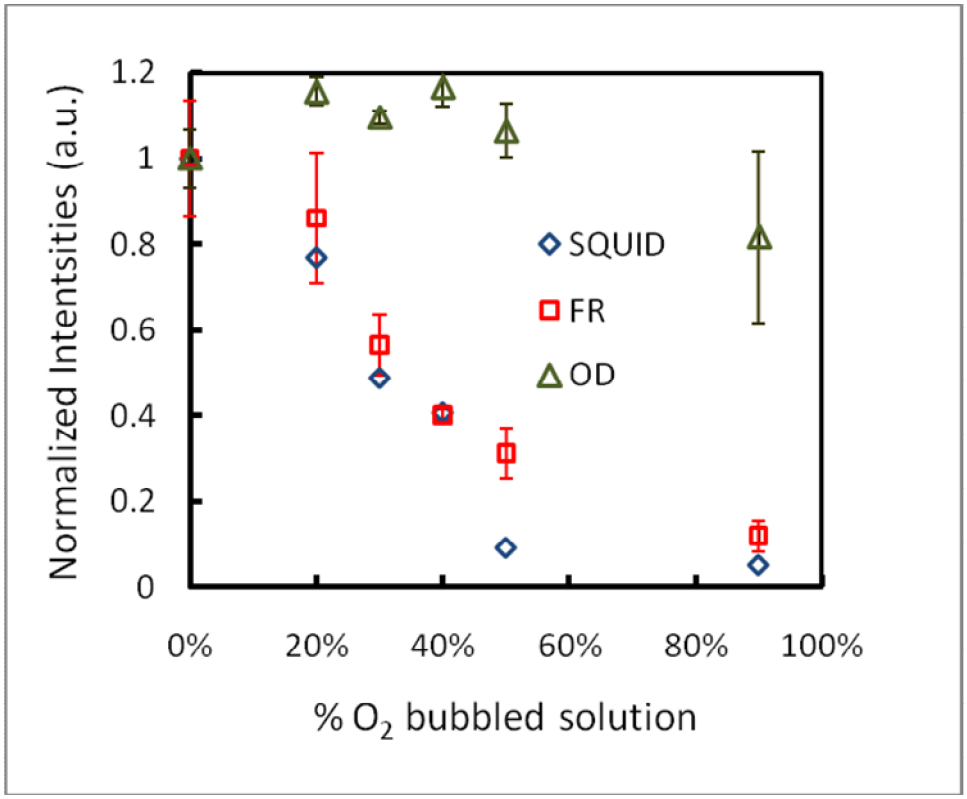

Figure 5.3 Normalized intensities of magnetization measured by SQUID, FR signal and the strength of optical transition at probing wavelength.

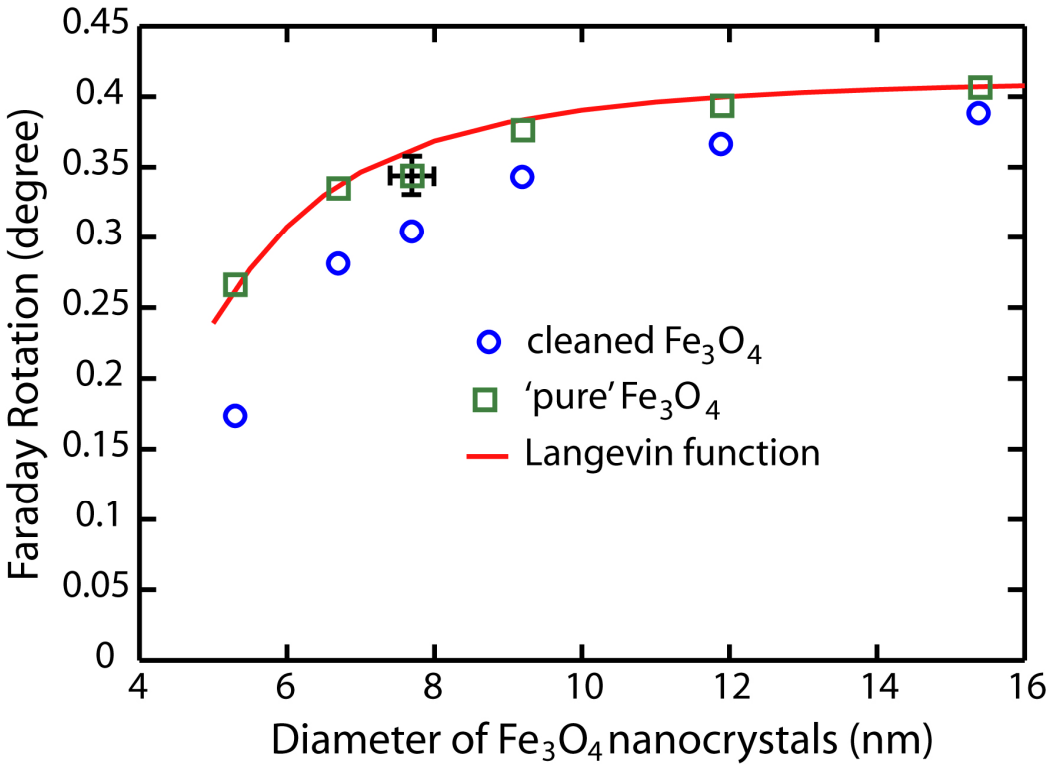

Figure 5.4 FR of cleaned (in the ambient condition) and 'pure' Fe_3O_4 nanocrystals. Langevin function was normalized to FR of 15 nm Fe_3O_4 nanocrystals.

Smaller nanocrystals show larger deviation on FR between cleaned and 'pure' Fe_3O_4 nanocrystals, suggesting surface oxidation has stronger effect on smaller nanocrystals. The result can be explained by smaller fraction of Fe_3O_4 in the smaller nanocrystal after oxidation during cleaning procedure. The thicknesses of oxidation layer are about 0.18±0.1 nm for all six size nanocrystals calculated from the decrease of absorption in the near-IR region. Even FR signal in 5 nm cleaned Fe_3O_4 deceased about 1/3 of FR signal in 'pure' Fe_3O_4, the FR signal is mainly contributed from Fe_3O_4, considering the intensity of FR in 'pure' Fe_3O_4 is one order larger than that in γ-Fe_2O_3.

The static FR and UV-Vis-NIR measurements in oxidized Fe_3O_4 provide some useful information for magnetization dynamics measurements, discussed in Chapter III and 4. The samples for previous magnetization dynamics were cleaned Fe_3O_4, nominally Fe_3O_4/γ-Fe_2O_3 core/shell nanocrystals. Thus, 780 nm optical pump pulses only excited Fe_3O_4 via IVCT of Fe^{2+} and Fe^{3+}, and the FR signals were mainly coming from Fe_3O_4, which dominates the FR signal in the range of 600-900 nm. Previously, the size dependent spin-lattice relaxation (SLR) rate in Fe_3O_4 nanocrystals was explained by the different SLR rate of surface and interior, originated from different ligand field. In the study, the different oxidation status on surface and interior of nanocrystals was not considered, and it can be an effective structural parameter for magnetization dynamics. In order to confirm the effect of surface oxidation on magnetization dynamics, the time-resolved Faraday rotation was performed to study cleaned and further oxidized Fe_3O_4 nanocrystals. Figure 5.5a shows the comparison of time-resolved FR data of both samples, and the signal amplitudes of both samples in the magnetization recoveries are

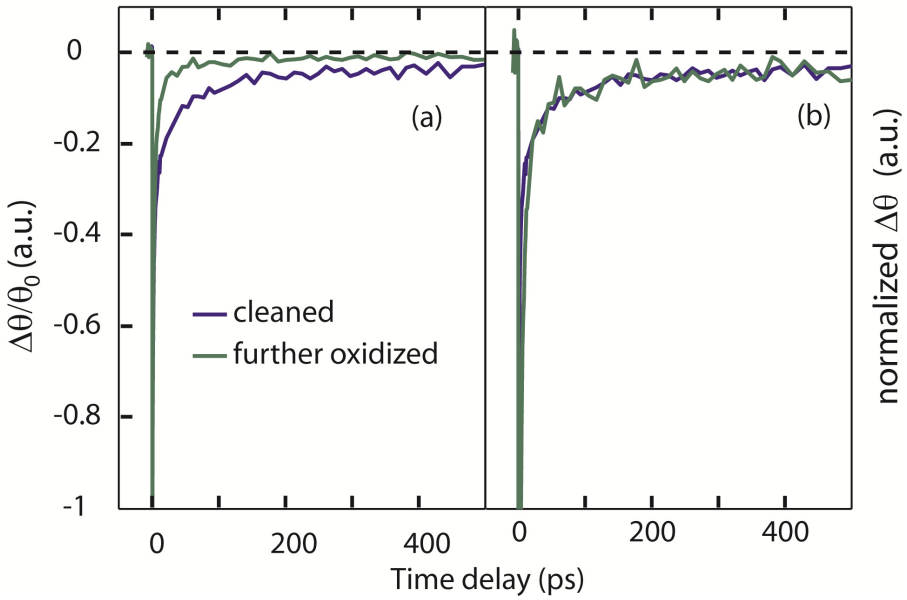

Figure 5.5 Time-resolved Faraday rotation data of cleaned and further oxidized Fe_3O_4 nanocrystals (5 nm). (a) Comparison of raw data. (b) Comparison of normalized data, in which the intensities at 200 ps.

very different, indicating surface oxidation is an effective structural parameter. However, the SLR rates of both samples are very similar based on almost perfect overlap of normalized data after 50 ps, shown in see Figure 5.5b.

5.4 Summary

The effect of oxidation on static Faraday rotation in iron oxide nanocrystals (between Fe_3O_4 and γ-Fe_2O_3) has been investigated by varying the degree of oxidation of nanocrystals. From the results, Faraday rotation (FR) signal of iron oxide nanocrystals is linearly correlated to the strength of optical transition between Fe^{2+} and Fe^{3+} in Fe_3O_4, not the change of magnetization. The Fe_3O_4 and γ-Fe_2O_3 binary system is a good system for this study because other physical properties of two species are very similar, such as saturation magnetizations and crystal structures. Fe_3O_4/γ-Fe_2O_3 binary structures prepared by different methods show the same effect of oxidation on FR signal. The result indicates the FR signal is affected by the distribution of Fe_3O_4 in the nanocrystal. The effect of oxidation on magnetization dynamics was also evaluated by time-resolved Faraday rotation measurement. The preliminary result indicates that the spin-lattice relaxation rates of iron oxide nanocrystals are not affected by the surface oxidation, but the surface oxidation still plays important role on magnetization dynamics. However, the effect of surface oxidation on magnetization dynamics cannot be resolved based the preliminary results.

CHAPTER VI

GENERAL CONCLUSIONS

6.1 Concluding remarks

This dissertation has described the studies of magnetization relaxation after optically induced demagnetization in superparamagnetic Fe_3O_4 nanocrystals by time-resolved Faraday rotation. The focus of this study is to understand the correlation between the size of nanocrystals and the rates of spin-lattice relaxation (SLR) in nanoscale magnetic materials. The results indicate that the size of Fe_3O_4 nanocrystals plays an important role on the spin-lattice relaxation process. Optically induced magnetization dynamics in magnetic materials were intensively studied because optical manipulation of magnetism was suggested as a possible route to achieve faster spin-based electronics or data storage devices. Our study may provide useful information for marking the spin-based electronics in nanometer scales in the future.

Fe_3O_4 nanocrystals were chosen as the model system to study the correlation between the size of nanocrystals and the SLR rates due to the well-established synthetic procedure. Fe_3O_4 nanocrystals in the size range of 5 nm to 15 nm with narrow size dispersion (~ 10 %) were prepared by thermal decomposition of $Fe(acac)_3$ with surfactants in high boiling point solvent. Larger Fe_3O_4 nanocrystals with narrow size dispersion can be prepared by performing seeded growth reactions. In seeded growth reaction, the same reaction condition was repeated with addition of small Fe_3O_4 nanocrystals as the seed. In addition, larger Fe_3O_4 nanocrystals can also be prepared by

increasing the reaction temperature, reducing the amount of solvent, or decreasing surfactant to Fe ratio. But the size dispersion of Fe_3O_4 nanocrystals became worse by using the latter methods. The phase conversion between two iron oxide phases (Fe_3O_4 and γ-Fe_2O_3) can be easily achieved by performing oxidation and reduction reactions. Partially oxidized Fe_3O_4 nanocrystals were simply prepared by heating sample to 90 ^oC in the air. Partially oxidized Fe_3O_4 nanocrystals should have a Fe_3O_4/γ-Fe_2O_3 core/shell nanostructure based on the oxidation kinetics data. The oxidation reaction follow Sidhu's diffusion model, meaning the oxidation rate was determined by the rate of outward diffusion of Fe^{2+} cations. γ-Fe_2O_3 nanocrystals can be prepared by oxidizing Fe_3O_4 ncnoarystals under O_2 at 150 ^oC, and size and crystal structure parameter do not change much after oxidation (< 1%). Partially oxidized Fe_3O_4 and γ-Fe_2O_3 nanocrystals can be reduced back to Fe_3O_4 phase with olelyamine under N_2 at the temperature higher than 200 ^oC. The reduction reaction can still occur without either olelyamine or N_2 atomsphere at the temperatrure higher than 200 ^oC.

Time-resolved Faraday rotation was the method to measure the magnetization dynamics after optically induced demagnetization in Fe_3O_4 nanocrystals in real time domain. Faraday rotation is an optical method to measure magnetic information, so the signal can be affected by both the strength of optical transition and the magnetization of materials. The signals of time-resolved Faraday rotation are symmetric under opposite magnetic fields, namely the magnitude of the FR signals are the same but in different directions at certain time delay. The results indicate the signal of time-resolved Faraday rotation in Fe_3O_4 nanocrystals is magnetic origin. In addition, the transient FR data and

transient absorption data were compared to further confirm the transient FR data is not reflecting the transient absorption data. Three heat reservoirs model was often used to explain the optically induced magnetization dynamics, although this model is a simple phenomenological model, meaning no microscopic mechanisms are included. The exchange processes of energy and angular momentum among three heat reservoirs are electron-spin, spin-lattice, and electron-lattice interactions. Some of the recent studies are eager to understand the electron-spin interaction after optical excitation, because the process is not well-understood compared to the other two processes. This process is important because optically induced change of magnetization was suggested as an optical trigger in spin-based electronics or data storage data in the future. The focus of our study is to understand spin-lattice relaxation after optical excitation in nanoscale magnetic materials.

The rates of spin relaxation following the optically induced demagnetization in colloidal Fe_3O_4 nanocrystals were investigated by time-resolved Faraday rotation. A simple model was utilized to analyze the spin relaxation times, and it was found that the size of Fe_3O_4 nanocrystals plays an important role on spin-lattice relaxation. Faster spin-lattice relaxation rate was obtained in smaller Fe_3O_4 nanocrystals due to higher efficiency of spin-lattice relaxation at the surface relative to the interior region. The efficiency of spin-lattice relaxation was correlated to the strength of spin-orbit interaction, which is affected by the atomic spin-orbit coupling parameter (ξ) and the ligand field splitting energy (ΔE). In Fe_3O_4 nanocrystals, the lattice is not continuous on the surface and Fe ions have a smaller number of oxygen ligand on the surface than in

the interior. Therefore, the ligand field acting on the surface spins is smaller than that of the interior spins. In that study of $Co_xFe_{3-x}O_4$ nanocrystals, the atomic spin-orbit coupling parameter (ξ) of nanocrystal was varied by changing the cobalt content in $Co_xFe_{3-x}O_4$ nanocrystals because the strength of spin-orbit coupling increases with cobalt content in $Co_xFe_{3-x}O_4$. The spin-lattice relaxation is faster in the nanocrystals with higher cobalt content for a given size of nanocrystal, which is consistent with the previous argument.

The effect of oxidation on static Faraday rotation in iron oxide nanocrystals was investigated by varying the degree of oxidation of the nanocrystals. Previously, the effect of oxidation on static Faraday rotation cannot be quantitatively understood because the exact degree of oxidation can be obtained easily in Fe_3O_4 thin films. The degree of oxidation can be easily estimated by using UV-Vis-NIR spectroscopy because superparamagnetic Fe_3O_4 nanocrystals can well-suspend in the solution.

The effect of oxidation on static Faraday rotation in iron oxide nanocrystals was investigated by systematically varying the degree of oxidation, which is determined by the intensity of optical transition in near-infrared region in the UV-Vis-NIR spectra. The results indicate the signal of Faraday rotation is linearly correlated to the strength of optical transition between Fe^{2+} and Fe^{3+} in Fe_3O_4, not the magnetization of materials. The same results are observed in samples with corresponding degree of oxidation prepared by three different methods: (i) oxidation of Fe_3O_4, (ii) reduction of γ-Fe_2O_3, and (iii) mixture of Fe_3O_4 and γ-Fe_2O_3. The results suggested the FR signal is not affected by the distribution of Fe_3O_4 in the nanocrystals. In addition, the signal of Faraday rotation

of ‘pure’ Fe_3O_4 nanocrystals depends on the size of nanocrystal and is proportional to the magnetization of materials. Therefore, the signal of Faraday rotation is affected by both the magnetization of materials and the strength of optical transition. Nanocrystals have high surface-to-volume ratio, and the surface is more readily oxidized than the interior. The surface oxidation of Fe_3O_4 nanocrystals seems not like a factor for spin-lattice relaxation by comparing the time-resolved Faraday rotation data of nanocrystals with different degree of oxidation.

6.2 Future directions

Nanocrystals have versatile structural parameters (see Figure 6.1), which allow us to study the correlation between the structural parameters and the magnetization relaxation after optically induced demagnetization. This studies in this dissertation show that the size of Fe_3O_4 nanocrytal plays an important role on spin-lattice relaxation, one of the magnetization relaxation pathways. In addition, the cobalt content in $Co_xFe_{3-x}O_4$ nanocrystals is also a factor for spin-lattice relaxation. The results suggested the magnetization relaxation may be strongly correlated to the structural parameters. It implies the magnetization relaxation may be controlled by varying the structural parameter. The exciton relaxation pathways in quantum dots can be regulated by the structural parameters in quantum dots. For example, core/shell nanostructure in quantum dots can block some non-radiative relaxation pathway, resulting in high efficiency of light emitting. Using the analogy of excition relaxation in quantum dots, other structural parameters in nanocrystals may also play important roles on magnetization relaxation.

Systematically studying the correlation between structural parameters and magnetization dynamics could be the future directions before making spin-based devices in nanometer scales.

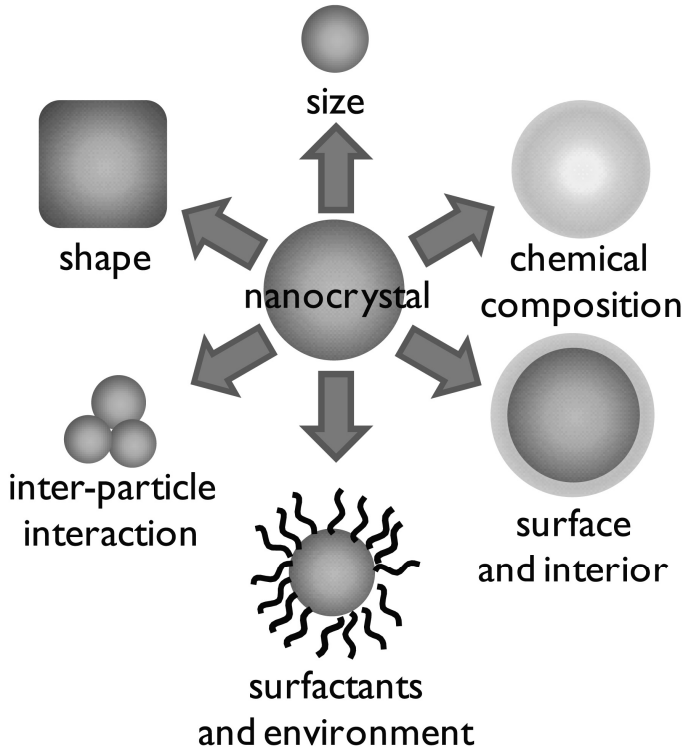

Figure 6.1 This schematic diagram shows that nanocrystals have versatile structural parameters. Some of these structural parameters may also affect magnetization dynamics.

REFERENCES

1. Chappert, C.; Fert, A.; Van Dau, F. N., *Nat. Mater.* **2007,** *6*, 813.
2. Wolf, S. A.; Awschalom, D. D.; Buhrman, R. A.; Daughton, J. M.; von Molnar, S.; Roukes, M. L.; Chtchelkanova, A. Y.; Treger, D. M., *Science* **2001,** *294*, 1488.
3. Prinz, G. A., *Science* **1998,** *282*, 1660.
4. Wang, J.; Sun, C.; Hashimoto, Y.; Kono, J.; Khodaparast, G. A.; Cywinski, L.; Sanders, G. D.; Stanton, C. J.; Munekata, H., *J. Phys.: Condens. Matter* **2006,** *18*, R501.
5. Kimel, A., V. ; Kirilyuk, A.; Hansteen, F.; Pisarev, R. V.; Rasing, T., *J. Phys.: Condens. Matter* **2007,** *19*, 043201.
6. Stöhr, J.; Siegmann, H. C., *Magnetism: From Fundamentals to Nanoscale Dynamics*. Springer: Berlin, 2006.
7. Hübner, W.; Bennemann, K. H., *Phys. Rev. B* **1996,** *53*, 3422.
8. Klimov, V. I.; McBranch, D. W., *Phys. Rev. Lett.* **1998,** *80*, 4028.
9. Burda, C.; Chen, X.; Narayanan, R.; El-Sayed, M. A., *Chem. Rev.* **2005,** *105*, 1025.
10. Cooney, R. R.; Sewall, S. L.; Dias, E. A.; Sagar, D. M.; Anderson, K. E. H.; Kambhampati, P., *Phys. Rev. B* **2007,** *75*, 245311.
11. El-Sayed, M. A., *Acc. Chem. Res.* **2004,** *37*, 326.
12. El-Sayed, M. A., *Acc. Chem. Res.* **2001,** *34*, 257.
13. Zijlstra, P.; Chon, J. W. M.; Gu, M., *Nature* **2009,** *459*, 410.

14. Krivorotov, I. N.; Emley, N. C.; Sankey, J. C.; Kiselev, S. I.; Ralph, D. C.; Buhrman, R. A., *Science* **2005,** *307*, 228.

15. Hsia, C.-H.; Chen, T.-Y.; Son, D. H., *J. Am. Chem. Soc.* **2009,** *131*, 9146.

16. Klimov, V. I., *The Journal of Physical Chemistry B* **2000,** *104*, 6112.

17. Müller, G. M.; Walowski, J.; Djordjevic, M.; Miao, G.-X.; Gupta, A.; Ramos, A. V.; Gehrke, K.; Moshnyaga, V.; Samwer, K.; Schmalhorst, J.; Thomas, A.; Hutten, A.; Reiss, G.; Moodera, J. S.; Münzenberg, M., *Nat. Mater.* **2009,** *8*, 56.

18. Park, J.; An, K.; Hwang, Y.; Park, J.-G.; Noh, H.-J.; Kim, J.-Y.; Park, J.-H.; Hwang, N.-M.; Hyeon, T., *Nat. Mater.* **2004,** *3*, 891.

19. Ogasawara, T.; Ohgushi, K.; Tomioka, Y.; Takahashi, K. S.; Okamoto, H.; Kawasaki, M.; Tokura, Y., *Phys. Rev. Lett.* **2005,** *94*, 087202.

20. Sun, S.; Zeng, H., *J. Am. Chem. Soc.* **2002,** *124*, 8204.

21. Sun, S.; Zeng, H.; Robinson, D. B.; Raoux, S.; Rice, P. M.; Wang, S. X.; Li, G., *J. Am. Chem. Soc.* **2003,** *126*, 273.

22. Xie, J.; Peng, S.; Brower, N.; Pourmand, N.; Wang, S. X.; Sun, S., *Pure Appl. Chem.* **2006,** *78*, 1003.

23. Hou, Y.; Xu, Z.; Sun, S., *Angewandte Chemie International Edition* **2007,** *46*, 6329.

24. Vestal, C. R.; Song, Q.; Zhang, Z. J., *J. Phys. Chem. B* **2004,** *108*, 18222.

25. Tang, J.; Myers, M.; Bosnick, K. A.; Brus, L. E., *J. Phys. Chem. B* **2003,** *107*, 7501.

26. Beaurepaire, E.; Merle, J. C.; Daunois, A.; Bigot, J. Y., *Phys. Rev. Lett.* **1996,** *76*, 4250.

27. Djordjevic, M.; Lüttich, M.; Moschkau, P.; Guderian, P.; Kampfrath, T.; Ulbrich, R. G.; Münzenberg, M.; Felsch, W.; Moodera, J. S., *Phys. Status Solidi C* **2006,** *3*, 1347.

28. Zhang, G. P.; Hübner, W., *Phys. Rev. Lett.* **2000,** *85*, 3025.

29. Bigot, J. Y.; Guidoni, L.; Beaurepaire, E.; Saeta, P. N., *Phys. Rev. Lett.* **2004,** *93*, 077401.

30. Lang, X. Y.; Zheng, W. T.; Jiang, Q., *Phys. Rev. B* **2006,** *73*, 224444.

31. Liu, C.; Zhang, Z. J., *Chem. Mater.* **2001,** *13*, 2092.

32. Fontijn, W. F. J.; Wolf, R. M.; Metselaar, R.; van der Zaag, P. J., *Thin Solid Films* **1997,** *292*, 270.

33. Song, Q.; Zhang, Z. J., *J. Phys. Chem. B* **2006,** *110*, 11205.

34. Cullity, B. D., *Introduction to Magnetic Materials*. Addison-Wesley Pub. Co.: Reading, Mass., 1972; p 190.

35. Klokkenburg, M.; Hilhorst, J.; Ern, B. H., *Vib. Spectrosc.* **2007,** *43*, 243.

36. Hsia, C.-H.; Chen, T.-Y.; Son, D. H., *Nano Lett.* **2008,** *8*, 571.

37. Buchanan, K. S.; Zhu, X.; Meldrum, A.; Freeman, M. R., *Nano Lett.* **2005,** *5*, 383.

38. Zhang, G.; Hübner, W.; Beaurepaire, E.; Bigot, J.-Y., *Top. Appl. Phys.* **2002,** *83*, 245.

39. Rhie, H. S.; Durr, H. A.; Eberhardt, W., *Phys. Rev. Lett.* **2003,** *90*, 247201.

40. Melnikov, A.; Radu, I.; Bovensiepen, U.; Krupin, O.; Starke, K.; Matthias, E.; Wolf, M., *Phys. Rev. Lett.* **2003,** *91*, 227403.

41. Ju, G.; Hohlfeld, J.; Bergman, B.; van de Veerdonk, R. J. M.; Mryasov, O. N.; Kim, J.-Y.; Wu, X.; Weller, D.; Koopmans, B., *Phys. Rev. Lett.* **2004,** *93*, 197403.

42. Wang, J.; Sun, C.; Kono, J.; Oiwa, A.; Munekata, H.; Cywinski; Sham, L. J., *Phys. Rev. Lett.* **2005,** *95*, 167401.

43. Stamm, C.; Kachel, T.; Pontius, N.; Mitzner, R.; Quast, T.; Holldack, K.; Khan, S.; Lupulescu, C.; Aziz, E. F.; Wietstruk, M.; Durr, H. A.; Eberhardt, W., *Nat. Mater.* **2007,** *6*, 740.

44. Koopmans, B.; Ruigrok, J. J. M.; Longa, F. D.; de Jonge, W. J. M., *Phys. Rev. Lett.* **2005,** *95*, 267207.

45. Kimel, A. V.; Kirilyuk, A.; Usachev, P. A.; Pisarev, R. V.; Balbashov, A. M.; Rasing, T., *Nature* **2005,** *435*, 655.

46. Hillebrands, B.; Ounadjela, K., *Spin Dynamics in Confined Magnetic Structures II*. Springer: Berlin, 2003; Vol. 87.

47. Andrade, L. H. F.; Laraoui, A.; Vomir, M.; Muller, D.; Stoquert, J. P.; Estournes, C.; Beaurepaire, E.; Bigot, J. Y., *Phys. Rev. Lett.* **2006,** *97*, 127401.

48. Klimov, V. I.; Mikhailovsky, A. A.; McBranch, D. W.; Leatherdale, C. A.; Bawendi, M. G., *Science* **2000,** *287*, 1011.

49. Scholes, G. D.; Kim, J.; Wong, C. Y.; Huxter, V. M.; Nair, P. S.; Fritz, K. P.; Kumar, S., *Nano Lett.* **2006,** *6*, 1765.

50. Zvezdin, A. K.; Kotov, V. A., *Modern Magnetooptics and Magnetooptical Materials*. Taylor & Francis: New York, 1997.

51. Lifshitz, E. M.; Landau, L. D.; Pitaevskii, L. P., *Electrodynamics of Continuous Media*. Pergamon Press: New York, 1984.

52. Baumberg, J. J.; Awschalom, D. D.; Samarth, N., *J. Appl. Phys.* **1994,** *75*, 6199.

53. Gupta, J. A.; Knobel, R.; Samarth, N.; Awschalom, D. D., *Science* **2001,** *292*, 2458.

54. Kise, T.; Ogasawara, T.; Ashida, M.; Tomioka, Y.; Tokura, Y.; Kuwata-Gonokami, M., *Phys. Rev. Lett.* **2000,** *85*, 1986.

55. Dormann, J. L.; Spinu, L.; Tronc, E.; Jolivet, J. P.; Lucari, F.; D'Orazio, F.; Fiorani, D., *J. Magn. Magn. Mater.* **1998,** *183*, L255.

56. Hansteen, F.; Kimel, A.; Kirilyuk, A.; Rasing, T., *Phys. Rev. Lett.* **2005,** *95*, 047402.

57. Chen, T.-Y.; Hsia, C.-H.; Son, H. S.; Son, D. H., *J. Am. Chem. Soc.* **2007,** *129*, 10829.

58. Scholl, A.; Baumgarten, L.; Jacquemin, R.; Eberhardt, W., *Phys. Rev. Lett.* **1997,** *79*, 5146.

59. Koopmans, B.; van Kampen, M.; Kohlhepp, J. T.; de Jonge, W. J. M., *Phys. Rev. Lett.* **2000,** *85*, 844.

60. Kubo, R., *Rep. Progr. Phys.* **1966,** *29*, 255.

61. Chen, T.-Y.; Hsia, C.-H.; Son, D. H., *J. Phys. Chem. C* **2008,** *112*, 10125.

62. Antao, S.; Jackson, I.; Li, B.; Kung, J.; Chen, J.; Hassan, I.; Liebermann, R.; Parise, J., *Phys. Chem. Miner.* **2007,** *34*, 345.

63. Batlle, X.; Labarta, A., *J. Phys. D: Appl. Phys.* **2002,** *35*, R15.

64. Goya, G. F.; Berquó, T. S.; Fonseca, F. C.; Morales, M. P., *J. Appl. Phys.* **2003,** *94*, 3520.

65. Bødker, F.; Mørup, S.; Linderoth, S., *Phys. Rev. Lett.* **1994,** *72*, 282.

66. Shrivastava, K. N., *Phys. Status Solidi B* **1983,** *117*, 437.

67. Sewall, S. L.; Cooney, R. R.; Anderson, K. E. H.; Dias, E. A.; Kambhampati, P., *Phys. Rev. B* **2006,** *74*, 235328.

68. Garanin, D. A.; Kachkachi, H., *Phys. Rev. Lett.* **2003,** *90*, 065504.

69. Peeters, W. L.; Martens, J. W. D., *J. Appl. Phys.* **1982,** *53*, 8178.

70. Fontijn, W. F. J.; van der Zaag, P. J.; Devillers, M. A. C.; Brabers, V. A. M.; Metselaar, R., *Phys. Rev. B* **1997,** *56*, 5432.

71. Gupta, J. A.; Awschalom, D. D.; Peng, X.; Alivisatos, A. P., *Phys. Rev. B* **1999,** *59*, R10421.

72. Tracy, J. B.; Weiss, D. N.; Dinega, D. P.; Bawendi, M. G., *Phys. Rev. B* **2005,** *72*, 064404.

73. Johnston-Peck, A. C.; Wang, J.; Tracy, J. B., *ACS Nano* **2009,** *3*, 1077.

74. Wang, H. Y.; Shen, J. X.; Qian, J. F., *J. Magn. Magn. Mater.* **1988,** *73*, 103.

75. Bentivegna, F.; Nyvlt, M.; Ferre, J.; Jamet, J. P.; Brun, A.; Visnovsky, S.; Urban, R., *J. Appl. Phys.* **1999,** *85*, 2270.

76. Tepper, T.; Ilievski, F.; Ross, C. A.; Zaman, T. R.; Ram, R. J.; Sung, S. Y.; Stadler, B. J. H., *J. Appl. Phys.* **2003,** *93*, 6948.

77. Sidhu, P. S.; Gilkes, R. J.; Posner, A. M., *Journal of Inorganic & Nuclear Chemistry* **1977,** *39*, 1953.

VITA

Name: Chih-Hao Hsia

Address: Department of Chemistry
Texas A&M University
PO Box 30012
College Station, TX 77843-3012
c/o Dong Hee Son

Email Address: kenthsia@gmail.com

Education:

2005-2010	Ph.D., Chemistry Texas A&M University, College Station, TX
2001-2003	M.S., Applied Chemistry National Chiao Tung University, Hsinchu, Taiwan
1997-2001	B.S., Applied Chemistry National Chiao Tung University, Hsinchu, Taiwan

Publications:

1. Tai-Yen Chen, Chih-Hao Hsia and Dong Hee Son; *J. Phys. Chem. C*, **2010**, *114*, 9713.
2. Chih-Hao Hsia, Tai-Yen Chen and Dong Hee Son; *J. Am. Chem. Soc.*, **2009**, *131*, 9146.
3. Stacey E. Wark, Chih-Hao Hsia and Dong Hee Son; *J. Am. Chem. Soc.*, **2008**, *130*, 9550.
4. Tai-Yen Chen, Chih-Hao Hsia and Dong Hee Son; *J. Phys. Chem. C*, **2008**, *112*, 10125.
5. Chih-Hao Hsia, Tai-Yen Chen, and Dong Hee Son; *Nano Lett.*, **2008**, *8*, 571.
6. Tai-Yen Chen, Chih-Hao Hsia, Hyung Su Son, and Dong Hee Son; *J. Am. Chem. Soc.*, **2007**, *129*, 10829.
7. Chih-Hao Hsia, Ming-Yu Yen, Hsin-Tien Chiu and Chi-Young Lee; *J. Chin. Chem. Soc.*, 2004, 51, 271.
8. Chih-Hao Hsia, Ming-Yu Yen, Chu-Chun Lin, Hsin-Tien Chiu, and Chi-Young Lee; *J. Am. Chem. Soc.*, **2003**, *125*, 9940.
9. Ming-Yu Yen, Chin-Wen Chiu, Chih-Hao Hsia, Fu-Rong Chen, Ji-Jung Kai, Chi-Young Lee and Hsin-Tien Chiu; *Adv. Mater.*, 2003, *15*, 235.